UNIVERSIDADE DE LISBOA
FACULDADE DE CIÊNCIAS

Collective dynamics of flexible active particles on substrates: from cells to tissues

“ Documento Definitivo”

Doutoramento em Física

Diogo E. P. Pinto

Tese orientada por:
Nuno Araújo e Margarida Telo da Gama

Documento especialmente elaborado para a obtenção do grau de doutor

2021

UNIVERSIDADE DE LISBOA
FACULDADE DE CIÊNCIAS

Collective dynamics of flexible active particles on substrates: from cells to tissues

Doutoramento em Física

Diogo E. P. Pinto

Tese orientada por:
Nuno Araújo e Margarida Telo da Gama

Júri:

Presidente:

- Doutor José Manuel Nunes Vicente Rebordão, Investigador Coordenador e Presidente do Departamento de Física da Faculdade de Ciências da Universidade de Lisboa

Vogais:

- Doutor Roberto Cerbino, Professor da Faculty of Physics da University of Vienna, Áustria
- Doutora Cristina Marchetti, Professor do Department of Physics da University of California Santa Barbara, Estados Unidos da América
- Doutor Pedro Manuel Alves Patrício da Silva, Professor Coordenador do Instituto Superior de Engenharia de Lisboa do Instituto Politécnico de Lisboa
- Doutor Nuno Miguel Azevedo Machado de Araújo, Professor Associado com Agregação da Faculdade de Ciências da Universidade de Lisboa, (Orientador)

Documento especialmente elaborado para a obtenção do grau de doutor

Doutoramento financiado pela FCT com a bolsa SFRH/BD/131158/2017

2021

Acknowledgements

I would like to start by acknowledging my supervisors, Nuno Araújo and Margarida Telo da Gama, for their continued support over the years. I had the privilege of meeting both while doing my bachelor degree and since then they have always been able to go beyond what is normal to properly help and guide my work. For that and much more I am extremely grateful.

During my PhD I had the opportunity of doing a five month internship at Syracuse University in the group of Lisa Manning. It was an excellent opportunity to understand more about the field and the model that would be the foundations of my thesis. I am very grateful for their help. I also want to acknowledge Gonca Erdemci-Tandogan who had a more direct contact with my work while at Syracuse and helped me have an easier transition into the topic. I would also like to acknowledge Daniel Sussman, not only for his help during this internship but also for his more recent contributions to the work presented in this thesis. Lastly, I would like to thank Arthur Hernandez for his support while at Syracuse and discussions not only while there but also after.

I would also like to thank all the members at CFTC, the ones still there and others who have already left. One of the benefits of staying in the same place for multiple years is that we get a front row seat at the groups evolution. When I started, the group was relatively small and I interacted with less than a handful of people on a daily basis. Since then, the group has grown substantially and sometimes there are not enough chairs in the lunch tables at the cafeteria for us all to sit. This also meant that at the start I was able to improve quickly since I got more attention, but now I am able to interact with more people and have more discussions that help solve my problems. I cherish this experience a lot.

Even if all that is discussed in this thesis is work related, none of it would be possible without the emotional support from my family over the years, especially Ana Sofia Inácio, my parents and my brother. They have supported me throughout all these years and without a doubt deserve more than a simple acknowledgment. Although sometimes I talk so little it seems I am paying a tax per word, I hope they still know how important they are.

In addition, I wish to acknowledge financial support from the Portuguese Foundation for Science and Technology (FCT) under Contracts no. PTDC/FIS-MAC/28146/2017 (LISBOA-01-0145-FEDER-028146), UIDB/00618/2020, UIDP/00618/2020 and SFRH/BD/131158/2017.

Abstract

We study the effects of disorder in epithelial confluent tissues through the Voronoi model for dense tissues. The modeling of epithelial tissues relies on three different mechanisms: cell-cell and cell-medium interactions, and propulsion or activity. First, we focus on the role of cell-cell interaction in this model by exploring, in the athermal limit, its anomalous jamming behavior. We introduce a new metric that allows us to find a hierarchical structure in its energy landscape similar to colloidal particle systems. We then introduce a cell-medium interaction by explicitly considering an interaction between the cells and their underlying substrate. We consider that the targeted geometry of the cells changes according to their spatial position and in turn affects the cells motility. We show that when the characteristic length scale of the disorder is smaller than the cell size, the cell motility increases when compared to its homogeneous counterpart. This result is in sharp contrast to what has been reported for tissues with heterogeneity in the mechanical properties of the individual cells, where the disorder favors rigidity. Due to the internal biological complexity of the cells, changes to the cell-substrate interaction should trigger a hierarchy of biochemical responses in the cell that lead to its adaptation to the new substrate region. As such, the process of cell adaptation to its underlying structure is not instantaneous but requires a finite time that in many cases competes with other relevant timescales for the dynamics such as, for example, the diffusion timescale. With this in mind, we then introduce a characteristic adaptation time of the cells to the cell-substrate interaction changes. We study how the competition between the adaptation of the cells and their mobility can compromise the fidelity of the substrate and by relating this with the previous disordered substrate propose a typical time scale for the adaptation of cells that is relevant for experiments. Lastly, we consider non-confluent tissues by allowing the cells to break from one another and create empty spaces. This change opens the door to the study of the surface properties of cell colonies and it is a first step towards the study of the transition from a single cell to confluent tissue. Implications of our findings in the field of Soft Condensed Matter Physics are discussed.

KEYWORDS:

Epithelial confluent tissues, Self-propelled Voronoi model, Glass transition, Cell-substrate interaction.

Resumo

Nesta tese estudámos as respostas físicas de tecidos confluentes epiteliais a perturbações do meio e como estas são influenciadas pela presença de heterogeneidades ao nível da interação célula-substrato. Sendo um sistema intrinsecamente fora do equilíbrio, as ferramentas existentes da física estatística de equilíbrio deixam de ser úteis e passa a ser necessário desenvolver novas ferramentas que possam auxiliar no estudo do problema. Dada a extrema complexidade dos sistemas biológicos, tanto do ponto de vista físico como químico, nós usamos uma abordagem *coarse grained*, onde apenas temos em conta algumas propriedades dos tecidos, para os podermos modelar computacionalmente e assim ter acesso às várias escalas relevantes do problema, desde a célula individual ao tecido de múltiplas células. Devido à simplicidade desta abordagem, podemos introduzir novas interações, como por exemplo, interações ao nível da célula-substrato que desencadeiam uma resposta do tecido, que tem relevância tanto do ponto de vista teórico, mas também prático no estudo de engenharia de tecidos e cancro.

A abordagem computacional começa com o desenvolvimento do modelo que consiga descrever, de uma maneira simplificada, mas fisicamente adequada, as propriedades do tecido. Para isso nós decidimos utilizar um método já desenvolvido na literatura, o modelo de Voronoi para tecidos confluentes. Este descreve o tecido confluente como um conjunto de células, sem espaços vazios. Cada célula é descrita por um ponto que marca a posição do seu centro geométrico e que é análogo ao núcleo da célula. A sua forma é obtida usando a tecelagem de Voronoi do espaço, o que leva a que cada ponto corresponda a uma região com forma poligonal. A interação célula-célula é introduzida por um funcional de energia, ou em termos mais comuns de física estatística o Hamiltoniano, que penaliza as células por terem uma forma muito diferente da sua área e perímetro preferenciais. Por fim, a atividade das células também é considerada, para descrever a habilidade de converter nutrientes do meio e transformar em energia que depois é usada para o movimento. Esta atividade da célula é modelada através de um simples movimento de propulsão com persistência, onde a célula tem memória da direção anterior. Assim, vai existir um fluxo constante de energia para o sistema que o afasta do equilíbrio. Apesar de ser um modelo maioritariamente geométrico que tenta simplificar todos os processos bioquímicos que se desencadeiam ao nível da célula, ele tem tido sucesso em reproduzir várias propriedades dos tecidos principalmente relacionados com as suas propriedades mecânicas.

Uma das propriedades dos tecidos que é capturada pelo modelo descrito, é a sua habilidade de transitar de um estado mais rígido, onde o tecido tem uma resposta forte a perturbações comparável a um sólido, para um estado semelhante ao de um fluido, onde o tecido consegue fluir facilmente como resposta à perturbação. Do ponto de vista físico, algo ainda mais relevante, é que esta transição pode ser descrita através de argumentos puramente geométricos. Quando o rácio entre o perímetro e a área é menor que 3.81, as células não vão ter espaço suficiente para satisfazer a sua geometria preferencial (dada pelo Hamiltoniano) e por isso cada uma vai estar enjaulada pelos seus vizinhos

que tentam aumentar o seu tamanho. Por outro lado, se este rácio for maior que um dado valor limite, isto já não se verifica e as células vão poder mover-se livremente pelo tecido, fazendo com que ele, como um todo, se comporte como um fluido. Este comportamento é muito semelhante a outro tipo de sistemas, chamados vidros ou materiais amorfos, usualmente constituídos por partículas granulares ou coloidais.

Um dos principais impactos desta descoberta, é contribuir para a mudança no paradigma de problemas biológicos. Assim, um problema que poderia apenas ser considerado como algo relevante do ponto de vista biológico passa a ser também relevante do ponto de vista físico. Apesar desta descoberta, muitas perguntas ficaram por responder e muitas outras foram abertas. Tal como foi mencionado previamente, fazer a ponte entre sistemas amorfos inorgânicos e estes sistemas biológicos pode ser uma porta para compreender muito mais sobre tecidos epiteliais e o seu comportamento tanto *in vivo* como *in vitro*. Algo que não foi explorado em estudos anteriores é a interação entre as células constituintes do tecido e o seu suporte físico. Tanto em laboratório como no revestimento de órgãos, tecidos epiteliais são sempre suportados por uma superfície física, seja outras células, a matriz extracelular ou um substrato sintético criado em laboratório. As interações entre as células e o seu meio envolvente são por isso um ingrediente relevante nas propriedades do tecido como um todo. Nesta tese, exploramos algumas destas questões no contexto da transição de rigidez dos tecidos.

No primeiro capítulo é feita uma introdução ao tópico onde para lá da motivação também é discutida a questão da universalidade na biologia. No segundo capítulo discutimos as principais interações no contexto de tecidos epiteliais. Também fazemos uma introdução mais detalhada ao modelo de Voronoi com atividade e o que já foi feito e quais as perguntas ainda por responder.

Os capítulos seguintes são relativos aos resultados desenvolvidos durante o período de doutoramento. No capítulo três introduzimos o modelo de Voronoi sem atividade para estudar a transição de rigidez puramente de um ponto de vista geométrico. Aqui usamos técnicas desenvolvidas para sistemas amorfos inorgânicos para explorar ao detalhe esta transição. Para isso medimos as propriedades hierárquicas do espaço de energias. Nós propomos uma nova métrica que nos possibilita a medição destas propriedades e assim identificamos uma região do espaço de parâmetros onde o tecido apresenta duas fases rígidas com um espaço de energias distinto. Sendo assim, o tecido não apresenta apenas a transição entre a fase rígida e a fase fluida, mas existe também uma transição entre fases rígidas. Por fim, propomos potenciais consequências para o estudo de tecidos e sugerimos uma possivel ponte entre os sistemas biológicos e os materiais amorfos inorgânicos.

No capítulo quatro introduzimos a atividade das células no tecido e também adicionamos uma interação entre a célula e o substrato. Esta interação é introduzida no modelo de uma maneira simplificada onde alteramos um dos parâmetros do Hamiltoniano que controla a forma das células. Como estamos interessados em estudar substratos heterogéneos, esta interação vai depender da posição espacial da célula. Aqui, estudamos como uma distribuição aleatória afeta a transição de rigidez do tecido. Do ponto de vista físico este problema assemelha-se ao estudo de sistemas com desordem. Assim traçamos uma comparação entre dois tipos de desordem, a primeira ao nível do substrato e a segunda ao nível da célula, e observamos que enquanto a segunda apenas torna o tecido mais rígido, a primeira pode torná-lo mais fluido dependendo da preparação do substrato.

No capítulo cinco introduzimos uma escala de tempo de adaptação da célula ao substrato, de modo a que quando esta se move de uma região do substrato para outra com propriedades diferentes, a célula não se adapte instantaneamente, mas demore um tempo característico. Este tempo está relacionado com o motor bioquímico da célula que desencadeia várias reações que alteram a forma da célula dependendo da região do substrato em que se encontra. Aqui observamos que existe uma

competição entre a escala de tempo de adaptação das células e a escala de tempo característica para a sua mobilidade que pode comprometer a fidelidade do padrão. Também introduzimos um modelo contínuo que está em concordância com os resultados numéricos. Usando este estudo e o do capítulo anterior conseguimos estabelecer limites ao tempo característico de adaptação das células que pode ser relevante para sistemas experimentais.

Por fim, no capítulo seis introduzimos espaços vazios ao tecido de modo a poder modelar um sistema não confluente. É feita uma análise numérica do modelo onde exploramos o comportamento de colónias de células e como as propriedades da sua interface evoluem à medida que a colónia cresce ou quando as células ficam mais ativas. Deste modo tentamos criar uma ponte entre o sistema das células individuais e o do tecido confluente, que ainda ilude a comunidade científica.

PALAVRAS-CHAVE:

Tecidos epiteliais confluentes, Modelo de Voronoi com propulsão, Transição vítrea, Interação célula-substrato

Contents

List of Figures

Acronyms

ECM	Extracellular Matrix
SPV	Self-Propelled Voronoi
AVM	Active Vertex model
BVM	Brownian Vertex model

Chapter 1

Introduction

Is there universality in biology? As physicists interested in studying biological systems, we believe that the answer is yes. Otherwise, we would be left with no way to substantially contribute to the field, as physics aims at finding universal laws [9–11]. On the bright side, the general consensus seems to be shifting towards this answer as well. Recent studies have made breakthrough findings on the universality of biological systems, from the scaling laws of phylogenetic trees [12–15], to the flocking of animals [16–21], to the mechanical properties of confluent tissues [1, 2, 22–28], to the complex motion of individual cells [29–35] and even to the understanding of the behavior of cell organelles [36–40]. So far, Soft Matter physics has been able to capture multiple universal properties of biological systems at wildly different length and time scales, pushing the boundaries of physics even further as a multidisciplinary field. More conservative people will reply that Soft Matter is about systems at the microscale where the interaction strength is comparable with the thermal energy. What we have succeeded in doing is to extend the same ideas and methods to systems at different scales.

The study of epithelial tissues is a relevant example, in the context of this thesis, of the current shift. Undoubtedly a biological system that has attracted physicists for several years [41–44], but only with the recent advances in computer imaging and tracking one has been able to truly grasp some of the universal behavior of these systems [1, 24, 28, 45, 46]. Even with these technological advances many conceptual difficulties remain. The fact that cells are living systems with a biochemically complex *internal motor* which transforms nutrients into energy that is then used for its own motion, drives the system far from equilibrium [1, 29, 32, 34]. Importantly, the driving is local, it occurs at the level of single cells. Thus, conventional thermodynamic tools developed for equilibrium systems are no longer useful and require a conceptual change to be applied to these new systems. This property also allows cells to move autonomously without the need for externally applied forces.

Cells also feel their surroundings. Thus, changes in their environment can trigger a hierarchy of biochemical processes that change the properties of individual cells. This can be seen in multiple situations, but the most straightforward is when a cell is on a heterogeneous substrate. For example, it is well established that cells tend to move towards stiffer regions of the substrate where they can more easily anchor [47–54]. In this context, there is another relevant topic to mention. Epithelial tissues are usually studied from a confluent point of view, meaning that the tissue is made of a vast number of cells with no empty space [55]. It is therefore a many body problem with a truly many body (non reciprocal) interaction. This is in contrast with typical soft matter systems like colloidal particles where interaction are usually considered as symmetric pair-wise [56–60]. This raises several challenges to the generalization of ideas and methods developed in the context of passive systems to living ones [61–65]. Understanding the role of cell-cell and cell-environment interaction is of major importance for morphogenesis, collective cell motion, and wound healing [65–73].

Understanding the cell collective behavior in biological tissues has become one of the major interdisciplinary challenges of recent years [53, 64, 65, 74–76]. Through both theoretical and experimental efforts, key properties of these tissues have been discovered. One example is that they may be either rigid or flexible depending on the properties of individual cells and external conditions [28, 63, 76–78]. This behavior is not exclusive to biological tissues. Particulate systems, such as colloidal suspensions or granular media exhibit similar dynamical slowing down when density is increased or temperature decreased, which leads to disordered amorphous materials kinetically arrested in jammed or glassy states [79–81]. In living tissues, although the nature and properties of the rigid states are still under debate [28, 63, 76, 77], it is undoubtedly a collective phenomenon. This is in contrast with the mesenchymal to epithelial transition usually discussed in the context of epithelial tissues. During development, cells undergo a mesenchymal to epithelial transition and the tissue goes from a state with more irregularly shaped cells (mesenchymal) to another where cells adopt more regular shapes (epithelial). The consequence of this transition is that the tissue also goes from a fluid to a rigid state. But more importantly, this is a transition at the level of the chemistry of the individual cell. Only when a significant portion of the cells have undergone this change, can the tissue actually flow. On the other hand, the rigidity transition, described previously, is a purely collective behavior [82]. It does not happen due to a biochemical change in the individual cell but due to a collective interacting aggregate of cells [1, 2, 22, 25, 45, 46, 61, 61, 76, 83–86]. This suggests that there is something universal about epithelial confluent tissues where physicists can play a relevant role.

From a theoretical point of view, developing a model to tackle these issues is not a simple task. Due to their extreme complexity, it is intractable to actually describe all the biochemical processes happening inside the individual cell when trying to describe phenomena at the tissue level. Thus, one needs coarse-grained models in order to develop a good insight of these systems [23, 87]. An instinctive first approach is to use models already developed for inorganic particles, like colloidal systems, where interactions are pairwise and the individual constituents are modeled as isotropic spherical particles [16, 20, 21]. On the one hand, the particle description has been able to properly capture collective migration of tissue cells in a simplistic way [20, 21, 88–91]. On the other, particle models miss details related to cell shape and its coupling to polarity, which are relevant for some aspects of epithelial dynamics [63, 76, 77, 82, 92–98]. As such, other models have been adapted to provide a proper insight into the problem. A family of models taken from the physics of foams that has been quite successful at capturing the mechanical properties of epithelial confluent tissues are the active network models [76, 82, 92, 94]. The Vertex and Voronoi models, in 2D or 3D, constitute this family of models which are represented as multiple vertices connected by straight lines (edges), forming a system spanning network. The major difference between the two lies in the degrees of freedom. The Vertex model uses the vertices of the network as degrees of freedom, while the Voronoi model uses the vertices in the dual of this network [42, 44]. The Vertex model is more tractable since there is more control over the individual cell shape. The Voronoi model has one third of the degrees of freedom allowing more robust simulations. Although both models seem quite similar, not only from an aesthetic point of view but also from a physical one [2, 22, 62, 84], there are major differences between the two which can severely impact our view of epithelial confluent tissue [99].

In these models, the cell-cell interaction is usually described by an energy functional that dictates the interaction between cells and is analogous to the Hamiltonian in standard equilibrium physical systems [2, 83]. This energy functional penalizes the cells for deviating from a preferential area and perimeter (or surface area and volume in 3D). In the Vertex model the geometry of the cell is given by the edges connecting the different vertices which enclose empty spaces of the simulation box into regularly shaped polygons [45,46]. In the Voronoi model, the geometry of the cell is calculated using the Voronoi tesselation of the degrees of freedom [100]. In both, since the area and perimeter of a given cell depend on its neighbors, the interactions will thus be many body. In chapter two of this thesis we will discuss in more detail the different models used to describe biological systems and how they compare to one another. In these models a dynamical slowing down is observed when the ratio between the preferential perimeter and the area of the cell decreases [2,22,83]. Cells are caged by their neighbors and are unable to break free. This rigidity transition, as described above, has been one of the staple predictions of this model with applications ranging from disease diagnosis [76] to organ development [94]. For cells to move they need to exchange neighbors, commonly referred to as $T1$ transitions. In the rigid regime, the characteristic energy barrier for these $T1$ transitions is too high and cells are unable to move. This happens since when the ratio between the preferred perimeter of the cells and the square root of their area is smaller than a given threshold, the cells tend to expand until they become geometrically constrained by their neighbors. As this ratio increases, the cells are able to deform and the energy barriers associated with $T1$ transitions decrease, allowing the tissue to flow. As in particulate systems [101–107], this glassy behavior appears due to the high degree of roughness of the energy landscape, as one approaches the rigid regime, populated with several local minima that trap the system in a specific configuration which can be far from the global minimum [108]. Aside from these similarities, the Vertex and Voronoi models actually have quite anomalous glassy dynamics, with sub-Arrhenius scaling of the relaxation time with temperature and the appearance of collective low frequency modes [84]. This raises the question, are these two models different from a physical point of view?

This topic is explored in the third chapter of the thesis, where we study the Voronoi model in the athermal limit, without activity or thermal fluctuations. As mentioned above, the number of degrees of freedom of each model is quite different. In both models there are two constraints per cell, one coming from the area and another from the perimeter terms in the energy functional. This energy functional can be thought of as a spring which tries to push cells towards a preferred perimeter and area, which when under tension acts as a constraint. Since the Vertex model has three times more degrees of freedom than cells, the system is underconstrained [105, 109]. Recent work has shown that these underconstrained models undergo a rigidity transition at a critical point [61,62]. This can be thought of as a minimal edge length problem, thinking of the edges between vertices as springs. When the springs are under tension the vertices are constrained and unable to move. These tensions act as additional constraints to the cells making it rigid and overconstrained. After a given threshold, this tension disappears and they are able to move freely. More recent work has suggested a mechanism of energetic rigidity since this tension is directly related to the energy of the cells [110]. In the Voronoi model, the number of degrees of freedom is equal to the number of constraints, thus it is marginal [105, 109]. Due to this, it is unlikely that the model becomes fluid and recent results have hypothesized that it might be rigid throughout the parameter space in the athermal regime since there are always tensions, or more commonly residual stresses, constraining the cells movement [99]. In chapter three we discuss these results and use methods developed in the particulate glassy systems [111] to show that although there is no sign of a rigidity transition, the energy landscape of the tissue undergoes a transition between rigid states which alter significantly its properties. This new rigid state is no longer typical, in the sense that the energy landscape is no longer populated with multiple distinct well-defined minima, but is partially flat. We draw similarities between this transition and the Gardner transition observed in particulate systems in infinite dimensions [102, 112] and probed in finite ones [103, 111, 113].

As mentioned previously, there are three main ingredients in the study of epithelial confluent tissues, cell-cell and cell-environment interactions, and activity. In chapter three we focus on the cell-cell interaction and neglect activity. In chapters four and five we consider cell activity and consider explicitly the interaction between the cell and its supporting physical structure. An extensive body of research shows that the cell morphology and dynamics are sensitive to the physical and chemical properties of their underlying structure, be it the extracellular matrix or a culture substrate [47–54, 64]. For example, it has been shown that substrate stiffness can significantly affect the geometry of cultured cells, including their spreading area [54, 114], volume [115], and shape elongation [116]. Furthermore, the epithelial layer of cells is supported by a complex polymeric structure, the extracellular matrix (ECM), which plays a pivotal role in the tissues collective behavior [47, 117–120]. Although the ECM is often quantified by bulk metrics, it has a high degree of heterogeneity, which in turn influences the tissue itself. In chapter four we explore how a heterogeneous substrate, consisting of a rough landscape that changes the preferred geometry of the cells depending on their position, influences the mechanical properties of an epithelial confluent tissue. Previous work has already established that cell shapes change as a function of substrate properties [114] and cell shape in turn governs the rate of cell diffusion in monolayers [76]. Heterogeneity at the cell level is known to substantially change the tissue dynamics [121, 122], with implications in cancer research where some cancer cells are found to be softer than normal cells [123–125]. Studies using the Vertex model observed that a tissue always becomes more rigid in the presence of heterogeneity [8]. We show that it is possible to change the motility of the cells using a heterogeneous substrate by controlling its dispersion. By tuning the characteristic length scale of the disorder to be smaller than the typical cell size, it is possible to make the tissue more fluid.

In chapter five we shed light on the motility of the cells. There is a sustained interest in the possibility of generating spatial patterns of cells with different properties, which is critical for morphogenesis, collective cell motion, and wound healing [65–73]. A possible approach is to culture a single cell type on a patterned substrate, and allow the patterned substrate to change the properties of cells to generate a pattern [67, 68, 70, 71]. Patterned substrates have been used to a large extent in the context of inorganic materials [126–129]. However, their use for biological systems raises several additional difficulties. Besides the need for biocompatible materials, the transduction of external stimuli into biological signals that control the cell morphology and mechanics is not instantaneous. It requires a hierarchy of biochemical processes, which sets a characteristic adaptation time that can extend over hours [130], for example, cells in rigid substrates reorganize their cytoskeleton through stresses applied to the actin network to conform to the substrates properties [131]. The problem is that, within the adaptation time scale, cells might move around and explore other regions of the substrate. Thus, the fidelity of patterns in the regulation of cell tissues should depend on how the adaptation time compares with the other relevant time scales. This is precisely what we study here.

The three chapters described previously cover the three facets of confluent epithelial tissues, cell-cell and cell-environment interaction, and activity. In chapter six we focus on the bridge between the single cell system and the fully grown confluent tissue [23–25,29,35,39,52,67,132–136]. For this, we change the Voronoi model to allow for gaps between the cells, similar to Ref. [137]. Thus, for weaker cell-cell adhesion, the cells will be able to break apart and take a more circular isotropic shape, while for stronger adhesion they will still be able to adhere to each other and form a cell colony. Recent studies have suggested that while the surface tension of cell colonies is quite heterogeneous and anisotropic, simple homogeneous continuum models are able to capture its behavior [132]. Using the non-confluent Voronoi model we are able to simulate small cell colonies. We investigate how the surface tension of the cell colonies change as it grows and try to understand how the different properties of the cells, cell-cell interaction and activity, affect this scaling.

1.1 List of publications from the thesis

1. Diogo E. P. Pinto, Gonca Erdemci-Tandogan, M. Lisa Manning and Nuno A. M. Araújo, *The Cell Adaptation Time Sets a Minimum Length Scale for Patterned Substrates*, Byophys. J. **119**, 2299 (2020).

   I performed the simulation studies and developed the continuum reaction-diffusion model. I was also involved in the writing of the paper. The results from this paper are presented in chapter 5

2. Diogo E. P. Pinto, Daniel M. Sussman, Margarida M. Telo da Gama and Nuno A. M. Araújo, *Hierarchical structure of the energy landscape in the Voronoi model of dense tissue*, submitted.

   I performed the numerical studies and implemented the GPU optimizations necessary for the simulations. I was also involved in the writing of the paper. The results from this paper are presented in chapter 3

3. Diogo E. P. Pinto, Margarida M. Telo da Gama and Nuno A. M. Araújo, *Substrate disorder promotes cell motility in confluent tissues*, submitted.

   I performed the simulation studies. I was also involved in the writing of the paper. The results from this paper are presented in chapter 4

Chapter 2

The model

The last decade saw groundbreaking technical [138] and conceptual [32, 37] advances in the study and characterization of biological systems. On the technical side, time-lapse imaging and fluorescence microscopy have become standard tools in life-science laboratories, technologies such as particle imaging velocimetry enabled a detailed mapping of velocity fields and strain tensors in the tissue [139], and new technologies such as traction microscopy have enabled the direct mapping of the forces that cells exert on their surroundings as they migrate [24]. All mechanical variables relevant to the problem of collective cell migration have thus become available in time and space. This technological revolution has coincided with the development of the theory of active matter [30, 32], which provides an ideal framework to rationalize the collective movement of cells. These accomplishments centered condensed matter physics in the study of collective cell behavior and shifted the conceptual reductionist framework to a picture of emerging collective phenomena characteristic of soft matter systems [25].

Despite these advancements, a general theory of active matter is still out of reach, especially concerning biological systems. The vast variability characteristic of cells or bacteria is still one of the major challenges [1, 29]. Physics is concerned with the universality of these phenomena, if they depend too much on the details, e.g. cell species or organelles, then general theories will not be possible and only system dependent conclusions can be taken. From a theoretical point of view, it is then ideal to develop coarse-grained models that properly capture the correct physics of the problem. As such, over the last decades, multiple models have been proposed that try capturing the different phenomena of biological systems, from single particle to continuum based theories [23, 35, 87]. In this chapter we explore the main ingredients of these models to study collective behavior in cells and tissues. Then, we focus on active network models, more specifically the Self-Propelled Voronoi model and introduce the relevant properties that will be useful for the following chapters. We also make a detailed description of the numerical implementation and some of our contributions to the optimization of the code used for the simulations.

2.1 Numerical modeling of living tissues

Even though cells and tissues are complex systems, efforts have been made into isolating the relevant interactions that play a role in their collective behavior [24, 27, 29, 63, 136]. These can be divided into three main interactions (Fig. 2.1), cell-environment, cell-cell and activity or orientation [23]. Most of the progress done on these systems has been performed *in vitro*, since *in vivo* measurements of traction forces and velocity fields are still quite challenging. As such, cells are

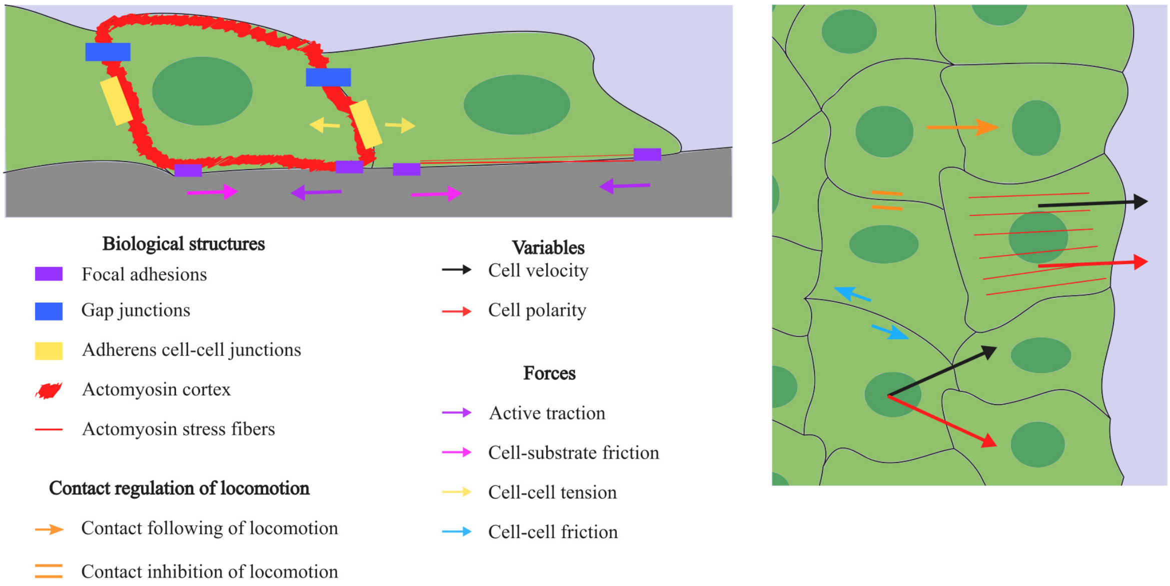

Figure 2.1: Schematic representation of a monolayers top (right figure) and side (top left figure) views, based on Fig. 2 of Ref. [1]. We have color coded symbols that represent the different interactions and relevant biological structures in cells. When modeling an epithelial tissue these different components should be taken into account as appropriate for the behavior it is meant to describe.

usually cultured in a substrate where they adhere and develop into a fully confluent monolayer. In these configurations, the cell-environment interaction is usually attributed to a substrate, be it the ECM or the physical culture substrate [47, 117–120]. This interaction is commonly divided into two contributions: the active traction forces and the friction forces.

The active traction forces stem from the cell's actomyosin cytoskeleton, where the action of myosin molecular motors on actin filaments generates contractile forces which are then transmitted to the substrate through focal adhesions [136]. For this, the cell must first break its symmetry and polarize. This front to rear polarization is usually accomplished through the formation of actin-based protrusions which generate an inward-pointing active traction resulting in a force that propels the cell forward in the direction of its polarity. Thus, in models, the force that drives cell migration is usually assumed proportional to a cell polarity vector, with a coefficient that depends on both cell–substrate adhesion and the active force–generating processes in the cytoskeleton [35]. The cell-substrate friction forces balance the active ones and are mediated by the attachment and detachment of proteins at focal adhesions [75]. This friction is expected to be proportional to the velocity of the cell relative to the substrate and, in a first approximation, cell–substrate friction is often modeled as a viscous damping force with a coefficient that reflects cell–substrate adhesion [35].

Cell-cell interactions can also be described using four different types of intercellular forces. The first is the cell-cell adhesion. Especially relevant for tissues, this force is mediated by specific transmembrane protein complexes, which build cell–cell junctions that physically link the actomyosin cortices of the adhering cells, thereby enabling force transmission between them [55]. Cell–cell junctions endow tissues with cohesion energy and surface tension, as well as with a bulk modulus. Thus, different modeling frameworks account for cell–cell adhesion by either an interfacial energy contribution, a short-range attraction that opposes cell–cell detachment, or a tissue bulk modulus [87]. Since cells are adhered, friction will also play a role as they move past each other. Cell–cell friction is based on the sliding, turnover, and attachment kinetics of cell–cell junction proteins [55]. This friction is usually modeled as a shear force proportional to the relative velocity between the cells or, in tissue-level descriptions, as shear viscous stresses. Aside from attraction, cells also repel each other. Cell compression is resisted by the cytoskeleton elasticity, which, in epithelial monolayers, gives rise to an area compressibility [140]. This interaction can also lead to more extreme behavior like cell insertion or extrusion which directly influences the monolayers area [26, 134, 141–143], but these effects will not be explored in the context of this thesis. Lastly, active cell-cell forces are generated by myosin molecular motors in the cytoskeleton and transmitted through cell–cell junctions. The cell cortex and the apical actin belt generate a roughly isotropic tension at the cell scale, thus giving rise to isotropic active stress at the tissue level. However, migrating cells are polarized, and hence their cytoskeleton exhibits highly anisotropic structures such as stress fibers which generate anisotropic tension and give rise to anisotropic active stresses at the tissue scale [144, 145]. Due to this high level of anisotropy, some models only take it into account when it is introduced explicitly in the models framework, while others consider it isotropic for simplicity [23].

The orientation interaction between cells might be one of the most debated and, depending on the model, can vary wildly on its interpretation. The problem lies in the fact that the orientation of the cells can be changed through a variety of different methods, either from cell-cell interations or cell-substrate ones [35]. The most prominent ones are polarity alignments, where cells tend to align their polarities and is often explicitly implemented via either Vicsek-like rules, torques on cell polarity or orientational stiffness of the polarity field in continuum models [20, 87]. Cells also tend to align with the flow induced in the tissue, shear tissue flows reorient cell polarity in the fly wing [146], as well as the cell division axis in epithelial monolayers [147]. Cell polarity-shape alignments have also been discussed in previous works [35, 87, 148]. There are also several processes whereby cells tune their migration direction upon contact interactions with other cells, which is sometimes termed contact regulation of locomotion [23]. Lastly, the polarization of the cells can also be influenced by the substrate. This can be through a substrate induced polarization given that cells exert larger tractions on more adhesive substrates and thus, gradients of substrate adhesivity/stiffness can polarize cells (durotaxis) [47, 70, 96, 149]. Through their interaction with the substrate, cells may be able to align their polarity to their velocity, thus tending to align self-propulsion with drag cell–substrate forces [51]. This can induce a polarity-velocity alignment. Although used in some models, this interaction is still poorly understood due to the dominance of cell–cell interactions in cell monolayers [23, 35, 87].

Due to the complexity of the interactions, models should be properly coarse-grained to take into account the relevant ones when trying to describe a specific phenomenon. The more interactions one takes into account the more difficult it is to grasp the model itself and understand which interactions play a relevant role. As such, multiple models have been proposed to tackle different problems in cell monolayers. From single particle descriptions to continuum models, each one excels at different levels [23, 87]. For example, single particle descriptions have been developed for several years to describe collective motion in large aggregates of cells, but usually fail at taking cell-cell adhesion into account or fail at describing the mechanics of cell tissues as the relevant length and time scales are out of reach [20, 35, 88]. On the other end of the spectrum, continuum models are often more analytically tractable which can yield insights into the problem without having to explore the parameter space in simulation, but cell–cell interactions are not implemented at the cellular level but rather encoded in phenomenological couplings whose relationship to cellular processes may be unclear [33, 34, 132]. Others lie in the middle, like Phase Field models, or lattice models like the Cellular Potts model [23]. In this thesis, we focus on a specific family of models, the active network models [45, 46]. With roots in the study of foams [150], network models have been adapted to describe cell monolayers where each cell has a polygonal shape [42,44]. Although not as detailed as the Cellular Potts model or Phase Field models they still have been able to capture some relevant geometrical properties of tissues [76, 82,94]. A current limitation of network models is that they account for neither internal dissipation nor anisotropic active stresses in the tissue. Recent efforts to include cell–cell friction [151] and to relate network geometry to the tissue stress tensor [152] offer possible ways to address these limitations.

This family of models can be divided into two subtypes, the Vertex and the Voronoi models. When describing cell monolayers, both consider that cells have a regular polygon shape. The Vertex model uses the vertices of the polygons as degrees of freedom, while the Voronoi model uses their geometrical center as degrees of freedom and makes use of the Voronoi tessellation of these points to extract the shape of the individual cells [2, 83]. Given the disparity in the degrees of freedom, both models will differ on how the topological changes to the network are performed. While in the Voronoi model, topological changes are carried automatically through the tessellation, in the Vertex model they need to be introduced explicitly [45]. Both models have been studied in 3D [61,62,153] and 2D [2,22,45,46,83]. Although the 3D Voronoi model shows interesting properties that have been used to highlight the uniqueness of these network models [61, 62], the shape of the cells becomes too unnatural when comparing to typical cell monolayers. Due to the Voronoi tessellation, the cells will have a spherical shape which conflicts with the typical columnar shape seen in epithelial tissues, and thus Vertex models are usually used to describe the tissues in 3D [153]. Since the degrees of freedom are in the vertices of the polygon, there is more freedom to model the shape of the cells and make a proper columnar tissue. Furthermore, this also allows for a more detailed description of the cell by separating the dynamics of its apical and basal sides, which can be of relevance for some studies [93,153]. In our case, we will be focusing on 2D models. For the applications we aim for, the height of the monolayer does not play a relevant role and as such we do not need to take into account the apical and basal sides explicitly [55]. Thus, all the relevant dynamics will be at the level of the cross-sectional area of the tissue. Both the Vertex and Voronoi models are usually described, in the cell monolayer context, by an energy functional [2,45,46,83],

$$E_i = K_A[A_i - A_0]^2 + \Lambda P_i + \Gamma P_i^2 \ , \tag{2.1}$$

where A_i and P_i are the area and perimeter of cell i, respectively, and A_0 is the target area value. The first term accounts for the cell incompressibility and the resistance to height fluctuations. The second term accounts for the effective cell membrane tension, due to cell-cell adhesion and cortical tension, while the third term accounts for the active contractility of the actomyosin subcellular cortex. This term is a key difference between models of tissues and foams; for the latter, Λ is always positive and the quadratic perimeter term is absent [150]. K_A is the area moduli, Λ is the line tension of the cell–cell interfaces and Γ is related to the strength of the contractility.

2.2 The 2D Self-Propelled Voronoi model

In this thesis, we focus primarily on the 2D Self-Propelled Voronoi model. The differences in implementation between the Voronoi and Vertex models are explained in the following subsection and we also give a general overview of the relevant results in the literature from the two models.

We model the confluent tissue as a monolayer of N cells (Fig. 2.2). Each cell i is represented by its center $\mathbf{r}_i$ and its shape is given by the Voronoi tesselation of the space. The stochastic trajectories

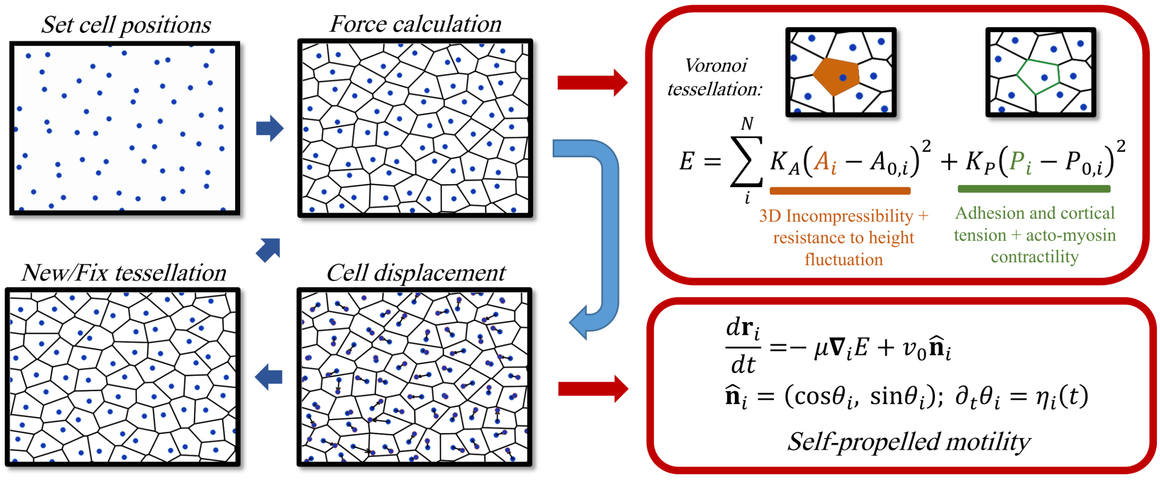

Figure 2.2: Schematic representation of the rules of the model. On the left are snapshots of the different steps of the simulation. First, one distributes points in a box corresponding to the centers of the cells. Then, the interactions are calculated using the energy functional Eq. (2.5), where the area and perimeter of the cells are calculated using the Voronoi tessellation. The cells are then displaced using an overdamped Langevin equation of motion (Eq. (2.2)), which takes into account an interaction term and a self-propelled term, that describes in a simplified way the front to rear polarization of the cells. The last step of the simulation is tasked with calculating the new network topology of the tissue.

of cells are obtained from a set of overdamped Langevin equations of motion,

$$\frac{d\mathbf{r}_i}{dt} = \mu \mathbf{F}_i + v_0 \hat{\mathbf{n}}_i, \tag{2.2}$$

where $\mathbf{F}_i$ is the net force acting on cell i, μ is the mobility of the cell, v_0 the self-propulsion speed, and $\hat{\mathbf{n}}_i = (\cos\theta_i, \sin\theta_i)$ is a polarity vector which sets the direction of the self-propulsion force. For simplicity, we consider that θ_i is described by a Brownian process given by,

$$\dot{\theta}_i = \eta_i(t),\ \langle \eta_i(t)\eta_j(t')\rangle = 2D_r\delta(t-t')\delta_{ij}, \tag{2.3}$$

where $\eta_i(t)$ is an uncorrelated random process of zero mean and its variance sets the rotational diffusion D_r. This is a simplistic way of introducing the front to rear polarization of the cells explored previously [23, 87].

The net force $\mathbf{F}_i$ describes the multibody cell-cell interaction and it is given by $\mathbf{F}_i = -\nabla_i E$, where $E = \sum E_i$ is the energy functional for the whole tissue and E_i is the energy functional for each cell i as shown in Eq.(2.1) [45, 46]. The gradient operator $\nabla_i = \partial/\partial \mathbf{r_i}$, where $\mathbf{r}_i$ are the coordinate positions of cell i. One can further simplify the energy functional,

$$E_i = K_A[A_i - A_0]^2 + K_P[P_i - P_0]^2 \ , \tag{2.4}$$

where A_i and P_i are the area and perimeter of cell i, respectively, and A_0 and P_0 are their target values. The first term accounts for the same effects as described previously. The second term accounts for both the active contractility of the actomyosin subcellular cortex and effective cell membrane tension, due to cell-cell adhesion and cortical tension. K_A and K_P are the area and perimeter moduli. There is an additional constant term when compared to Eq. (2.1), which vanishes when the forces are calculated. Since we use periodic boundary conditions with a fixed box size, the preferred area, A_0, only renormalizes the pressure and does not affect the forces between the cells [61, 137]. Thus, without loss of generality, we set $A_0 = \bar{A} \equiv (\sum_i A_i)/N = L^2/N$ and adimensionalize the model using the length $\sqrt{\bar{A}}$ and the energy $K_P\bar{A}$ units, leading to the dimensionless energy:

$$e_i = k_A(a_i - 1)^2 + (p_i - p_0)^2 \ , \tag{2.5}$$

with four adimensional quantities: two that characterize the area and the perimeter of the cell ($a_i = A_i/\bar{A}$ and $p_i = P_i/\sqrt{\bar{A}}$), a shape parameter $p_0 = P_0/\sqrt{\bar{A}}$, and the ratio $k_A = K_A\bar{A}/K_P$.

2.2.1 The 2D Vertex model

The Vertex and Voronoi model share the same energy functional given by Eq. (2.1), the difference being the way they are calculated since in the Voronoi model the area and perimeter of the cell is given by the Voronoi tessellation of the degrees of freedom, while in the Vertex model these are the vertices, and the area and perimeter are calculated through the edges of the network which connect the different vertices to form the cells [45]. The main difference is in the self-propulsion term. Some studies consider the simplest case where each vertex moves with Brownian motion, where $\hat{\mathbf{n}}_i$ becomes a simple white noise term. More recent studies have introduced a self-propulsion term by considering an effective energy similar to Eq. (2.1) but with an additional term related to the self-propulsion,

$$E_i = K_A[A_i - A_0]^2 + \Lambda P_i + \Gamma P_i^2 - \gamma v_0 \sum_{cells-a} \hat{\mathbf{n}}(\theta_a) \cdot \mathbf{r}_a \tag{2.6}$$

where $\mathbf{r}_a$ is the geometrical center of the cell and γ the substrate friction. The last term is a sum on all vertices belonging to a given cell a. In this way, when taking the gradient of the energy, the equations of motion become identical to those of the SPV model [98].

Another major difference comes in the way topological changes to the network are handled. In the SPV model, topological changes are carried automatically through the tessellation. In the AVM or BVM they need to be introduced into the model explicitly. These are usually termed $T1$ transitions, which correspond to the process through which cells exchange neighbors. In practice, this is carried out by checking if after each timestep there is any edge in the network with a length smaller than a given threshold l_a. If so, a $T1$ transition is performed, in which two vertices sharing a short edge merge into a single vertex, which then decomposes into two new vertices, forming an edge perpendicular to the previous one, such that the local network topology is changed [45].

2.3 Rigidity transition and anomalous glassy dynamics

Recently it has been reported that both the Vertex and Voronoi models undergo a rigidity transition at a threshold value $p_0 \approx 3.81$ [2, 83]. In the Vertex model, this transition is accompanied by a reduction of the shear modulus of the tissue for $p_0 < 3.81$, vanishing for values above this threshold [83]. In the Voronoi model, this transition was characterized using the diffusion coefficient of the tissue which increases substantially close to the same critical point [2]. In both models the phenomenology of the transition is similar, for $p_0 < 3.81$ the tissue is in a rigid phase where cells are caged by their neighbors. The energy barriers for cell rearrangement are large and the tissue is arrested [22]. In this phase, the edges of the cells are under large tensions, referred commonly as residual stresses, and are not able to decrease sufficiently in length such that a $T1$ transition, or a cell neighbor exchange, occurs. For $p_0 \geq 3.81$, the residual stresses decrease significantly and cells are able to adopt more asymmetrical shapes. This is accompanied by a reduction of the energy barriers and the tissue is able to flow. This new phase is the fluid-like phase [2,22,83]. Figure. 2.3 shows how

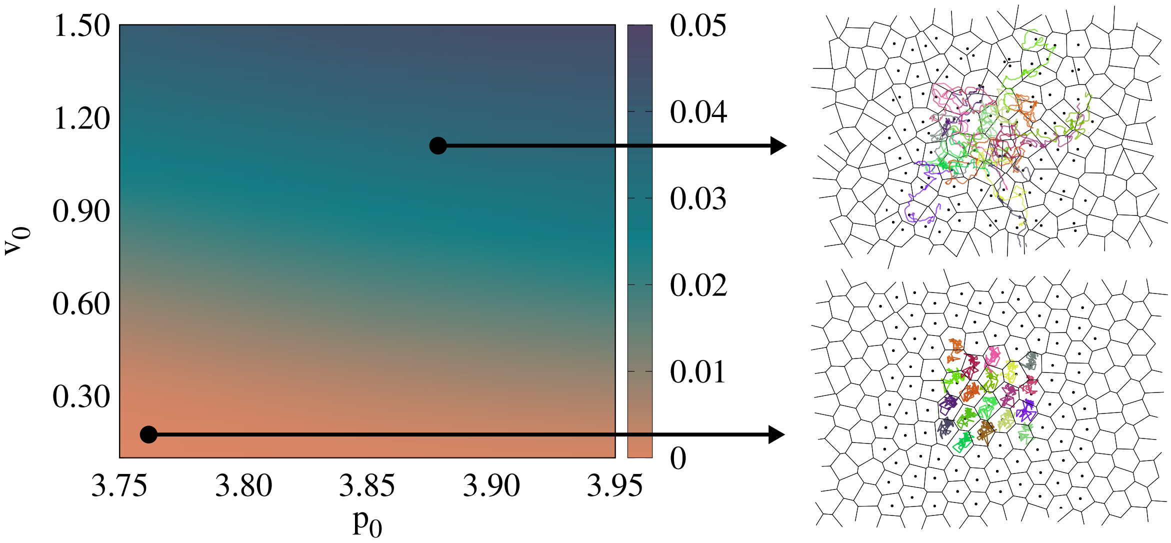

Figure 2.3: Heat map of the diffusion coefficient of the tissue for different p_0 and v_0. As shown in previous studies [2], the diffusion coefficient increases with p_0 or v_0. For low values of these parameters, the cells are caged by their neighbors and the tissue is arrested. As p_0 or v_0 increase, the cells break free from their cages and move more easily throughout the tissue. On the right are snapshots of the tissue and sample trajectories of the cells corresponding to the two different phases.

the diffusion coefficient of the tissue in the SPV model changes as a function of p_0 and v_0 (similar to Ref. [2]). We observe an increase of the diffusion coefficient as the tissue enters the fluid phase as shown in previous studies.

Aside from the rigidity transition, both models show anomalous glassy dynamics when compared to more typical glassy systems like colloids or granular matter [80]. In Ref. [84], the glassy dynamics of the Brownian version of the Voronoi and Vertex models was studied. It was found that the low-frequency modes are collective, rather than the quasi-localized modes typically seen in particulate glasses. Furthermore, the models display *sub-Arrhenius* scaling of the relaxation time as the temperature is lowered, suggesting that either typical glassy energy barriers decrease in colder glasses, or that a local picture of activated dynamics, characteristic of particulate glasses, does not hold. It is also heavily hinted that nonlinearities are a key to understanding structural length scales in these models.

Although both models have quite similar dynamics, they diverge substantially in the athermal regime (no activity or temperature). As observed in Ref. [154], the 2D athermal Voronoi model, parameterized by Eq. (2.5), does not have a rigidity transition around the critical value ($p_0 = 3.81$), and is rigid throughout the parameter space explored. It was also suggested, using larger simulations, that in the SPV model (with activity), the critical point no longer plays a special role (the values do not converge at this point), and that the implied dynamical transition is a strong function of D_r. This is consistent with the decoupling of the glass and jamming transitions observed in self-propelled particle models [106]. By contrast, for the special case $k_A = 0$, where there are more degrees of freedom than constraints, a mechanically floppy regime was reported with a rigidity transition close to that observed in the 2D Vertex model. Similar to the 3D Voronoi model and the 2D Vertex model, this transition is also followed by a substantial decrease of the residual stresses [61, 62].

These results suggest that it is possible to distinguish these models depending on the number of constraints. On one hand, the underconstrained models, like the 2D Vertex model, 3D Voronoi model or 2D Voronoi model with $k_A = 0$, exhibit a clear rigidity transition driven by the presence of residual stresses [61, 62, 110]. On the other hand, the 2D Voronoi model with $k_A > 0$, which is marginal (number of degrees of freedom equals the number of constraints) [109], is always rigid, with a dynamical transition similar to self-propelled particle models when activity or temperature is introduced in the equations of motion [84, 106, 154].

Recent studies have worked towards unifying the rigidity in underconstrained models using a minimal length approach [61, 62, 110]. These systems are rigid due to geometrical incompatibility. Similar to a guitar string, before it is tightened, the floppy string is underconstrained, with fewer constraints than degrees of freedom and there are many ways to deform the string at no energetic cost. As the distance between the two ends is increased above the rest length of the string, this geometric incompatibility together with the accompanying creation of a self-stress rigidifies the system and any deformation will be associated with an energetic cost. Just as with the guitar string, the description of the geometry given by a minimal length then allows one to calculate many features of the elastic response, including the bulk and shear moduli [62]. In the 2D Vertex model this minimal length corresponds to a given preferred perimeter, p_0, while for 3D is a surface area. Even more recent work [110] further emphasis this idea and introduces the concept of energetic rigidity to these models. They suggest that standard constraint counting is not enough to predict the onset of rigidity, it is required for small displacements to increase the energy of the system for it to be rigid. This result is in contrast to typical particulate models which have focused on rigidity trough constraint counting, when motion preserves constraints [101, 107, 155].

In contrast, the 2D Voronoi model with $k_A > 0$ is marginal and it is still unknown whether the same theory applies. Nonetheless, as pointed out previously, the Voronoi and Vertex models share the anomalous glassy dynamics and although the Voronoi model does not have a rigidity transition in the athermal regime, the shear modulus of the tissue still decreases by orders of magnitude close to the expected thermal transition point [154]. Recent results with the 2D Brownian Voronoi model have also suggested a change in the energy landscape close to $p_0 \approx 3.81$, where there is an emergence of a fractal-like energy landscape and cells become virtually free to diffuse in specific phase space directions up to a small distance [108]. All these results suggest that for high values of p_0, even though the tissue might not be fluid, the rigidity still changes. We explore this in more detail in chapter two.

Aside from the rigidity transition and glassy dynamics, some works have also explored collective cell motion like flocking in these models, by introducing Vicksek-like orientation interactions or similar [23, 156]. Other works have also explored the effects of cell apoptosis and mitosis in the transition [98, 157]. Some studies have introduced a coupling between network geometry and the tissue stress tensor. Due to the anisotropy of the network, this could resolve the problem of the active stresses in the tissue not being anisotropic [92, 97, 158]. Although the simple Vertex model only takes into account simple vertices (shared by three cells), some studies have considered the effects of multi-fold vertices and rosettes in the tissue, observing that these higher order nonlinear terms increase the constraints of the tissue promoting its rigid state [159]. The 3D Vertex model has also garnered some attention due to the possibility of creating columnar like monolayers and being able to separate the apical and basal dynamics [153]. Aside from the standard planar description, recent studies have looked at the effects of curvature in the mechanical properties of the tissue and the rigidity transition, highlighting the effects of curvature in the collective motion of the cells [85, 86]. In chapter four of this thesis, we explore more how heterogeneity affects the rigidity of the tissue, which has been discussed in previous work with significant impact for cancer research [8]. Lastly, we also consider in chapter six the case of a non-confluent tissue which also shows a wide array of

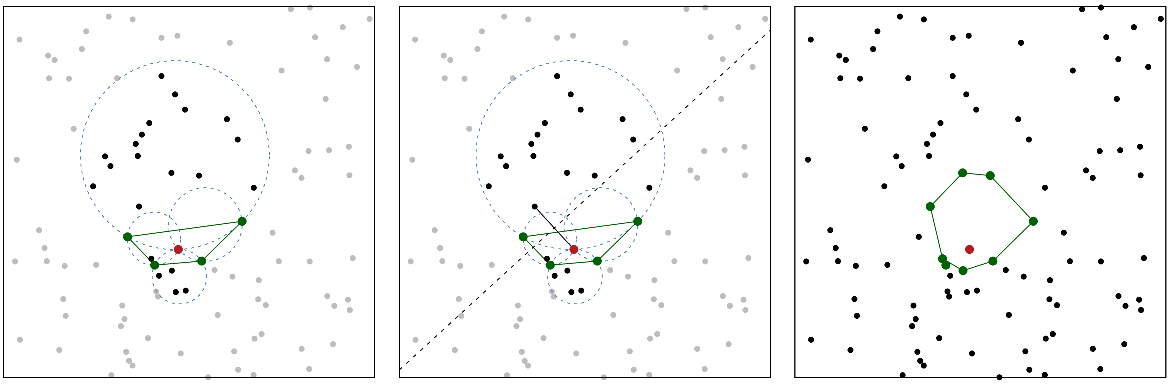

Figure 2.4: Schematic representation of the lemma used for the optimization. The image on the left shows how the local lemma applies to the triangulation of a specific point (red). In green are four points which are chosen as the initial vertices of the trial polygon. The circumcircles are shown in blue and in black are the points that are inside the circumcircles. The lemma states that while there are points inside the circumcircles we have not reached the final Delaunay triangulation. In the middle is a schematic representation of the half plane intersection routine. Here, a point inside a circumcircle is chosen as a trial vertex and a segment is drawn between it and the red point. Then a perpendicular to that line is drawn which divides the box into two half planes. In this case, since there is only one circumcircle center in the same side as the trial vertex, no vertex of the trial polygon is removed and this trial vertex is added to the trial polygon. On the right is the correct Delaunay triangulation.

different phases, starting in a gas-like phase until reaching the fully confluent phase [137, 160].

2.4 Code optimization

To run the simulations we use a C++ code entitled cellGPU. This is an hybrid CPU and GPU code that efficiently simulates a confluent tissue using the SPV model [99]. The routine is a standard molecular dynamics simulation with an Euler integration, and an additional layering which is the Delaunay triangulation. In order to access large system sizes and long time scales, we optimized the existing open source code as follows: previously, this code used a CPU only C++ library named CGAL to compute the periodic Delaunay triangulation of the cell points, which is the dual graph of the one given by the Voronoi tessellation. This library uses a standard edge flipping algorithm to perform this triangulation [3]. Although these pre-established routines are extremely optimized for their task, the constant memory transfers between CPU and GPU hinders the codes performance. Furthermore, since only the Delaunay triangulation of the points are stored at each timestep, it is possible that only local topological rearrangements of this network are needed between successive timesteps, instead of a global triangulation. Since the CGAL routine does not take this into account, it is not optimized for this problem in particular, and given that the Delaunay triangulation is the most demanding task of the whole routine, we decided to implement a GPU and multi-threaded CPU routine that allows for faster local triangulations. Recently, a multi-threaded CPU implementation of the Delaunay triangulation was studied and compared to other state of the art algorithms [161]. It takes advantage of the following local lemma to triangulate the points: given a subset of points X of the entire set N, if the points in X form a closed simple polygon that contains a given point i, then the actual Delaunay neighbors of i are contained in the union of the circumcircles formed by i and each ordered pair of vertices in the polygon. This lemma makes it easier to calculate the Delaunay triangulation since one only needs to look at points closer to i and not to the whole set, thus allowing for local repairs of the topology of the network. We took advantage of the same lemma to develop a

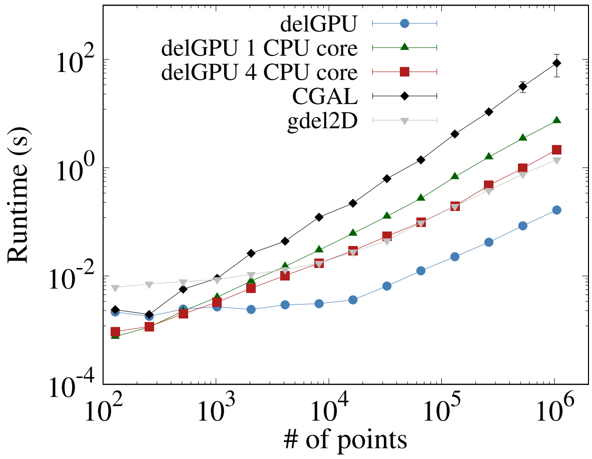

Figure 2.5: Runtime of the Delaunay triangulation code as a function of the number of points used. The runtime is measured in seconds and for all methods used, the initialization time was removed from the total in order to take into account the relevant time for triangulation. We compare between different CPU and GPU implementations. delGPU is our implementation and we show its runtime when using the GPU, the CPU with one core and with four cores. CGAL is used as a CPU implementation with only one core [3]. gdel2D is a GPU implementation as described in Refs. [4,5]. All results were averaged through 100 different samples. The hardware used for the CPU is a AMD Ryzen 3 2200g with radeon vega graphics, while for the GPU we used a Nvidia GeForce RTX 2080 Ti. These results were calculated using only uniform distributions of points.

GPU routine to use in the simulations of the Voronoi model.

Figure 2.4 shows some of the steps of the implementation, a more thorough explanation is given in Ref. [161]. To find the Delaunay neighbors of a given point we start by creating the trial polygon that encloses the point. We choose to always take a four point trial polygon since, in this way, it becomes less expensive to check relative positions, we only need to make sure that the points are in different quadrants with respect to the point we are trying to triangulate. If a fifth is added we need to check its relative position to the others, while for only three we do not always guarantee that the trial polygon encloses the triangulation point. To find this trial polygon we create a squared grid that divides the simulation box into multiple squares. We choose the grid size such that, on average, there is one point per square grid. We start from the grid square of the triangulation point and search the nearby grid squares, in a spiral like way, until we find four points, one in each quadrant (with respect to the triangulation point). We need to make sure that this trial polygon is regular and convex. As the lemma states, we can create a circumcircle between the triangulation point and each ordered pair of the trial polygon, leading to a total of four circumcircles. If there are no other points inside these circumcircles, the vertices of the trial polygon are the actual Delaunay neighbors, if there are others, the polygon needs to be adjusted. We use a half plane intersection routine, as explained in Ref. [161] to go from the trial polygon to the actual Delaunay triangulation. For a given pair of vertices in the trial polygon with other points inside its circumcircle, we choose the closest one (the trial vertex) to the triangulation point and run the half plane intersection. First, we calculate the line segment that goes from the triangulation point to the trial vertex. From that line, we calculate another that is perpendicular and intersects it at half its length, which creates two half planes, one which contains the triangulation point and the other which contains the trial vertex. Lastly, we check which circumcircle centers (of the trial polygon) are on the side of the trial vertex. Each polygon vertex generates two different circumcircles. Thus, if there is only one circumcircle center on the half plane of the trial vertex, the trial vertex is added to the trial polygon. If there is more than one center on that half plane, then the vertices which have their two circumcircle centers on the side of the trial vertex are removed and the trial vertex is added to the polygon. This half plane routine is carried out until the final polygon is found. To reduce the redundancy of the method, one can choose to calculate only two triangles per triangulation point, but we chose to calculate the whole triangulation since we needed the full ordered list of Delaunay neighbors to use in the SPV routine.

In Fig. 2.5 we show a comparison between our GPU routine (delGPU) and the single-core implementation used previously in cellGPU (CGAL). We observe that the difference between the two routines increases with the number of points, being almost three orders of magnitude faster to triangulate for larger sets. In this comparison, only uniform point distributions are used since they highlight the strength of this implementation. Furthermore, when using this routine to simulate the Voronoi model, it is probable that a large percentage of the triangulations will be done on uniform point distributions. In Fig. 2.5 we also show a comparison between our implementation and a state of the art routine for the GPU [4, 5].

One of the advantages of this technique is that it allows for a fast and local triangulation of the point set. Thus, aside from the clear optimization resulting from a full GPU implementation, we also have the added advantage of using only local topological changes of the Delaunay triangulation network. For this, we go through each triangle in the Delaunay triangulation and check whether the circumcircle area formed by those three points contains any other point of the $N-3$ set inside. The local topological change only needs to happen if the answer is yes, in which case the three points belonging to that triangle need to be updated.

Chapter 3

Hierarchical structure of the energy landscape in the Voronoi model of dense tissue

The Voronoi model is a popular tool for studying confluent living tissues. It exhibits an anomalous glassy behavior even at very low temperatures or weak active self-propulsion, and at zero temperature the model exhibits a disordered solid structure with no evidence of a rigidity transition. Here we investigate the properties of the energy landscape in this limit. We find two disordered solid phases that have similar structural features but that differ in the ultrametricity of their energy landscapes; the crossover between these two states shares properties of a Gardner transition. We further highlight how the metric used to calculate distances between configurations influences the ability to detect hierarchical arrangements of the basins in the energy landscape.

3.1 Motivation

Understanding the collective behavior of cells in biological tissues has become one of the major interdisciplinary challenges of recent years, with applications ranging from wound healing to cancer treatment [53, 64, 65, 74–76]. Both experimental and theoretical efforts have been crucial in understanding the properties of these tissues and the mechanisms by which tissue properties are regulated, for example in the way that tissues can transition from rigid to flexible as the properties of individual cells are regulated [28, 63, 76–78, 94, 116]. Rigidity transitions are also seen in particulate systems, such as granular materials and colloidal suspensions, in which changes in particle density and temperature can lead to disordered materials in kinetically arrested jammed or glassy states [79–81]. In living tissues, the nature and properties of the rigid states are still under debate [28, 63, 76, 77], owing both to the explicitly non-equilibrium nature of cellular motion and the many-body interactions found in confluent tissue [16]. These differences raise several challenges to the generalization of ideas and methods developed in the context of well-studied particulate matter [61–65].

Several models have been proposed to understand the collective behavior of cellular systems, from single particle descriptions to density field models [22, 45, 46, 83, 87, 148]. The Voronoi model represents a confluent tissue as a space filling polygonal tiling, where each positional degree of freedom corresponds to a cell whose shape is obtained by an instantaneous Voronoi tessellation [2, 100, 162]. The dynamics is controlled by an energy functional that is quadratic in the area and

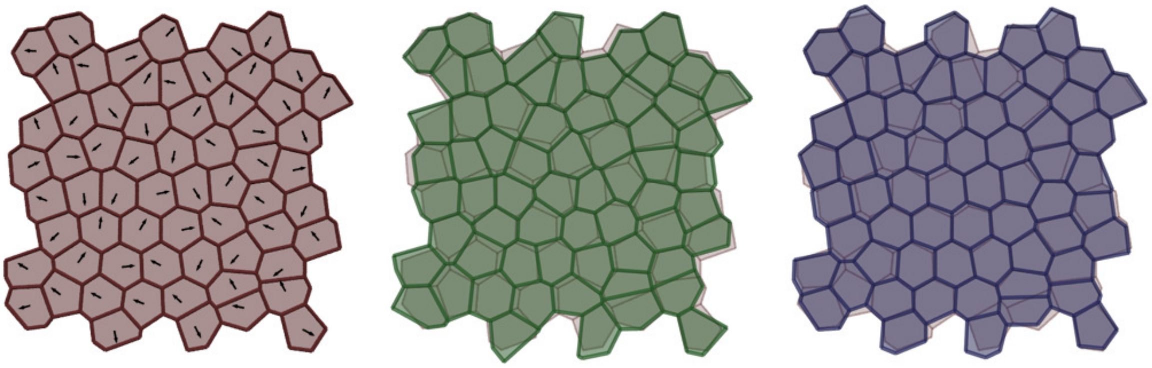

Figure 3.1: Representation of the perturbation protocol. On the left is represented the original minimized configuration (red) with the perturbation vectors in the center of each cell. In the middle is the original minimized configuration (red) and the perturbed one (green). On the right is the original minimized configuration (red) and the one minimized after the perturbation (blue).

perimeter of each cell (described in more detail below), and the mechanical properties of the tissue can be either solid-like or fluid-like depending on the temperature and a shape parameter, p_0, which quantifies the target shape of the individual cells [2].

At zero temperature (or in the absence of cellular activity) it has been argued that the Voronoi model possesses a finite shear modulus over its entire range of model parameters [84]. This is in sharp contrast with particulate systems, in which a zero-temperature rigidity transition can be observed by changing the system density [102, 105, 112, 155]. The particulate jamming transition is typically interpreted in the context of constraint counting, in which the transition occurs when the number of independent particle-particle contacts equals the number of degrees of freedom [109, 163]. As described below, the 2D Voronoi model is always at this point of marginal stability [84], and thus an analysis based only on the balance between constraints and degrees of freedom is insufficient. It has been proposed instead that energetic rigidity, in which not only simple constraints but also residual stresses play a key role [61, 62, 110, 159], is a better framework for understanding Voronoi model rigidity in the athermal limit [110].

Here, we explore this unusual athermal regime of the Voronoi model and show that, even in the absence of a zero-temperature rigidity transition, there is a profound change in the statistics of the energy landscape in different regions of the model parameter space. We find evidence for a transition to an ultrametric, hierarchical arrangement of basins in the energy landscape, suggesting two different phases of a disordered solid [101, 103, 111, 113]. The ultrametric state is characterized by energy minima forming a tree-like structure in phase space where minima within a given sub-basin are much closer to one another than they are to minima in any other sub-basin [102, 112]. This is consistent with a Gardner phenomenology [102, 112]; the phenomenological properties of this phase have been studied in multiple experimental and computational systems [101, 103, 111, 113, 164, 165].

3.2 Methods

We model the confluent tissue as a monolayer of N cells [2, 22, 83] in a square domain of side-length L with periodic boundary conditions. Each cell i is represented by its center $\mathbf{r}_i$ with a shape given by an instantaneous Voronoi tessellation of the space. We choose the unit of length to be given by the square root of the average area of all the cells. We can then write a dimensionless version of

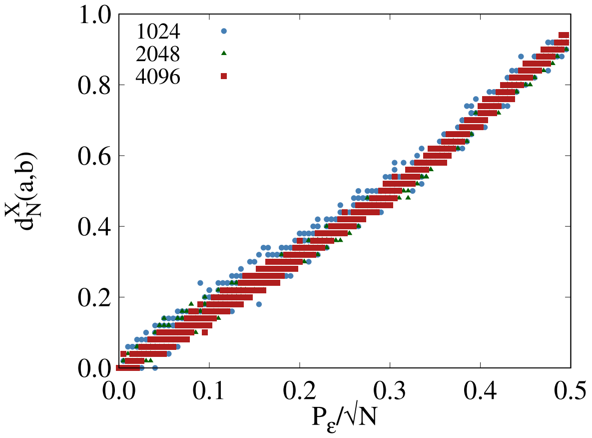

Figure 3.2: Scatter plot of the distribution of normalized metric distance to the original minimum for different norms of the perturbation vector, using the contact metric. The metric distance defined in Eq. (3.2) is normalized by $\sqrt{|a||b|}$, where $|a| = d(a,0)$. For $p_0 = 3.81$, all sizes collapse onto the same curve when using this scaling. We choose $\varepsilon_{max} = 0.5\sqrt{N}$.

the contribution of each cell to the energy functional as [45,46,61,137]

$$e_i = k_A(a_i - 1)^2 + (p_i - p_0)^2. \tag{3.1}$$

Here a_i and p_i are the dimensionless area and perimeter of cell i, p_0 is the target perimeter, and k_A represents the ratio between the relative stiffness of the area and perimeter elasticity of the cell. To simulate the tissue we use cellGPU [99] and initialize N cells distributed randomly in a square periodic box of linear size $\sqrt{N}$ in units of $\sqrt{\bar{A}}$. We consider a monodisperse system with $\bar{A} = 1$.

After initialization, the tissue is relaxed using a FIRE minimization algorithm [166]. This relaxation algorithm moves the cell centers at each step in order to minimize the energy, described by the functional form given in Eq. (3.1). The algorithm uses the standard Molecular Dynamics equations (with velocity Verlet integration) and two adaptive quantities, the time-step Δt and α, the latter to adjust the integration step and the former to control the velocities. During the relaxation, when an *uphill* in the energy landscape is found, both decrease in order to minimize the amount of time spent there and then increase again when a *downhill* is encountered. For our simulations, we have chosen $\Delta t_{min} = 0.001$, $\Delta t_{max} = 0.1$ and $\alpha_{start} = 0.99$. We have tested other values and have found that they do not affect substantially the minimization procedure. Thus, they were kept the same in all the simulations. The minimization is halted once the maximum force on all cells is less than 10^{-12} in natural units. Due to numerical constraints, we consider $p_0 \leq 3.85$, since it has been shown for athermal systems that, above this value, configurations with multi-fold vertices are obtained which lead to numerical instabilities in the minimization protocol [84]

To probe the structure of the energy landscape, we start from an initial configuration that corresponds to a local minimum and perturb it to find new stable configurations. In our primary perturbation protocol, we displace the position of each cell according to the vector $\overrightarrow{P}_\varepsilon = [X_0, X_1, ..., X_{2N-1}]$, where N is the number of cells, $X_{2i} = \varepsilon\cos(\theta_i)$ is the perturbation to cell i along the x-axis, $X_{2i+1} = \varepsilon\sin(\theta_i)$ is that along the y-axis, and θ_i is a random angle uniformly distributed between 0 and 2π. We considered a random length ε drawn from a uniform distribution between 0 and ε_{max}, to guarantee the possibility of visiting minima in the same and different top-level basins. The norm of the perturbation vector is $|\overrightarrow{P}_\varepsilon| = P_\varepsilon = \varepsilon\sqrt{N}$. After the perturbation, we subtract the global translation of the tissue, and then let the tissue relax to a new minimum. An example of this process is shown in Fig. 3.1; details of alternate "perturb-and-minimize" schemes can be found in

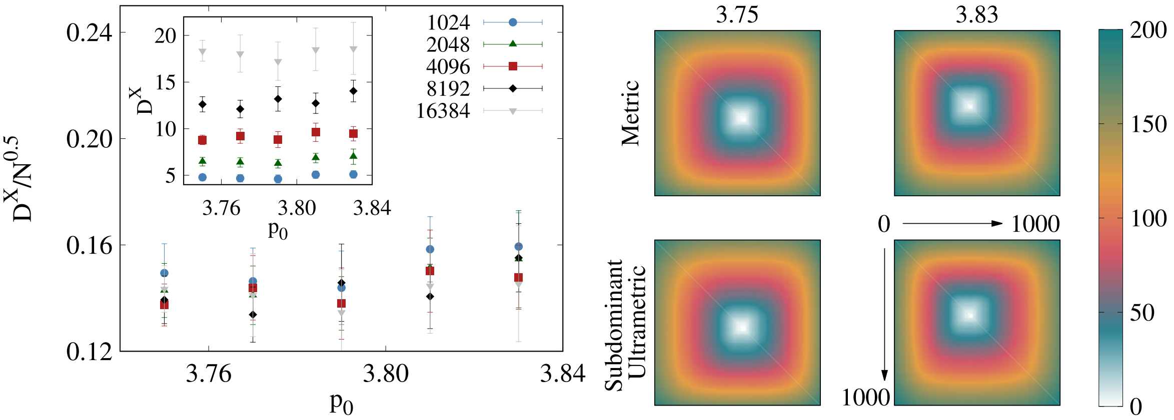

Figure 3.3: Ultrametric structure of the energy landscape using the contact vector metric. (Left) The normalized generalized distance to ultrametricity as measured using the contact vector metric, $D^X/\sqrt{N}$, as a function of p_0, for $N = 1024$, 2048, 4096, 8192, 16384. The inset shows the same results without the scaling. (Right) A schematic representation of the distances between minima according to the contact metric, $d^X(a, b)$, and the subdominant ultrametric constructed from it using a minimum spanning tree [6, 7]. Matrices corresponding to $N = 4096$ and $p_0 = 3.75,\ 3.83$ are shown, where the different distances are grouped using a single-linkage clustering algorithm which clusters the minima sequentially by distance. All results are averages of 10 initial configurations subject to 100 perturbations and minimizations each.

the following sections, where we show that our results are not qualitatively sensitive to these details.

3.3 Results and discussion

We will be exploring different metrics to characterize distances between minima in the energy landscape. To begin quantifying these distances we consider the contact metric (denoted by the superscripted X) discussed in Refs. [103, 111, 113],

$$d^X(a, b) = \sqrt{\sum_{ij} (\vec{C}^a_{ij} - \vec{C}^b_{ij})^2}, \tag{3.2}$$

where $d^X(a, b)$ is the distance between configuration a and b, and $\vec{C}^a_{ij}$ is the 2D contact vector between two cells, where each component $C^a_{ij,x} = x^a_i - x^a_j$ is the distance along the respective axis between cells i and j if those cells share an edge, and $\vec{C}^a_{ij} = \vec{0}$ otherwise. Figure 3.2 shows how the normalized distance to the original minimum ($d^X_N(a, b) = d^X(a, b)/\sqrt{|a||b|}$), using this contact metric, scales with the norm of the perturbation vector applied, computed after subtracting the global translation, where $|a| = \sqrt{\sum_{ij}(C^{ij}_a)^2}$ corresponds to $d^X(a, b)$ for which $C^{ij}_b = 0$. Here, a is fixed and corresponds to the initial configuration, while b is the minimum after the perturbation. We observe that the distance to the original minimum scales approximately linearly with the norm of the perturbation. Furthermore, as in ref. [111], rescaling the perturbation by $\sqrt{N}$ we find the collapse of the curves for different system sizes. To properly parameterize ε_{max}, we need to choose a value that is large enough so that the perturbed configuration does not always relax to the initial minimum but small enough so that we can guarantee that, in principle, any minimum that has some structural resemblance (a normalized distance smaller than one) to the unperturbed one is accessible. We choose $\varepsilon_{max} = 0.5\sqrt{N}$ for all p_0, based on these results.

Figure 3.3 depicts matrices where the color corresponds to the distance between minima, for all pairs of minima found for $p_0 = 3.75$ and 3.83. These matrices were constructed for 10^3 minima obtained for a tissue of 4096 cells. Each element of the matrix corresponds to the distance between

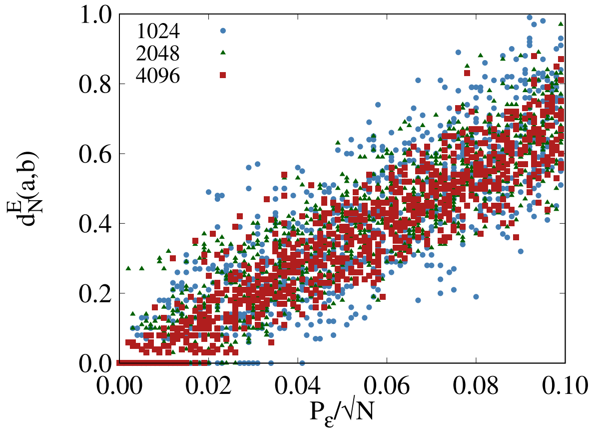

Figure 3.4: Scatter plot of the distribution of normalized metric distance to the original minimum for different norms of the perturbation vector, using the energy metric. The metric distance defined in Eq. (3.2) is normalized by $\sqrt{|a||b|}$, where $|a| = d(a, 0)$. For $p_0 = 3.81$, all sizes collapse onto the same curve when using this scaling. We choose $\varepsilon_{max} = 0.1\sqrt{N}$.

two minima, a and b, given by Eq. (3.2). The distances are sorted using the single-linkage clustering algorithm on the metric of the fully minimized systems, which groups them sequentially based on their relative distance [167]. The colors represent different distances. In white are the minima that are closest to each other. We find groups of minima that are all at this minimum distance, forming a white region that corresponds to sub-basins. The matrices do not show any substantial visual change with p_0.

A Gardner phase is characterized by an ultrametric phase space consisting of a tree-like structure, where minima within a given sub-basin are all much closer to one another than to minima in any other sub-basin. This property is codified by an ultrametric inequality,

$$d^X(a, c) \leq \max[d^X(a, b), d^X(b, c)], \tag{3.3}$$

where a, b and c are three different configurations in phase space and $d^X(a, b)$ is the distance between configurations. To verify if the properties of the tissue are consistent with a Gardner phase, we compute how close the metric is to being ultrametric. To do so, we first find the subdominant ultrametric, $d^<(a, b)$, i.e., the ultrametric that is closest to $d^X(a, b)$ itself. The subdominant ultrametric can be found by first computing the distances in the minimum spanning tree of the space of minima. Then, for each pair of minima a and b, we compute the path between them in the minimum spanning tree and define $d^<(a, b)$ as the largest distance between two neighboring minima along the path [7]. The corresponding matrices are shown in Fig. 3.3.

Having found $d^<(a, b)$, we finally calculate the generalized distance between the metric and the subdominant ultrametric using

$$D^X = \sqrt{\langle (d^X(a, b) - d^<(a, b))^2 \rangle}, \tag{3.4}$$

where $\langle \cdot \rangle$ denotes the average over all pairs of configuration a and b. If $D^X = 0$ then the energy landscape is ultrametric, while $D^X > 0$ quantifies how far it is from ultrametricity. In the inset of Fig. 3.3, we show that D^X increases slightly with p_0, but more importantly it depends strongly on N. In the main plot we re-scale D^X by $\sqrt{N}$ and obtain a reasonable collapse of the data. Since the typical distance between minima and the distance to ultrametricity both scale with $\sqrt{N}$, the space with this contact metric is not ultrametric in the thermodynamic limit [111].

Using distances based on the contact vectors suggests that the landscape of the Voronoi model is not ultrametric, but does the choice of metric itself influence this result? We note that in the

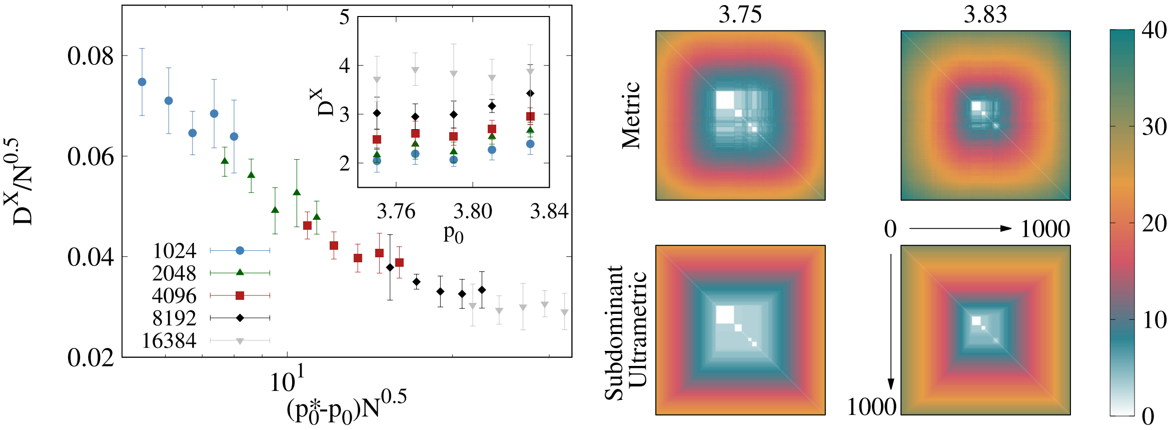

Figure 3.5: Ultrametric structure of the energy landscape using the contact vector metric for small perturbations. On the right is a schematic representation of the distances between minima according to the contact metric and its corresponding subdominant ultrametric. We show the matrices for $p_0 = 3.75, 3.83$, with 1000 different minima and $N = 4096$. The different distances are grouped using a single-linkage clustering algorithm. On the left is a plot of the normalized distance to ultrametricity (Eq. (3.4)) as a function of $(p_0^* - p_0)$, where we have chosen $p_0^* = 3.92 \pm 0.01$, for $N = 1024, 2048, 4096, 8192, 16384$. The inset shows the same results without this scaling. All results are averages of 10 initial configurations subject to 100 perturbations and minimizations each.

Voronoi model, the contact network of the tissue does not change significantly even as the tissue rigidity changes substantially [62, 110]. We further note that the energy functional in Eq. (3.1) is a simple collection of harmonic springs, in a coordinate basis of shape space rather than in the positional basis of the degrees of freedom generating the shapes. This suggests a different metric might be more appropriate, and in this context, we propose one based on the contribution of each cell i to the total energy of the tissue, E_i. We take the same form for the metric as Eq. (3.2), but where $\vec{C}_{ij}^a \to C_{ij}^a = E_i^a - E_j^a$, if i and j are neighbors and zero otherwise. We call this metric the “energy metric”, $d^E(a,b)$. We adopt the same perturb-and-minimize protocol as before, using $\varepsilon_{max} = 0.1\sqrt{N}$ for all p_0 (see Fig. 3.4). As such, we keep biasing the perturbations to nearby minima in the new metric, otherwise more simulations would be needed to probe the same volume of configuration space. In Fig. 3.5 we show that the results using the contact metric remain qualitatively the same using the new ε_{max}. It is possible to see the structure of the basins more clearly but the system still does not appear to be ultrametric. Just like the contact metric, the energy metric scales with system size, $d^E(a,b) \sim \sqrt{N}$, since it depends on the total number of cell-cell contacts. We observe in the inset of Fig. 3.6 that, for the energy metric, the distance to ultrametricity (D^E) does not scale with N and decreases with p_0 (inset of Fig. 3.6). Since the distance between minima scales as $d^E(a,b) \sim \sqrt{N}$, while the generalized distance does not depend on the system size, this suggests that the system does, in fact, become ultrametric in the thermodynamic limit: $D^E/d^E(a,b) \sim 1/\sqrt{N}$.

In the case of the contact metric the calculated values are already normalized since we increase the box size with N, while the typical cell size is fixed. In the case of the energy metric this is no longer the case. Thus, to properly compare the system properties at different p_0 (since $\langle E_i \rangle$ varies with p_0), we also consider a normalized version of the energy metric: $d_N^E(a,b) = d^E(a,b)/\sqrt{|a||b|}$, for which the typical distance between configurations does not depend on either p_0 or N. Figure 3.6 shows the schematic representation of the normalized energy metric, $d_N^E(a,b)$, and its subdominant ultrametric. From this representation, we can already observe changes in the structure of the energy landscape. As p_0 increases, the color gradient is less smooth and the boxes corresponding to the different sub-basins become sharper. Furthermore, it is also observed that more minima fall into the

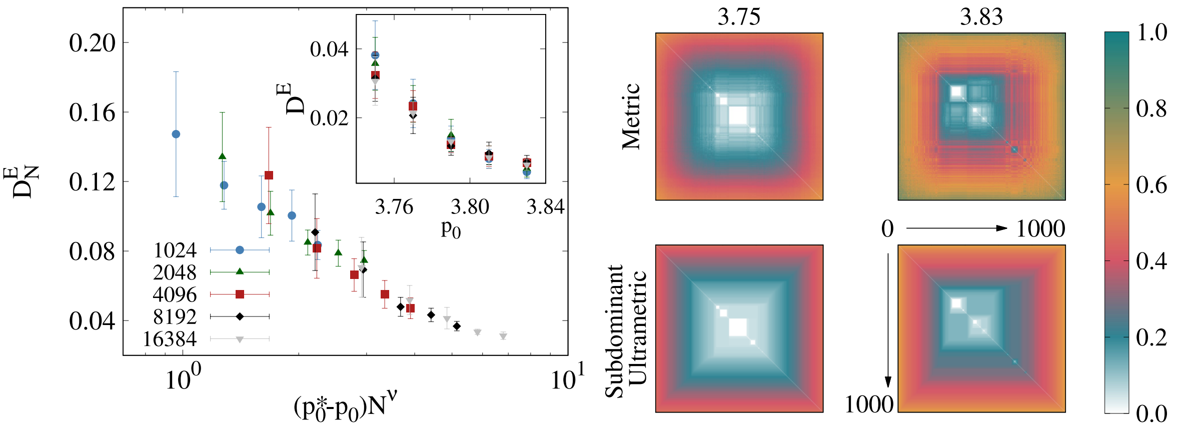

Figure 3.6: Ultrametric structure of the energy landscape using the normalized energy metric. (Left) The normalized generalized distance to ultrametricity as measured using the normalized energy metric, D_N^E, as a function of $(p_0^* - p_0)N^\nu$, for $N = 1024$, 2048, 4096, 8192, 16384, $p_0^* = 3.89 \pm 0.01$ and $\nu = 0.4 \pm 0.01$. The inset shows the generalized distance to ultrametricity, D^E, calculated using the energy metric, $d^E(a,b)$, as a function of p_0, for the same N. (Right) Schematic matrix representation of the distances between minima according to the normalized energy metric, $d_N^E(a,b)$, and its subdominant ultrametric, as in Fig. 3.3. Matrices are shown for $p_0 = 3.75,\ 3.83$ and $N = 4096$. All results are averages of 10 initial configurations subject to 100 perturbations and minimizations each.

same sub-basin. These properties suggest that, when the value of p_0 decreases, the structure of the energy landscape becomes more hierarchical [111].

We also compute the generalized distance to ultrametricity when using d_N^E. Again we see that ultrametricity is approached with increasing system size. Furthermore, with the scaling shown in the main panel of Fig. 3.6 we can collapse the different curves. The values of p_0^* and ν were chosen such that we obtain the best data collapse. Recent work in particulate systems interpreted a similar scaling as a distance to jamming [111, 155]. This suggests not only that the Voronoi model has an ultrametric structure in the thermodynamic limit, but that there is a transition between two different solid phases. Previously, it was shown that the athermal Voronoi model did not have a rigidity transition [84]. Nevertheless, we show that there is a clear difference between the energy landscape for low and high p_0: at low p_0 the glass state is characterized by large residual stresses and an ultrametric energy landscape, and at high p_0 the energy landscape is not ultrametric. We find that the change in the structure of the energy landscape occurs for preferred shape parameters in the range $p_0 = 3.75 - 3.83$, which is close to where the zero-temperature shear modulus changes markedly [84] and where the dynamics at finite temperature changes in character [2, 108, 162].

As p_0 increases, fewer sub-basins are found inside each basin (as represented by the different unconnected clusters in Fig. 3.6), suggesting that the energy landscape flattens out. Another way of exploring this flattening of the energy landscape is by studying the behavior of the model as the relative area modulus k_A is varied. In the limit $k_A = 0$, the Voronoi model is no longer marginally constrained, and it exhibits a residual-stress-based rigidity transition as a function of p_0 at $T = 0$ [84]. As shown in Fig. 3.7, for $p_0 < 3.79$ we find that the tissue is both rigid and the energy landscape is ultrametric. For slightly larger p_0, the energy landscape deviates from ultrametricity and the variance of D_E^N increases significantly. In this regime, the energy landscape consists of a mixture of hierarchical basins and several nearly flat basins and so, in many cases, small perturbations will not drive the system to a different minimum. Due to finite size effects, it is difficult to establish if a new solid phase exists. In the following subsections, we use a simple technique to estimate the transition from the solid to the fluid phase. Using the fraction of configurations with zero energy we

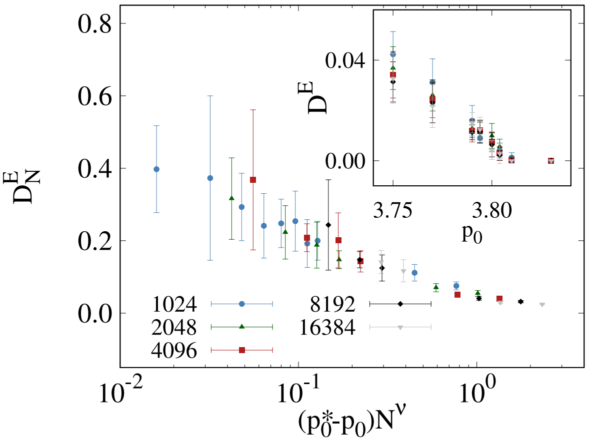

Figure 3.7: A plot as in Fig. 3.6 but for $k_A = 0$, highlighting a similar scaling in the two cases. Here, we use $p_0^* = 3.798 \pm 0.001$ and $\nu = 0.4 \pm 0.01$. All results are averages of 10 initial configurations subject to 100 perturbations and minimizations each.

estimate a transition around $p_0^* = 3.8022 \pm 0.0001$, while in Fig. 3.7, $p_0^* = 3.798 \pm 0.001$ seems to be more appropriate to collapse the data. We used $\nu = 0.4 \pm 0.01$, which was found the best value for the collapse. More simulations would be needed to conclude whether a new solid phase at $k_A = 0$ exists before the fluid phase, or if the observations are finite size effects and both transitions actually coincide. For $p_0 > 3.8$ the energy landscape is flat, characteristic of a fluid-like tissue. For any $k_A > 0$, different energy minima are found for all p_0, consistent with previous work that reported a finite shear modulus for the whole range of model parameters investigated [84]. Although we have not explored the thermal case, recent studies with the thermal 2D Voronoi model also suggest a change in the energy landscape close to $p_0 \approx 3.81$, where there is the emergence of a fractal-like energy landscape and cells become virtually free to diffuse in specific phase space directions up to a small distance [108].

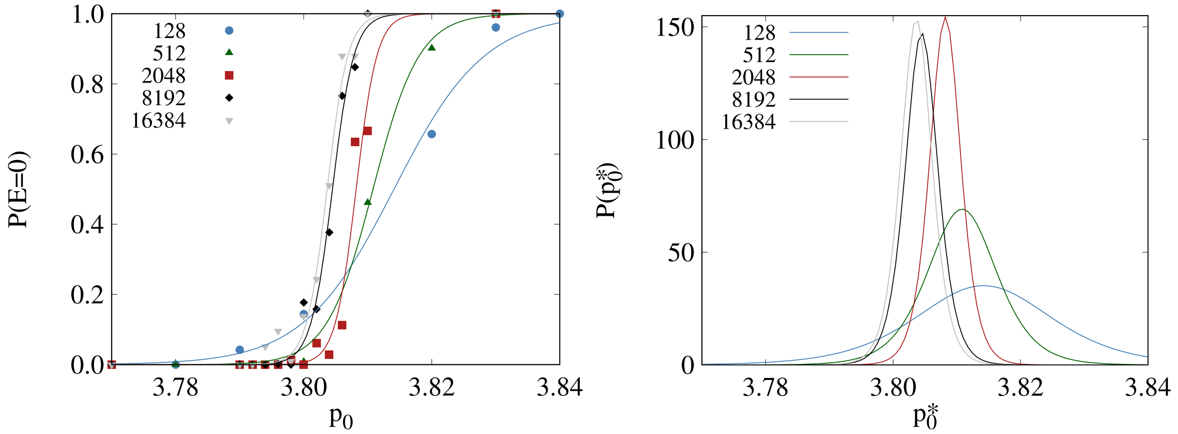

Figure 3.8: Estimation of the rigid to fluid transition point. On the left is plotted the probability of finding a configuration with zero energy, $P[E = 0]$, as a function of p_0 for different N. These results were averaged over 1000 samples. We also show a fit of Eq. (3.8) to the data. On the right is the estimation of the transition point, p_0^*, which is calculated using the peak value of the probability distribution function of the transition points, $P(p_0^*) = \mathrm{d}_{p_0^*} P[E = 0](p_0^*)$.

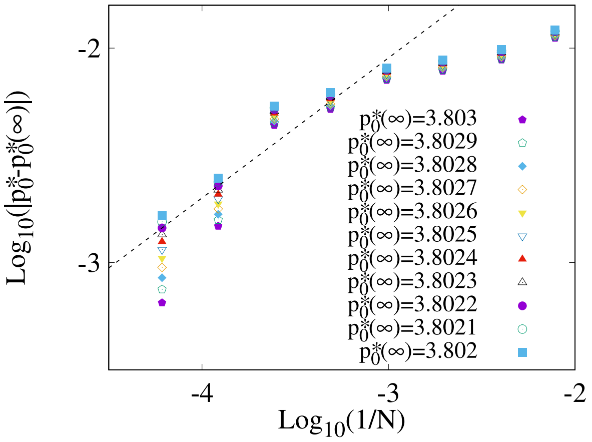

Figure 3.9: Log-log plot of the absolute distance of the estimated transition points for different Ns (from Fig. 3.8) to the thermodynamic value, $p_0^*(\infty)$, as a function of $1/N$. We find $p_0^*(\infty) = 3.8022 \pm 0.0001$ as the value which gives the best linear fit for $N > 1024$ and take it as the estimation of the transition point.

3.3.1 Estimation of the rigid to fluid transition point

To estimate the transition point from a rigid to a fluid tissue we use a technique based on recent work on the vertex model [61]. We use the minimized configurations calculated previously and count the fraction of configurations with zero energy (thus, where there are no residual stresses and for all cells $P_i = P_0$ and $A_i = A_0$), $P[E = 0]$, for different p_0 and N. Since we have less data for the different p_0 than in Ref. [61], we use the following ansatz to fit our data:

$$P[E = 0](p_0) = 0.5\big[1 - \tanh\big(-\frac{p_0 - a}{2b}\big)\big], \tag{3.5}$$

where a and b are fitting parameters. Even though we do not expect that the actual function is Eq. (3.5), it is a good approximation for the N explored here. By using this function we are able to differentiate it and calculate the probability distribution of the transition points, $P(p_0^*) = \mathrm{d}_{p_0^*} P[E = 0](p_0^*)$, from which we can extract the peak value corresponding to the (probable) transition point p_0^* for a given N. Figure 3.8 shows how $P[E = 0](p_0)$ increases with p_0 and the corresponding fit given by Eq. (3.5), which are in good agreement. The right plot shows the derivative of Eq. (3.5) as a function of p_0^*. We use the value corresponding to the peak of the distribution to estimate the transition points for the different N.

To estimate the transition point in the thermodynamic limit we find the best linear fit in a log-log plot, of the distance of the estimated p_0^* for each N (given by Fig. 3.8) to the thermodynamic transition point $p_0^*(\infty)$, as a function of $1/N$. Figure 3.9 shows the different curves for multiple $p_0^*(\infty)$ where we estimate the actual value from the best linear fit. We focus only on $N > 1024$ and estimate $p_0^*(\infty) = 3.8022 \pm 0.0001$. Although more simulations and a more appropriate estimation protocol could be used to quantify this value, our simple estimation is close to the one reported in previous work [84].

3.3.2 $k_A \neq 1$

Here we explore the changes to the energy landscape for different k_A. We explore the values $k_A = \{0, 10^{-2}, 10^0, 10^2\}$. For finite k_A a transition to the fluid-like state never occurs and the system is always rigid. Nonetheless, features of a transition between rigid states are still present for all k_A.

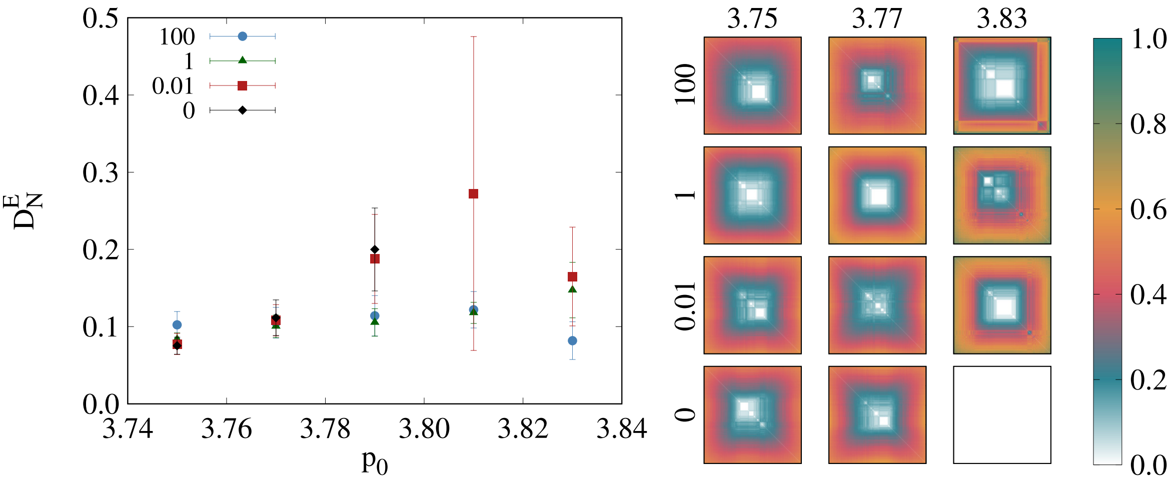

Figure 3.10: Ultrametric structure of the energy landscape using the normalized energy metric for different k_A. (Left) Generalized distance to ultrametricity, for the normalized energy metric, D_N^E, as a function of p_0. Here, we show a comparison between different k_A, using systems with size $N = 1024$. All results are averages of 10 initial configurations subject to 100 perturbations and minimizations each. (Right) Schematic representations of the normalized energy metrics, $d_N^E(a, b)$, of systems with size $N = 4096$, $k_A = 0, 0.01, 1, 100$ and $p_0 = 3.75, 3.77, 3.83$. For $k_A = 0$ and $p_0 = 3.83$ the metrics only show one color since $E_i - E_f \approx 0$ and thus the normalized metric distance diverges.

In Fig. 3.10, we can observe how the different k_A change the hierarchy of the energy landscape, using the generalized distance to ultrametricity (Eq. (3.4)). We find that the results are similar for the different k_A, especially $k_A = 1$ and $k_A = 100$. For $k_A = 0.01$, the variance of D_N^E increases significantly around $p_0 = 3.81$, while for the other systems this is not as pronounced. This is due to the fact that the energy landscape partially flattens and there is coexistence between basins with multiple sub-basins and basins which are almost flat where any (small) perturbation always leads to the same minimum.

Although the variance seems to reduce significantly for $p_0 = 3.83$, this might be due to the presence of multi-fold vertices. Since we are not able to take these vertices into account in our simulations, we have to discard these configurations. This leaves a smaller pool of minima to sample which might lead to smaller fluctuations. The qualitative properties of the different phases described in the main text can be seen in the matrices shown in Fig. 3.10.

3.3.3 Energy metric with similar distance distributions

There is a dependence of the distances explored with p_0 when using the energy metric, with increasing p_0 leading to larger distances. Here, we change ε_{max} for different p_0, in such a way that similar ranges of normalized energy metric distance are explored. In Fig. 3.11 we show how the generalized distance to ultrametricity, D_N^E, changes as a function of p_0, using a constant ε_{max} and a variable one that depends on p_0. We observe that although the values change slightly, the qualitative description of the results remains the same.

3.3.4 Different perturbation protocols

To analyze the sensitivity to the perturbation protocol, we tested different approaches. In addition to the protocol described previously, we introduce two new ones, one based on Gaussian perturbations and another where some skeweness is added.

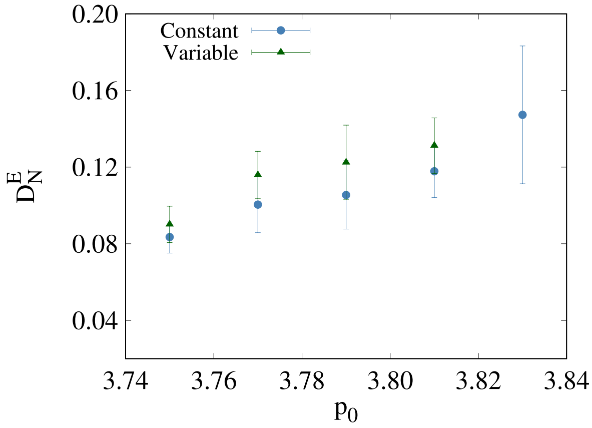

Figure 3.11: Generalized distance to ultrametricity, for the normalized energy metric, D_N^E, as a function of p_0, for $N = 1024$. All results are averages of 10 initial configurations subject to 100 perturbations and minimizations each. The results represent the values measured using the constant ε_{max} as in the main text, and a variable one that depends on p_0.

In the Gaussian perturbation (G), we start by creating a perturbation vector $\overrightarrow{P}_\varepsilon = [X_0, X_1, X_2, X_3,$ ... $, X_{2N-1}]$, where N is the number of cells, $X_{2i} = \mathcal{N}(0,1)$ is the perturbation to cell i along the x-axis and $X_{2i+1} = \mathcal{N}(0,1)$ is the one along the y-axis. Here, $\mathcal{N}(0,1)$ represents a normal distribution with mean $\mu = 0$ and standard deviation $\sigma = 1$. Then we subtract the global translation of the system after the perturbation. Finally, we multiply the perturbation vector by ε, which is a uniformly distributed random variable between 0 and ε_{max}. With this formulation, the norm of the perturbation vector will scale as $|\overrightarrow{P}_\varepsilon| = P_\varepsilon = \varepsilon\sqrt{2N}\sigma$.

In the Skewed perturbation (S), we start by defining a perturbation vector $\overrightarrow{P}_\varepsilon = [X_0, X_1, X_2, X_3,$ ... $, X_{2N-1}]$, where $X_{2i} = \mathcal{N}(0,1) + \mathcal{E}(0.5)$ is the perturbation to cell i along the x-axis and $X_{2i+1} = \mathcal{N}(0,1) + \mathcal{E}(0.5)$ is the one along the y-axis. Here, $\mathcal{E}(0.5)$ represents a Poisson distribution with rate $\lambda = 0.5$. Then we subtract the global translation of the system after the perturbation. Finally, we multiply the perturbation vector by ε, which is a uniformly distributed random variable between 0 and ε_{max}. By adding a Poisson distribution, we are skewing the positive Gaussian tail. With this formulation, the norm of the perturbation vector will scale as $|\overrightarrow{P}_\varepsilon| = P_\varepsilon = \varepsilon\sqrt{2N(\sigma^2 + 1/\lambda^2)}$.

In Fig. 3.12 is represented the generalized distance to ultrametricity, D_N^E, as a function of p_0, calculated using multiple perturbations to the same minimum. The maximum perturbation displacement was fixed at $\varepsilon_{max} = 0.1\sqrt{N}$ for all protocols. We observe that the different perturbations do not lead to different results and thus the range of distances found will only depend on the norm of the perturbation vector.

3.4 Conclusion

In summary, we have found indications of a hierarchical structure of the energy landscape in a model of dense biological tissue whose zero-temperature rigidity is quite different from that of constraint-based particulate systems. Strikingly, we find that the choice of metric to characterize distances between minima is crucial: defining distance based on changes in neighboring contact vectors vs contributions to the energy give *qualitatively* different interpretations of the structure of the energy landscape. In particulate systems, the contact vectors enter explicitly in the relevant energy functional – i.e., the energy of a soft harmonic repulsion or a Lennard-Jones interaction is a simple function of the contact vector between interacting particles. In Voronoi models, the energy

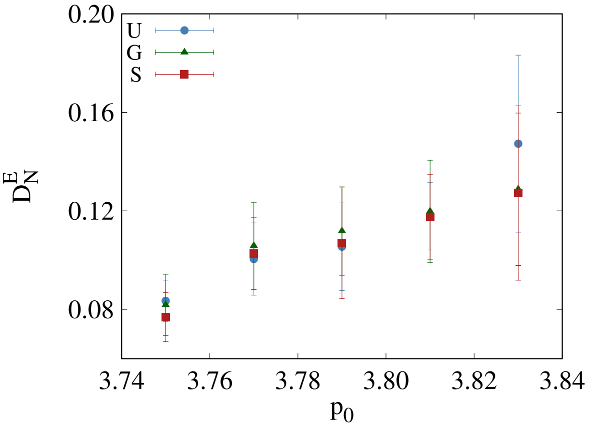

Figure 3.12: Generalized distance to ultrametricity, D_N^E, as a function of p_0 for the different perturbations, using the normalized energy metric, $d_N^E(a, b)$. U represents the uniform perturbation described previously. The size of the system is $N = 1024$ and $\varepsilon_{max} = 0.1\sqrt{N}$ for all. The individual parameters of the perturbations are summarized in the text.

cannot be decomposed into independent pairwise contributions, which we speculate is the reason that choosing a distance metric based on the total energy associated with each degree of freedom is required to reveal the hierarchical structure of the landscape. We further speculate that this may point more generally to the importance of the choice of metric for systems in which many-body interactions dominate over pairwise ones. An avenue for future research could be relating these tissue-like systems to particulate ones, such as soft or hard spheres [111, 113]. This could be done by establishing the relation between the effects of p_0 in the Voronoi model and pressure in particulate systems. Since both exhibit an ultrametric landscape, this could allow a generalization of glassy physics outside of particulate systems and glass-forming materials [80, 81, 112].

Chapter 4

Substrate disorder promotes cell motility in confluent tissues

In vivo and *in vitro* cells rely on the support of an underlying biocompatible substrate, such as the extracellular matrix or a culture substrate, to spread and proliferate. The mechanical and chemical properties of such structures play a central role in the dynamical and statistical properties of the tissue. At the cell scale, these substrates are highly disordered. Here, we investigate how spatial heterogeneities of the cell-substrate interaction influence the motility of the cells in a model confluent tissue. We use the Self-Propelled Voronoi model and describe the disorder as a spatially dependent preferred geometry of the individual cells. We found that when the characteristic length scale of the preferred geometry is smaller than the cell size, the tissue is less rigid than its homogeneous counterpart, with a consequent increase in cell motility. This result is in sharp contrast to what has been reported for tissues with heterogeneity in the mechanical properties of the individual cells, where the disorder favors rigidity. Using the fraction of rigid cells, we observe a collapse of the motility data for different model parameters and provide evidence that the rigidity transition in the model tissue is accompanied by the emergence of a spanning cluster of rigid cells.

4.1 Motivation

The idea of growing artificial cell tissues and organs has been around for several decades [168, 169]. This has spurred a truly multidisciplinary effort to understand the mechanisms responsible for the development of cell tissues and to search for novel strategies to tune the shape and mechanical properties of the tissue. Among those strategies is the use of biocompatible substrates [168,170,171]. An extensive body of research shows that the cell morphology and dynamics are sensitive to the physical and chemical properties of their underlying structure, be it the extracellular matrix or a culture substrate [47–54,64]. For example, it has been shown that the substrate stiffness can significantly affect the geometry of cultured cells, including their spreading area [54,114], volume [115], and shape elongation [116]. The mechanical properties of cells have been shown to change when they adhere to substrates due to the influence of cell-matrix adhesion complexes. For example, cells adhered to rigid substrates develop stresses at the level of the actin network which lead to polarization [131]. Recent studies have also shown that the nanotopography of the substrate can significantly change the cell shape and motility [68–71]. Thus, irrespective of the biological effects, the physical interaction between the cells and their supporting structure plays a critical role in the mechanical properties of the tissue. This poses a great challenge due to the typical level of disorder involved [172–174].

Both *in vivo* and *in vitro*, the epithelial layer of cells is supported by a complex polymeric structure, the extracellular matrix (ECM), which constrains the collective behavior of the tissue [47, 117–120]. For example, it has been observed that cancerous cells alter the ECM in order to promote invasion through healthy tissue [175, 176]. The tumor microenvironment supports diverse mechanical and biochemical interactions during cancer progression, which plays a significant role in the degree of tumor malignancy and metastatic potential [177,178]. Tumors act as local sources of ECM remodeling, resulting in heterogeneous spatial profiles of the ECM network [179]. These profiles can then influence the migration of surrounding cells [180]. By generating cell-scaled tracks along migratory paths, cells will not need to squeeze through or clear constrictive mechanical barriers [180]. Thus, although the ECM is often quantified by bulk metrics, it has a high degree of heterogeneity, which in turn influences the tissue itself, in a way that is largely unclear.

Despite the broad range of physico-chemical processes, which in many cases are system dependent [169], there are convincing arguments that simple, mechanistic models can provide valuable insight into the dynamics of living systems [23, 45, 46, 87]. Several models have been proposed to understand their collective behavior, from single particle descriptions to density field models [22, 45, 46, 83, 87, 148, 181, 182]. The Self-Propelled Voronoi model (SPV) has been one of the models of choice to study confluent tissues [2, 162]. The degrees of freedom are the positions of the center of each cell and the cell shape is obtained by Voronoi tessellation [100]. The dynamics is governed by an energy functional that is quadratic in the area and perimeter of each (Voronoi) cell, thus making the interactions truly many body. The mechanical properties of the tissue are either solid or fluid like, depending on the strength of activity and shape parameter, p_0, of the individual cells [2]. The solid-like regime is characterized by a finite shear modulus, while in the fluid-like regime the shear modulus drops significantly [2, 84]. These results agree both quantitatively and qualitatively with experiments on monolayer tissues [76, 78].

Here, we investigate how heterogeneities on the substrate affect the mechanical properties of confluent tissues (see Fig. 4.1 a)). We describe the confluent tissue using the Self-Propelled Voronoi model, with a position-dependent shape parameter to account for spatial heterogeneities in the cell-substrate interaction. Previous works have established that cell shapes change as a function of substrate properties [114] and in turn the cell shape governs the rate of cell diffusion in the tissue [76]. Heterogeneity in the mechanical properties of the individual cells is known to substantially affect cell motility [121, 122]. For example, numerical simulations of the Vertex model suggest that, a heterogeneous distribution of the mechanical properties of individual cells favors rigidity and thus hinders cell motility [8]. This particular type of cell disorder leads to larger tensions between adhered cells, which in turn gives rise to a percolating cluster of rigid cells responsible for the increase in the tissue rigidity. This result sheds light on the dynamics of cancer propagation, for cancer cells are usually softer than healthy ones [123–125]. Here, we show that the opposite behavior is observed when the disorder is on the substrate (position dependent). For values of the characteristic length scale of the disorder lower than the typical cell size, the tissue is less rigid and cell motility is enhanced.

4.2 Methods

We model the confluent tissue as a monolayer of N cells using the Self-Propelled Voronoi model [2]. Each cell i is represented by its center $\mathbf{r}_i$ and its shape is given by an instantaneous Voronoi tessellation of the space. The stochastic trajectory of each cell is obtained by solving a set

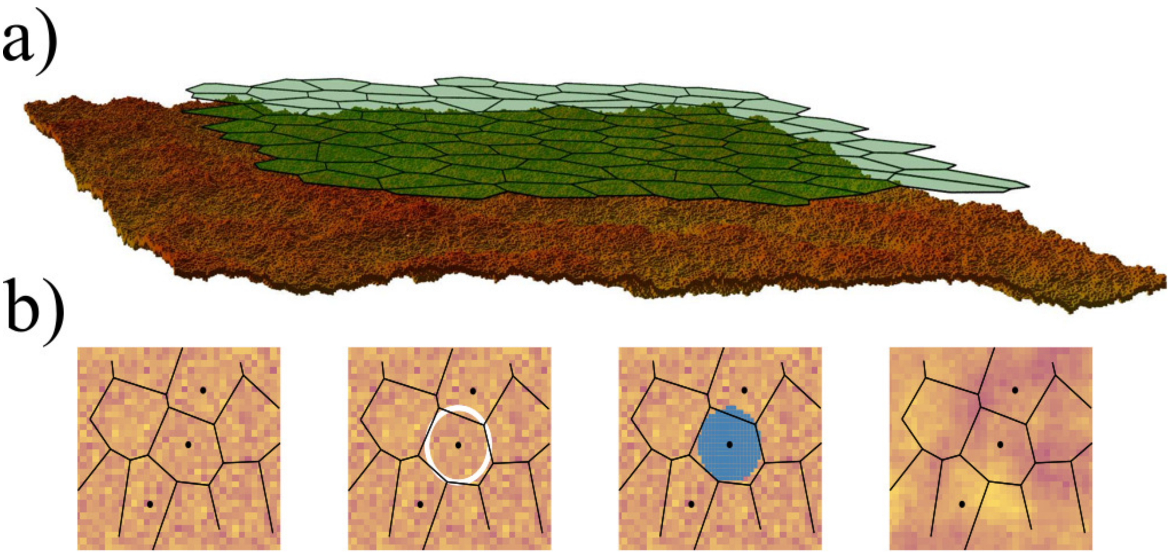

Figure 4.1: a) Model illustration. We consider the 2D projection of the tissue (top, in green), described using the Self-Propelled Voronoi model, on a 2D heterogeneous substrate (bottom) where the value of the target shape index of the cells depends on the position. The color of the substrate is related to the value of the shape index in the square tiles, $p_{0,j}$, with red corresponding to higher values and yellow to lower ones. The height profile in the substrate is only meant to illustrate this heterogeneity. b) Schematic representation of the averaging process used on the random substrate. The averaging is performed by sweeping through each square tile and calculating the average of all points at a distance less than $\xi/2$. The white circle corresponds to the averaging radius of a given square tile close to a cell center. The blue shape corresponds to the square tiles used for the averaging. Here we have used approximately 80 blue square tiles, where each tile has a length two orders of magnitude smaller than the typical length of a cell. The color of the substrate on the last panel represents the averaged substrate.

of equations of motion in the overdamped regime,

$$\frac{\mathrm{d}\mathbf{r}_i}{\mathrm{d}t} = \mu \mathbf{F}_i + v_0 \hat{\mathbf{n}}_i, \tag{4.1}$$

where $\mathbf{F}_i$ is the net force acting on cell i, μ is the mobility of the cell, v_0 the self-propulsion speed, and $\hat{\mathbf{n}}_i = (\cos\theta_i, \sin\theta_i)$ is a polarity vector which sets the direction of self-propulsion. For simplicity, we consider that θ_i is modeled by a stochastic process given by,

$$\dot{\theta}_i = \eta_i(t), \ \langle \eta_i(t)\eta_j(t')\rangle = 2D_r\delta(t-t')\delta_{ij}, \tag{4.2}$$

where $\eta_i(t)$ is an uncorrelated random process of zero mean and variance set by a rotational diffusion coefficient D_r.

The force $\mathbf{F}_i$ describes the many-body cell-cell interaction and is given by $\mathbf{F}_i = -\nabla_i E$, where $E = \sum E_i$ and E_i is the energy functional for cell i. We choose the unit of length to be given by the square root of the average area of all the cells. We can then write a dimensionless version of the contribution of each cell to the energy functional as [45,46],

$$e_i = k_A(a_i - 1)^2 + (p_i - p_{0,i})^2 \ , \tag{4.3}$$

where a_i and p_i are the dimensionless area and perimeter of cell i, $p_{0,i}$ is the target perimeter of cell i, and k_A represents the ratio between the relative stiffness of the area and perimeter elasticity of the cell.

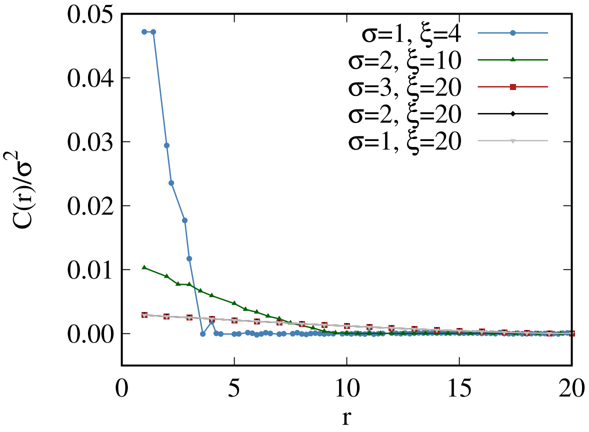

Figure 4.2: Correlation function versus distance for a substrate with averaging radius $\xi = 2, 5, 10$, mean $\overline{p}_0 = 0$ and standard deviation $\sigma = 1, 2, 3$. We re-scale the correlation by the standard deviation in order to collapse the different curves with the same ξ.

4.2.1 Substrate properties

We consider a square substrate of length $L = \sqrt{N}$, where the value of the target shape index ($p_{0,i}$) is spatially dependent. The substrate is divided into square tiles with lattice constant δ, in units of the cell diameter. Each square tile has a value of the target parameter randomly drawn from a Gaussian distribution with mean $\overline{p}_0$ and standard deviation σ. Throughout the dynamics, the value of the shape index, $p_{0,i}$, for each cell corresponds to the one in the underlying square tile. When a cell moves from one square tile to another, its target shape index (in Eq. (4.3)) changes accordingly. We expect that cells take a characteristic time to adapt to changes in the underlying substrate [130, 183]. We first consider this adaptation time to be negligible and in the following chapter, we discuss its effect when it is comparable to the other relevant time scales.

Since cells spread over an area larger than that of a square tile, we average the shape index over a distance on the random substrate to mimic, in a simplified way, the cells ability to probe its surroundings (see Fig. 4.1 b)). The averaged substrate has the same size as the random substrate and thus the same lattice constant δ. The shape index on each square tile j, of the averaged substrate, is calculated by taking the average of the shape indices of the square tiles in the original substrate which have their centers at a distance smaller than $\xi/2$ from the centers of j. Thus, for a given ξ the averaged substrate has mean $\overline{p}_0$ and standard deviation $\sigma/\sqrt{n}$, where n is the number of square tiles inside the corresponding averaging circle.

As ξ increases, the correlations in the substrate also increase. In Fig. 4.2 we show how the correlations in the averaged substrate change for different correlation lengths and standard deviations of the initial substrate. We find that for $r > \xi$, the correlations are zero. This is due to the fact that two substrate sites at a distance larger than ξ no longer share sites in their averaging areas. By re-scaling the correlations by σ^2 we are able to collapse the different curves for the same ξ. We also note the approximately linear decrease of the correlations with distance.

To shed light on these results, we calculate explicitly the averaging effects in a 1D substrate. In this case, each site i on the averaged substrate is an average of the j sites which are at a distance $r \leq \xi/2$, in the initial substrate. The initial substrate is generated by randomly assigning a number drawn from a normal distribution with mean $\overline{p}_0$ and standard deviation σ, to each site, X_i^{in}, where i is the site and in represents the initial substrate. The second substrate is an average of the initial one, thus the value on site i will be,

$$\begin{aligned} X_i^{av} =& (X_{i-\xi/2}^{in} + X_{i-\xi/2+1}^{in} + X_{i-\xi/2+2}^{in} + \dots \\ &+ X_{i+\xi/2-2}^{in} + X_{i+\xi/2-1}^{in} + X_{i+\xi/2}^{in})/(\xi+1). \end{aligned} \tag{4.4}$$

The correlation between two sites at a distance r on the averaged substrate is given by,

$$C(r) = \langle X_i^{av} X_{i+r}^{av} \rangle - \langle X_i^{av} \rangle \langle X_{i+r}^{av} \rangle. \tag{4.5}$$

By substituting Eq. (4.4) into Eq. (4.5), the only terms that remain after expanding the multiplication are the quadratic terms that overlap in both intervals. For example, when $i = 1$, $r = 2$ and $\xi = 2$, one finds,

$$\begin{aligned} C(r) =& \langle X_1^{av} X_3^{av} \rangle - \langle X_1^{av} \rangle \langle X_3^{av} \rangle \\ =& \langle X_2^{in} X_2^{in} \rangle - \langle X_2^{in} \rangle \langle X_2^{in} \rangle = \sigma^2. \end{aligned} \tag{4.6}$$

Generalizing for any ξ and r,

$$C(r) = \frac{(\xi + 1 - r)\sigma^2}{(\xi + 1)^2}, \tag{4.7}$$

where $(\xi + 1 - r)/(\xi + 1)^2$ corresponds to the number of sites on the line shared by sites i and $i + r$ for any ξ.

In the 2D case we consider a circle of diameter ξ centered on site i, thus $C(r) = A(r, \xi)\sigma^2$, where $A(r, \xi)$ depends on the geometry of the grid and quantifies how many points overlap and contribute to the correlations. In the model used, this term is not easily calculated. Nonetheless, the 1D case gives us insight on the behavior of the correlation function shown in Fig. 4.2. We recover the σ^2 scaling and it highlights its linear dependence with distance. These results are valid for $r \leq \xi$, since for $r > \xi$ the sites are uncorrelated.

4.3 Results and discussion

To simulate the confluent tissue, we used a hybrid CPU/GPU software package, cellGPU [99], for the self-propelled Voronoi model. The equations of motion, Eq. (4.1), are integrated using the Euler method, with a time step of $\Delta t = 10^{-2}$. We impose periodic boundary conditions, $D_r = 1$, $v_0 = 0.1$, and $k_A = 1$. For the initial configuration, we generate N positions at random and let the system relax over 10^4 time steps. The random substrate consists of square tiles with lattice constant $\delta = 0.03125$, in units of the cell diameter. This small value guarantees that there are no spatial correlations at the scale of the cell size and that cells are able to explore more than one substrate square tile even when they have very low motility. After the initial relaxation, the simulation is performed for another 10^6 additional time steps.

4.3.1 Overview

To characterize the fluidity of the tissue, we measure the mean squared displacement from the initial position, averaging over all the cells ($\langle \Delta r^2(t) \rangle$) and we estimate the diffusion coefficient using:

$$D = \frac{\langle \Delta r^2(t) \rangle}{4t}, t \gg 1. \tag{4.8}$$

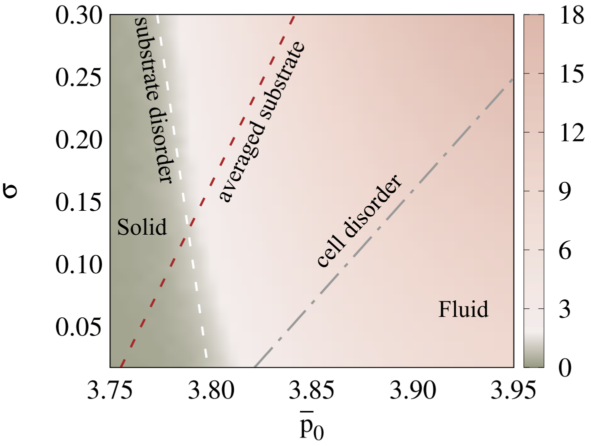

Figure 4.3: Phase diagram of the tissue for substrate or cell disorder. On the vertical axis is the standard deviation of the Gaussian distribution, σ, and on the horizontal axis the mean, $\overline{p}_0$. The color gradient represents the diffusion coefficient of the tissue when using the random substrate disorder (given by Eq. (4.8)), in units of $D^* \approx 9.04 \times 10^{-5}$, which corresponds to the value of the diffusion coefficient at the onset of rigidity in the homogeneous system, i. e. , $p_0 = 3.8$. The white (dashed) line defines the threshold where the fraction of rigid cells (cells with $p_i < 3.8$), forms a percolating cluster, $\sigma(\overline{p}_0) = -11.2\overline{p}_0 + 42.7$. Thus, it sets the onset of rigidity, in the presence of a disordered substrate. Results were obtained for $N = 1024$ and averaged over 10 samples. The gray (dot-dashed) line is obtained from Ref. [8] for a tissue with heterogeneity in the mechanical properties of individual cells described by a cell-dependent shape index $p_{0,i}$, which is also drawn from a normal distribution with the same mean and standard deviation. In this case, the onset of rigidity is given by $\sigma(\overline{p}_0) = 1.2\overline{p}_0 - 4.7$. The brown (dashed) line gives the onset of rigidity when an averaged substrate is used with correlation length of the order of the cell diameter. Here, the line is given by $\sigma(\overline{p}_0) = 3.3\overline{p}_0 - 12.5$. This figure highlights the different effects of disorder. When the disorder is at the cell level the tissue becomes more rigid, while when it is spatially dependent (i.e., on the substrate) the tissue becomes less rigid when the substrate correlation length is less than the diameter of the cells, but more rigid when it is larger. The different phases are shown in the figure, where the tissue is marked solid or fluid. The lines do not meet at $\sigma = 0$ since in Ref. [8] the Vertex model was used rather than the Voronoi model used in this work.

This quantity is obtained numerically by running the simulations for 10^6 time steps and calculating the slope of a linear fit, using the least squares method, of the mean squared displacement averaged over all the cells for all time steps above 10^5. In the solid-like phase the cells are caged by their neighbors and few cell rearrangements occur. Thus, the mean squared displacement is characterized by an initial ballistic behavior ($\langle \Delta r^2 \rangle \sim t^2$) but rapidly saturates. On the other hand, in the fluid-like phase, the cells are able to break free from their cages and the tissue flows. Thus, the mean squared displacement is diffusive ($\langle \Delta r^2 \rangle \sim t$) asymptotically [2]. We have found that we can measure the diffusion coefficient reliably for time steps above 10^5, in the fluid-like phase. As the solid-like phase is approached the fitting worsens, as the diffusion coefficient decreases to zero. Nonetheless, we still use the same technique.

A recent work reported the effect of heterogeneities in the mechanical properties of individual cells using the Vertex model [8]. In this study, heterogeneity is introduced at the cell level by endowing each cell with a random shape index, $p_{0,i}$, chosen from a Gaussian distribution with mean $\overline{p}_0$ and standard deviation σ. The shape index of each cell is then constant over time. It was observed that the shear modulus increases with the disorder, σ, corresponding to a more rigid tissue. In what follows we compare the effect of the two types of disorder: substrate disorder, where the shape parameter is spatially dependent, and cell disorder, where the shape parameter is a time independent property of the cell as discussed in Ref. [8]. For cell disorder, we have chosen the probability distribution of the shape index ($p_{0,i}$) to be Gaussian, parameterized by the same mean ($\overline{p}_0$) and standard deviation (σ).

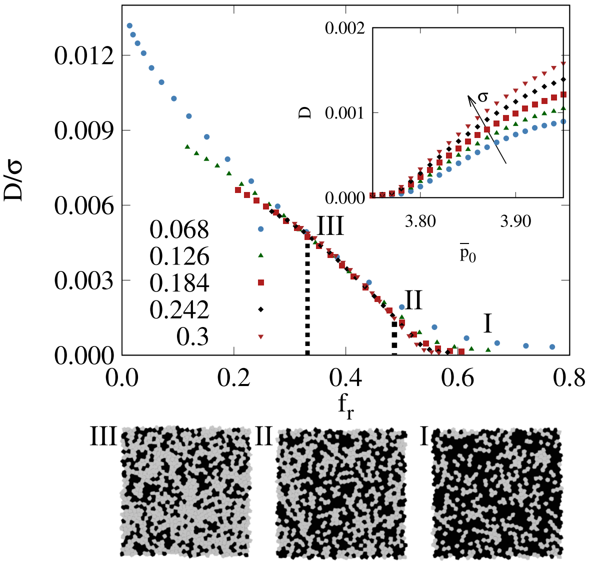

Figure 4.4: Average cell diffusion coefficient as a function of the fraction of rigid cells, f_r. The diffusion coefficient is re-scaled by the standard deviation σ to collapse the curves. These results were obtained for $N = 1024$, $\sigma = 0.068 - 0.3$ in steps of 0.058, $\overline{p}_0 = 3.75 - 3.95$ in steps of 0.01 and averaged over 100 samples. The scaling suggests that the fraction of rigid cells drives the rigidity transition. In the inset are the individual curves to highlight the increase of the diffusion coefficient with the disorder (σ). Below the main plot are snapshots for different fractions of rigid cells (f_r), where rigid cells in black have a shape index below a given threshold ($p_{0,i} < \overline{p}_0^*$) and fluid cells in gray have, $p_{0,i} > \overline{p}_0^*$. We recall that $\overline{p}_0^* = 3.8$ is the threshold for rigid cells.

We note that both types of disorder are quenched as they do not evolve with the dynamics. Nevertheless, the substrate disorder is fixed in space, while that of the cells is carried by their motion in the fluid phase. In the rigid phase, both types of disorder are fixed in space, as cell motion practically ceases.

Figure 4.3 shows a diagram of the two-parameter space explored for a random substrate, where the color represents the average diffusion coefficient of the cells in the tissue using the random substrate disorder. We explored different values of the mean ($\overline{p}_0$) and standard deviation (σ) of the Gaussian distribution and observed that the diffusion coefficient increases for larger values of the disorder (σ), suggesting that the motility of the cells increases for substrates with larger dispersion of the target shape index. We also show in the inset of Fig. 4.4 the increase of the diffusion coefficient with $\overline{p}_0$ and σ. This is in contrast with the cell disorder case where the rigidity of the tissue increases with increasing disorder [8].

We plot three lines that give the onset of rigidity for the different types of disorder: cell disorder and substrate disorder with and without averaging (as described in the previous section). In depth details on how these lines are calculated are given in the following sections. We observe that the onset of rigidity in the tissue is accompanied by a percolation of rigid cells, defined as the cells with a perimeter smaller than a given shape index threshold, $p_i < \overline{p}_0^*$. When the substrate disorder is not averaged, the line is given by $\sigma(\overline{p}_0) = -11.2\overline{p}_0 + 42.7$, highlighting the increase in motility when the disorder (σ) increases. The cell disorder line is taken from Ref. [8], $\sigma(\overline{p}_0) = 1.2\overline{p}_0 - 4.7$, and highlights the opposite behavior. Lastly, when the substrate with averaged disorder has a correlation length of the order of the cell diameter, $\xi = 2$, the rigidity threshold is given by $\sigma(\overline{p}_0) = 3.3\overline{p}_0 - 12.5$, which also exhibits an increase of tissue rigidity with disorder (σ). Thus, while for small correlation lengths the substrate disorder promotes cell motility, for correlation lengths of the order of the cell diameter, it gives rise to tissues with increased rigidity. Furthermore, the results for the averaged

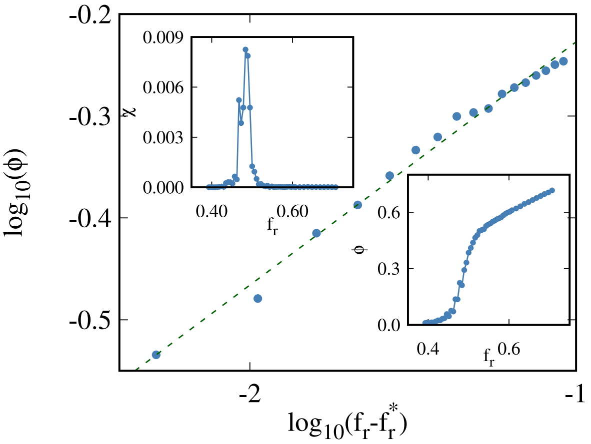

Figure 4.5: Percolation of rigid cells. In the main plot is the fraction of rigid cells in the largest cluster, ϕ, as a function of $(f_r - f_r^*)$, where $f_r^* \approx 0.484$, was calculated from the peak in the variance (top left inset). In the bottom right inset is ϕ as a function of the fraction of rigid cells, f_r. From the slope of the curve in the main plot we estimate the exponent $\beta \approx 0.239 \pm 0.006$. The results were obtained for $N = 16384$ and averaged over 10 samples.

substrate approach those of cell disorder as the correlation length increases, as seen in the slopes of the two lines, suggesting a close relation between these types of disorder. We also note that the lines do not meet at $\sigma = 0$ most likely because in Ref. [8] a different model, i.e., the Vertex model was used.

4.3.2 Random substrate

First, we focus on a random substrate with a lattice constant smaller than the cell size ($\delta = 0.03125$). To calculate the lines separating the different regimes, we use a scaling *Ansatz* to collapse the numerical data and estimate the transition between the solid and fluid-like regions. In Ref. [8] a scaling *Ansatz* is proposed for the shear modulus, which depends on the ratio between σ and the distance to a threshold $|\overline{p}_0 - \overline{p}_0^*|$, where $\overline{p}_0^*$ is the threshold value. The data was indeed observed to collapse. At $\overline{p}_0 = \overline{p}_0^*$, 50% of the cells are rigid with $p_{0,i} < \overline{p}_0^*$. This fraction decreases or increases above or below $\overline{p}_0^*$. This suggests that the fraction of rigid cells (cells with $p_{0,i} < \overline{p}_0^*$) plays an important role in driving the rigidity of the tissue. The fraction of rigid cells is defined as,

$$f_r = \int_{-\infty}^{\overline{p}_0^*} \mathcal{F}_{\overline{p}_0,\sigma}(p_0)dp_0 = \frac{1}{2}\text{erfc}[(\overline{p}_0 - \overline{p}_0^*)/\sqrt{2}\sigma], \tag{4.9}$$

where σ and $\overline{p}_0$ are the standard deviation and mean of the Gaussian distribution $\mathcal{F}$, respectively. For substrate disorder, the cells shape index changes frequently. Thus, the probability density function should also depend on the spatial distribution of the cells and we have no control over $\mathcal{F}$ in Eq. (4.9). Nonetheless, for the parameters explored, we found that the cells have a distribution of the shape index, $p_{0,i}$, similar to the Gaussian used to generate the substrate disorder, with the same mean ($\overline{p}_0$) and standard deviation (σ). Thus, we use Eq. (4.9) to estimate the threshold of the transition, with $\overline{p}_0$ and σ the same as those used for the substrate.

Figure 4.4 illustrates the data collapse for the diffusion coefficient re-scaled by the standard deviation as a function of the fraction of rigid cells, f_r. To collapse the different curves we used $\overline{p}_0^* = 3.80 \pm 0.01$ in Eq. (4.9). We estimate this value numerically by using different threshold values ($\overline{p}_0^*$) and choosing the one for which we obtained the best data collapse. Figure 4.4 (bottom panels) illustrates the evolution of the rigid cluster, which corresponds to the largest cluster of rigid cells

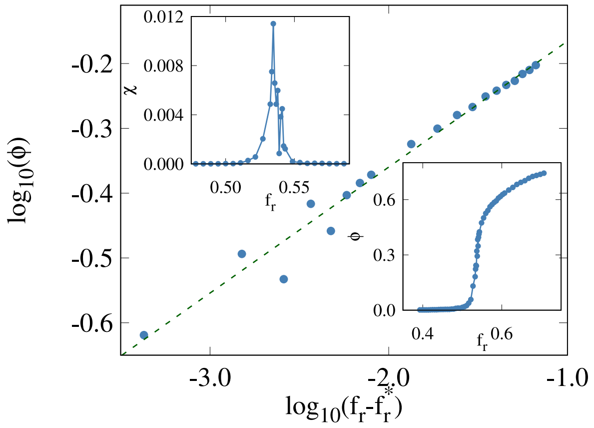

Figure 4.6: Percolation at the rigidity transition. In the main plot is the fraction of rigid cells in the largest cluster, ϕ, as a function of $(f_r - f_r^*)$, where $f_r^* \approx 0.5353$, was calculated from the peak in the variance (top left inset). In the bottom right inset is ϕ as a function of the fraction of rigid cells, f_r. From the slope of the curve in the main plot we estimate the exponent $\beta \approx 0.194 \pm 0.007$, which is consistent with that for 2D random percolation, $\beta = 5/36$. The results were obtained for $N = 16384$ and averaged over 10 samples.

$(p_{0,i} < \overline{p}_0^*)$ in black. We found that this cluster decreases as the standard deviation (σ) or the mean ($\overline{p}_0$) increase. The scaling *Ansatz* suggests that the rigidity is driven by cells with a shape index, $p_{0,i}$, smaller than a threshold $\overline{p}_0^*$. As a result, we can estimate the onset of rigidity by measuring the threshold where the rigid cells form a system spanning cluster.

To analyze the percolation of rigid cells, we measure the fraction ϕ of all rigid cells $(p_{0,i} < \overline{p}_0^*)$ in the largest cluster. To estimate the percolation threshold, f_r^*, we consider the value at which the variance $\chi = \langle \phi^2 \rangle - \langle \phi \rangle^2$ is maximal. In Fig. 4.5 it is shown that χ has a peak around $f_r^* \approx 0.484$ signaling the onset of percolation. When comparing to the data collapse in Fig. 4.4, this threshold is not consistent with the point at which the diffusion coefficient starts increasing from small values $(D > 10^{-4})$. From the numerical results, the distribution of perimeters of the cells, p_i, also follows a Gaussian distribution with mean $\overline{p}_0$ and standard deviation σ. Thus, we now consider a different criteria for rigid cells. We redefine a rigid cell as one with a perimeter (p_i) below the shape index threshold, $p_i < \overline{p}_0^*$. We considered the same threshold, $\overline{p}_0^*$, since the distribution of perimeters (p_i) and shape index ($p_{0,i}$) are similar. Thus, Eq. (4.9) is equivalent when using the distribution for either p_i or $p_{0,i}$. We hypothesize that since p_i is related to the tension in the cells ($\tau \sim p_i - p_{0,i}$) it may be responsible for the increased or decreased rigidity of the tissue, as detailed in previous works [2, 8]. We observe from the inset of Fig. 4.6 that the corresponding χ has a peak around $f_r^* \approx 0.534$ signaling the onset of percolation, in line with the results from the data collapse in Fig. 4.4. From a finite size scaling analysis, using the shift of the peak in the variance (χ) with N, we estimate the threshold $f_r^* \approx 0.5353 \pm 0.0003$. Using this value, we calculate the scaling exponent (shown in the main plot), $\beta \approx 0.194 \pm 0.007$. Larger simulations are needed to estimate the exponents with higher precision, which is beyond the scope of this work. Nonetheless, the obtained value of β, is consistent with that for random percolation, $\beta = 5/36$ [184, 185].

In Fig. 4.3 we plot in white the line corresponding to $f_r^* \approx 0.5353$ which sets the percolation threshold for the disordered substrate. The gray line corresponds to $f_r^* \approx 0.21$ taken from Ref. [8] as the onset of rigidity in the cell disordered system. This highlights the differences between the two types of disorder and how they change the mechanical properties of the tissue. In the cell disordered case, the heterogeneity increases the tensions, $\tau \sim p_i - p_{0,i}$, leading to a more rigid tissue. For the substrate disorder, larger tensions can be observed at higher values of the disorder (σ) but the average

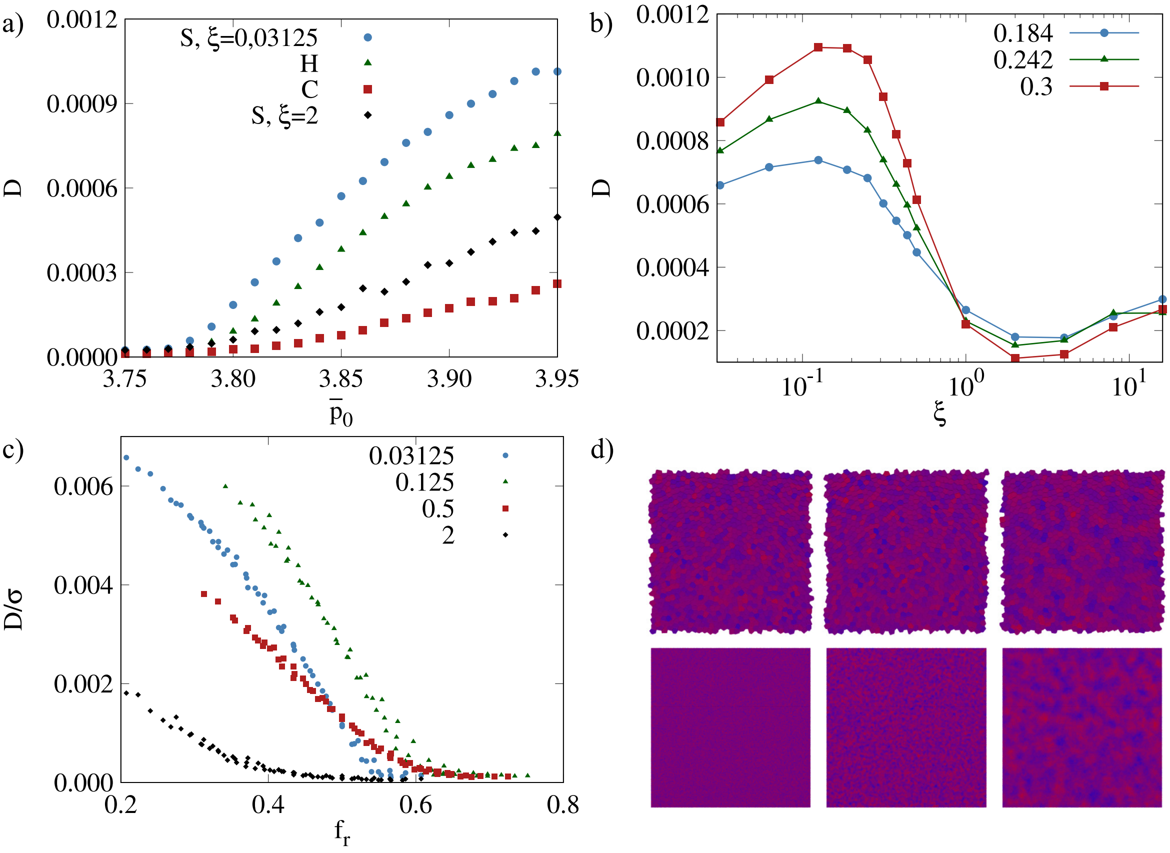

Figure 4.7: Effect of substrate heterogeneities on cell motility. In a) the diffusion coefficients are plotted for different types of heterogeneity: "S" is for substrate disorder, not averaged for a correlation length $\xi = 0.03125$ and averaged for $\xi = 2$. "C" is for cell disorder, as in Ref. [8], where each cell has a random shape index $p_{0,i}$ from a normal distribution, which remains constant. "H" is for the homogeneous tissue. Panel b) illustrates how the diffusion coefficient varies with the substrate correlation length ξ, for a mean $\overline{p}_0 = 3.85$ and $\sigma = 0.184, 0.242, 0.3$. In c) the diffusion coefficient re-scaled by the standard deviation (σ) is plotted as a function of the fraction of rigid cells, f_r, for four different correlation lengths, ξ. In d) are schematic representations of the tissue (top) and the substrate (bottom) for correlation lengths $\xi = 0.125, 0.5, 2$ respectively. These results were obtained using $N = 1024$ and averaged over 10 different samples. We found that although the mechanical properties of the tissue change with the correlation length, ξ, the curves collapse with the fraction of rigid cells, f_r, suggesting that the percolation of rigid cells still drives the tissue rigidity. A correlation length of $\xi = 1$, is found above which the response of the tissue to the substrate disorder changes, with higher disorder, σ, leading to a more rigid tissue.

tension in the tissue decreases. Furthermore the distribution of tensions becomes more symmetrical, which promotes the fluid-like state (see following sections).

4.3.3 Averaged substrate

In a cell tissue, one expects that one cell senses a region of the substrate rather than a single point. In order to account for this effect, we consider next the averaged substrate described in the methods section. The averaging is aimed to mimic the process through which a cell senses a given area under it and thus responds. To each square tile j in the averaged substrate corresponds a value of the shape index, $p_{0,j}$, which is the average of the shape index in the square tiles within a distance $\xi/2$ from j. The length scale ξ sets the diameter of the circle used to calculate the averaged substrate disorder and thus sets the substrate correlation length. Figure 4.7 d) shows some examples of averaged substrates (bottom row) with the corresponding tissues (top row).

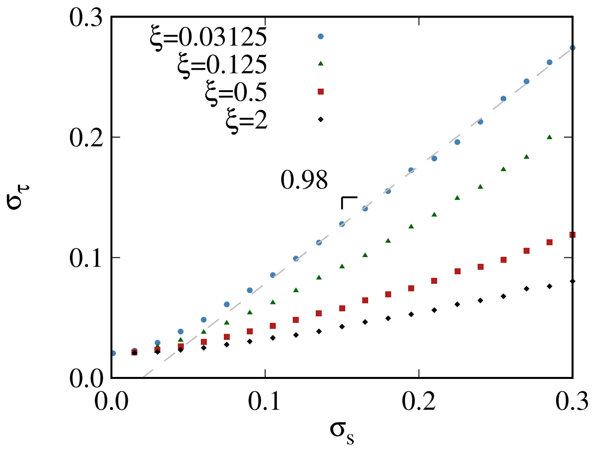

Figure 4.8: Dispersion of the tensions as a function of the dispersion in the substrate, for averaged substrates with $\xi = 0.03125, 0.125, 0.5, 2$. These results were taken for $N = 1024$ and were averaged over 10 samples.

Figure 4.7 a) depicts the diffusion coefficients measured for four different systems as a function of the mean, $\overline{p}_0$. We consider a random substrate (S, $\xi = 0.03125$), a homogeneous tissue (H), a tissue with cell disorder (C) and an averaged substrate (S, $\xi = 2$). Both substrate and cell disordered systems have a disorder dispersion $\sigma = 0.184$. We confirm that, the cell disorder decreases the motility of the cells while the random substrate increases it. However, if the correlation length of the substrate is of the order of the typical cell diameter (or larger) then the cells become less mobile than in the homogeneous case. Thus, substrate disorder with large correlation lengths can also lead to more rigid tissues. In Fig. 4.7 b) this is shown for three different values of the standard deviation (σ). We find that while for correlation lengths lower than the typical cell diameter, $\xi < 1$, more disordered substrates lead to larger diffusion coefficients than in the homogeneous case, for correlation lengths above the typical cell diameter, $\xi > 1$, substrate disorder decreases cell diffusion. This happens since for large correlation lengths the cells adapt to the substrate smoothly as the gradient of the shape index, $p_{0,i}$, is small. By contrast, for smaller correlation lengths, ξ, the cells change their shape index $p_{0,i}$ quite rapidly (the dependence of the diffusion coefficient with ξ is further explored in the following sections). This leads to different behaviors of the tension distribution in the tissue. For $\xi < 1$, as the dispersion, σ, increases, the variance of the tensions also increases while its average value decreases promoting fluid-like tissues. For $\xi > 1$ the variance of the tensions is almost constant while their average value increases leading to more rigid tissues.

Both types of behavior, however, are related to the percolation argument developed above. In Fig. 4.7 c) we report data for different values of the correlation length (ξ) which is collapsed using the same scaling as in Fig. 4.4. Thus, the behavior is driven by the percolation of rigid cells. As the correlation length (ξ) changes, the threshold values for the percolation transition also change ($\overline{p}_0^*(\xi)$ and $f_r^*(\xi)$). We note that for $\xi = 2$, where the tissue is the most rigid, the percolation threshold for the fraction of rigid cells, $f_r^* \approx 0.38$, tends to the value reported in Ref. [8], which is consistent with a more rigid tissue than for the homogeneous substrate.

4.3.4 Tension distribution

The main driving force for the decreased rigidity of the tissue is the dispersion of the perimeters of each cell, p_i. As such, the higher this dispersion, the more the tissue becomes fluid like. After a certain point the p_i, of each cell does not have time to decrease to the preferred value, $p_{0,i}$. Figure 4.8

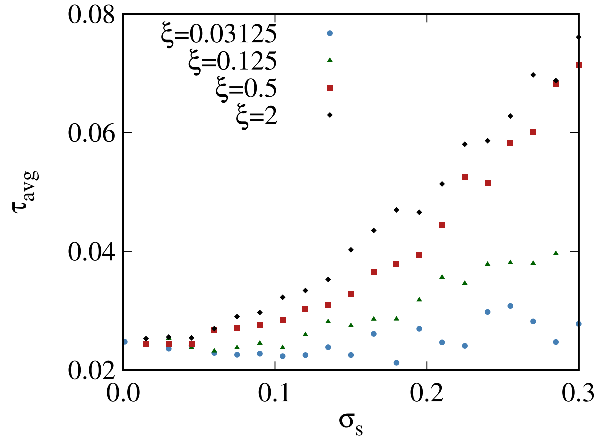

Figure 4.9: Average tension as a function of the dispersion in the substrate, for averaged substrates with $\xi = 0.03125, 0.125, 0.5, 2$. These results were taken for $N = 1024$ and were averaged over 10 samples.

shows how the dispersion of the tensions (calculated with $\tau = p_i - p_{0,i}$) in the cells, σ_τ, increases with the dispersion of the substrate, σ_s, for $\xi = 0.03125$. We find that for $\sigma_s > 0.1$, the dispersion of the tensions grows linearly with that of the substrate. This means that cells do not have enough time to adapt before moving to different square tiles. This in turn leads to a more fluid-like tissue as cells are being perturbed frequently. As ξ increases, the correlations of the substrate will span longer distances and thus the cells will have more time to relax. This leads to a more rigid tissue, which is also observed in the average tensions (Fig. 4.9), which increase with ξ, characteristic of rigid tissues.

4.3.5 Different size of square tiles

Instead of averaging through multiple square tiles in the substrate, one can also introduce correlations in the tissue by increasing the lattice constant, δ. The comparison between the two is reported in Fig. 4.10. We find that the results are similar. The differences may arise from the fact that, in this case, the substrate has larger discontinuities between square tiles while for the averaged substrate the gradient in $p_{0,i}$ is smaller. This result also suggests that the percolation transition observed in the tissue is not an artifact of the substrate, itself.

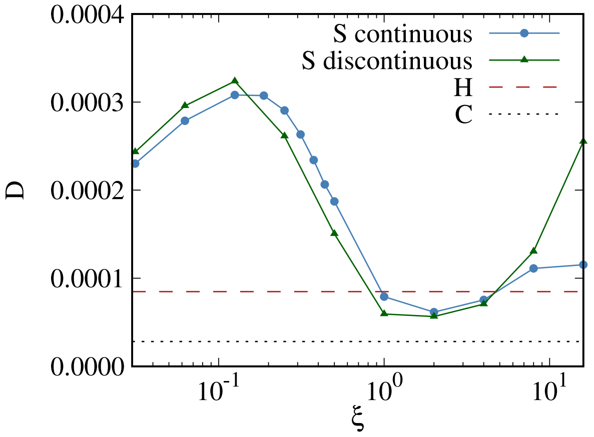

Figure 4.10: Diffusion coefficient as a function of ξ. Two curves are shown, the first corresponds to the data in Fig. 4.7, while the second corresponds to a non-averaged substrate with a larger lattice constant, δ. The Gaussian distributions have $\overline{p}_0 = 3.81$ and $\sigma = 0.184$. The two horizontal lines correspond to the cell disorder and homogeneous cases.

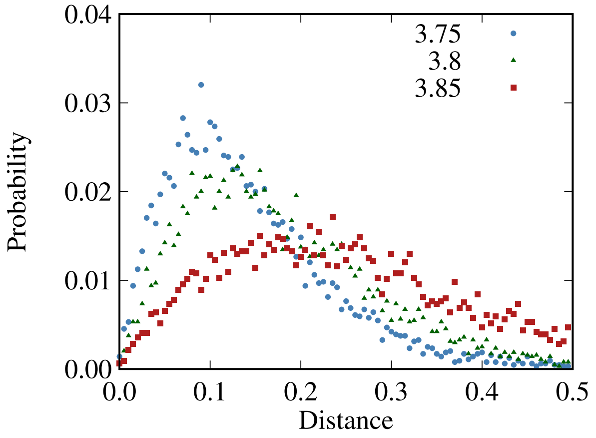

Figure 4.11: Histogram of the distance moved by the cells between the perturbation and the new minimized state. Results were taken for $N = 64$, $\overline{p}_0 = 3.75, 3.8, 3.85$, $\sigma = 0.184$ and averaged over 100 samples.

4.3.6 Perturbations in the athermal model

To shed light on the maximum of the diffusion coefficient as a function of ξ (seen in Fig 4.7 b)) we introduce the following athermal perturbation: we consider the tissue without activity ($v_0 = 0$) and relax it with the same $p_{0,i}$ for all cells. We consider that the tissue is fully relaxed when the maximum force on any cell is smaller than 10^{-12}. Then we perturb the minimized configuration by changing the $p_{0,i}$ of each cell to another randomly distributed $p_{0,i}$ generated from a Gaussian distribution with mean $\overline{p}_0$ and standard deviation σ. After the perturbation we let the tissue relax again.

Figure 4.11 shows the results for three different $\overline{p}_0$ and $\sigma = 0.184$. On average, cells move a length of approximately 0.1 to 0.2 after the perturbation. This is consistent with the maximum value found in Fig. 4.7 b).

4.4 Conclusion

We studied the effects of spatial disorder of the cell-substrate interaction on the motility of the cells in a confluent tissue. We used the self-propelled Voronoi model, where the preferred geometry of each cell, $p_{0,i}$, depends on its spatial position. To model the spatial heterogeneities we divided the surface of the substrate into square tiles, where each tile has a value of the shape index, $p_{0,j}$, drawn from a Gaussian distribution with mean $\overline{p}_0$ and standard deviation σ. We also considered a more realistic description of an averaged substrate, where cells respond to a local averaged disorder. We introduced a correlation length for such an average and showed that for correlation lengths smaller than the cell diameter, the motility of the cells increases. For correlation lengths larger than the cell diameter, the disorder makes the tissue more rigid, by decreasing the cell motility. This is in contrast to what is known for tissues with disorder in the mechanical properties of the cells. For those tissues, the rigidity increases with the level of disorder [8]. Our results suggest that, for smaller correlation lengths, the random change in the shape index leads to a more symmetrical tension distribution with lower average values, characteristic of more motile cells. For larger correlation lengths, the cells will have more time to adapt and the distribution of tensions shifts towards larger values characteristic of a more rigid tissue. We also note that for the largest values of the correlation length where the tissue is most solid like, our results approach those of the cell disorder reported in Ref. [8]. This suggests that these two types of disorder are closely related.

We also show that our results for a given correlation length may be collapsed onto a single curve if we use the fraction of rigid cells (Eq. (4.9)) as the control parameter. This suggests that the changes to the mechanics of the tissue are a consequence of the percolation of rigid cells, characterized by a perimeter smaller than a given threshold $p_i < \overline{p}_0^*$. Using the fraction of rigid cells in the largest cluster, we obtained the threshold for the reported increase in motility, $f_r^* \approx 0.5353 \pm 0.0003$, for a completely random substrate without averaging, and a scaling exponent $\beta \approx 0.194 \pm 0.007$. For larger values of the correlation length, our results suggest that the value of the threshold changes. Due to the symmetries of the model and the short-range nature of the correlations in the spatial distribution of the disorder, we hypothesize that the percolation transition belongs to the 2D random percolation universality class, as corroborated by the value of the obtained exponents.

Although we focused on changes to the shape of the cells, more specifically the cells perimeter, it is expected that the substrate can affect other properties. Previous works [186] have shown that the dynamics of mixtures is much less sensitive to differences in cell area than perimeter. Thus, we expect that, changes in area will lead to more subtle and potentially less marked effects.

These results can play an important role not only in tissue engineering, where the mechanical properties of the tissue are important [169], but also in the study of cancer where cells change the surrounding ECM in order to enhance their motility. Our results suggest that the underlying structure supporting the tissue, either the ECM or a culture substrate, should not be described using generalized bulk metrics since heterogenieties can play a relevant role in the tissue mechanics. Although we used a simplistic approach, these results should be robust to different substrate geometries. This also extends to curved substrates as long as the curvature does not play a major role in the tissue rigidity, as reported in previous studies [85].

Here, we focused on a 2D description, but a 3D generalization is possible. In a simple generalization of the model to 3D [61], we expect similar results since a fluid to solid transition is present and the cells are able to diffuse throughout the tissue. If we consider a more realistic description of a 3D epithelial monolayer, then we would need a Vertex model along the lines of Ref. [153] and characterize the apical and basal sides of the cells differently. Then, it is expected that the competition between the basal and apical perimeter difference plays a role in the diffusion of the cells. This would be interesting to explore in future studies.

We have also neglected both cell death and division. Due to modeling constraints, it is required that the number of cells remains constant throughout the simulation. Other works explored the effect of cellular division [98], and in the context of disordered media, it would be interesting to focus on how cell division or death play a role in tissue cell motility.

Chapter 5

The cell adaptation time sets a minimum length scale for patterned substrates

The structure and dynamics of tissue cultures depend strongly on the physical and chemical properties of the underlying substrate. Inspired by previous advances in the context of inorganic materials, the use of patterned culture surfaces has been proposed as an effective way to induce space-dependent properties in cell tissues. However, cells move and diffuse and the transduction of external stimuli to biological signals is not instantaneous. Here, we show that the fidelity of patterns to demix tissue cells depends on the relation between the diffusion (τ_D) and adaptation (τ) times. Numerical results for the self-propelled Voronoi model reveal that the fidelity decreases with τ/τ_D, a result that is reproduced by a continuum reaction-diffusion model. Based on recent experimental results for single cells, we derive an adaptation time scale for the cells in the substrate which is in line with those measured in experiments.

5.1 Motivation

The regulated growth and maintenance of a living tissue under controlled conditions is a major challenge for cell biology and tissue engineering. The standard procedure consists in the use of culture surfaces to support and guide the cells [47, 64, 76, 187, 188]. An extensive body of research shows that the cell morphology and dynamics are sensitive to the physical and chemical properties of the substrate [47–54, 64]. For example, it has been shown that substrate stiffness can significantly affect the geometry of cultured cells, including their spreading area [54, 114], volume [115], and shape elongation [116]. By adhering to a given substrates, the cells are influenced by the cell-matrix adhesion complexes which lead to different changes in the properties of cells, e. g., when cells are in contact with rigid substrates, its cytoskeleton develops stresses at the level of the actin network which leads to polarization [131]. In addition, the nanotopography of the substrate can alter cell polarization, shape, and motility [68–71]. Thus, the effort has been made in the design of biocompatible substrates that regulate the individual and collective dynamics of cells.

There is a sustained interest in the possibility of generating spatial patterns of cells with different properties, which is critical for morphogenesis, collective cell motion, and wound healing [65–73]. In development, the processes that typically generate two tissue types separated by a boundary have been studied extensively [189–193], and often occur because two different cell types, through various mechanisms, prefer to be surrounded by cells of the same type [55, 162, 186, 194, 195]. However, in vitro, an alternative approach is to culture a single cell type on a patterned substrate, and allow the patterned substrate to change the properties of cells to generate a pattern [67,68,70,71].

Patterned substrates have been used to a large extent in the context of inorganic materials [126–129]. However, their use for biological systems raises several additional difficulties. Besides the need for biocompatible materials, the transduction of external stimuli into biological signals that control the cell morphology and mechanics is not instantaneous. It requires a hierarchy of biochemical processes, which sets a characteristic adaptation time that can extend over hours [130],for example, cells on rigid substrates reorganize their cytoskeleton through stresses applied to the actin network to conform to the substrates properties [131]. The problem is that, within the adaptation time scale, cells might move around and explore other regions of the substrate. Thus, the fidelity of patterns in the regulation of cell tissues should depend on how the adaptation time compares with the other relevant time scales. This is precisely what we study here.

We consider an epithelial confluent tissue on a simple patterned substrate, consisting of two halves that solely differ in the cell-substrate interaction (see Fig. 5.1). We describe the tissue with the self-propelled Voronoi model, where the cell-substrate interaction is included in the preferential geometry of each cell, as cell shapes change as a function of substrate properties [114], and cell shape in turn governs the rate of cell diffusion in monolayers [76]. We show that the fidelity of the pattern in the regulation of the tissue properties is compromised significantly when the adaptation time competes with the diffusion time of cells.

5.2 Methods

We model the confluent tissue as a monolayer of N cells using the self-propelled Voronoi model [2, 22, 83]. Each cell i is represented by its center $\mathbf{r}_i$ and its shape is given by the Voronoi tessellation of the space. The stochastic trajectories of cells are obtained from a set of Langevin equations of motion,

$$\frac{\mathrm{d}\mathbf{r}_i}{\mathrm{d}t} = \mu \mathbf{F}_i + v_0 \hat{\mathbf{n}}_i, \tag{5.1}$$

where $\mathbf{F}_i$ is the net force acting on cell i, μ is the mobility of the cell, v_0 the self-propulsion speed, and $\hat{\mathbf{n}}_i = (\cos\theta_i, \sin\theta_i)$ is a polarity vector which sets the direction of the self-propulsion force. For

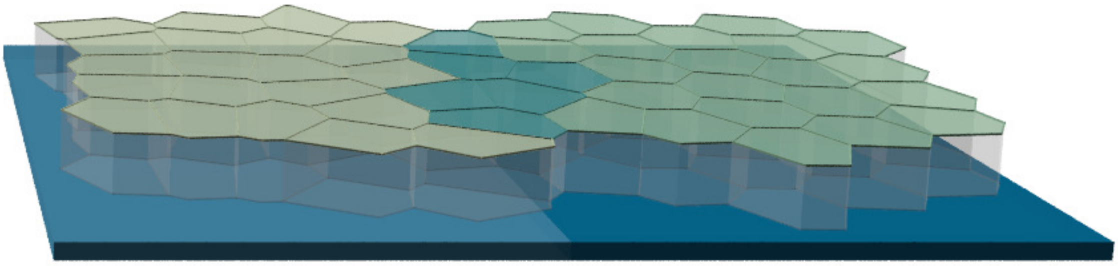

Figure 5.1: Schematic representation of the system. We consider the 2D projection of a confluent tissue on a squared 2D substrate with two regions of equal linear length $L/2$, which differ in the target value of the shape index p_0 of cells: $p_{0,i} = p_A$ on the brighter side (left) of the substrate and $p_{0,i} = p_B$ on the darker one (right), with $p_B > p_A$. The color of the cells is related to their actual shape index $p_{0,i}(t)$, which is equal to p_A for the ones on the left and p_B for the ones on the right. The darker cells (in the middle) have an intermediate value of $p_{0,i}(t)$, i.e., $p_A < p_{0,i}(t) < p_B$.

simplicity, we consider that θ_i is a Brownian process given by,

$$\dot{\theta}_i = \eta_i(t), \ \langle \eta_i(t)\eta_j(t') \rangle = 2D_r\delta(t-t')\delta_{ij}, \tag{5.2}$$

where $\eta_i(t)$ is an uncorrelated random process of zero mean and its variance sets the rotational diffusion D_r.

The net force $\mathbf{F}_i$ describes the multibody cell-cell interaction and it is given by $\mathbf{F}_i = -\nabla_i E$, where $E = \sum E_i$ and E_i is the energy functional for cell i. We choose the unit of length to be given by the square root of the average area of all the cells. We can then write a dimensionless version of the contribution of each cell to the energy functional as [45, 46],

$$e_i = k_A(a_i - 1)^2 + (p_i - p_{0,i})^2 \ , \tag{5.3}$$

where a_i and p_i are the dimensionless area and perimeter of cell i, $p_{0,i}$ is the target perimeter of cell i, and k_A represents the ratio between the relative stiffness of the area and perimeter elasticity of the cell.

We consider a squared substrate of linear length $L = \sqrt{N}$, where the value of the target shape index ($p_{0,i}$) is spatially dependent. As schematized in Fig. 5.1, we split the substrate in half, with different values of $p_{0,i}$ on each side. Thus, cells on the left-hand side have a target $p_{0,i} = p_A$, while the ones on the right-hand side have $p_{0,i} = p_B$, where $p_B > p_A$. When a cell diffuses from one side to the other, their target value of the shape index in Eq. (5.3) changes accordingly, within a characteristic adaptation time τ (Fig. 5.2). Thus, we consider that the time dependence of the shape index $p_{0,i}$ for cell i is given by,

$$\dot{p}_{0,i}(\Delta t_i) = \frac{1}{\tau}[p_{0,i}(\infty) - p_{0,i}(\Delta t_i)], \tag{5.4}$$

where Δt_i is the time interval since the cell crossed the line dividing the substrate, for the last time. $p_{0,i}(0)$ is the shape index of cell i before crossing and $p_{0,i}(\infty)$ is the target value in the new side. By changing this characteristic adaptation time τ, it is possible to control the time it takes for a cell to change from one shape index to the other.

To simulate the confluent tissue, we used a recently developed hybrid CPU/GPU software package, cellGPU [99], for the self-propelled Voronoi model. The equations of motion, Eq. (5.1), are integrated using the Euler method, with a time step of $\Delta t = 10^{-3}$. We impose periodic boundary conditions, $D_r = 1$, $v_0 = 0.3$, and $k_A = 100$, the latter to guarantee that fluctuations in the cell area are negligible when compared to the ones in the perimeter. For the considered set of parameters, the rigidity transition occurs for $p_0 \approx 3.725$ [2]. To generate the initial configuration, we generate N positions at random and let the system relax over 10^4 time steps, with $p_0 = p_B$ for all cells. Then, we set $p_{0,i}(0) = p_A$ for the cells on the left- and $p_{0,i}(0) = p_B$ for the ones on the right-hand side of the substrate.

5.3 Results and discussion

To study the role of the adaptation time τ, we first consider a pair of values for the shape index for which the confluent tissue is in a fluid-like state on both sides of the substrate: $p_A = 3.875$ and $p_B = 3.9$. For these values, the cell diffusion coefficients on each side differ by less than 15%: $D_A = 3.61 \times 10^{-3}$ and $D_B = 4.13 \times 10^{-3}$, obtained from the mean squared displacement. Below, we assume $D_A = D_B = D$.

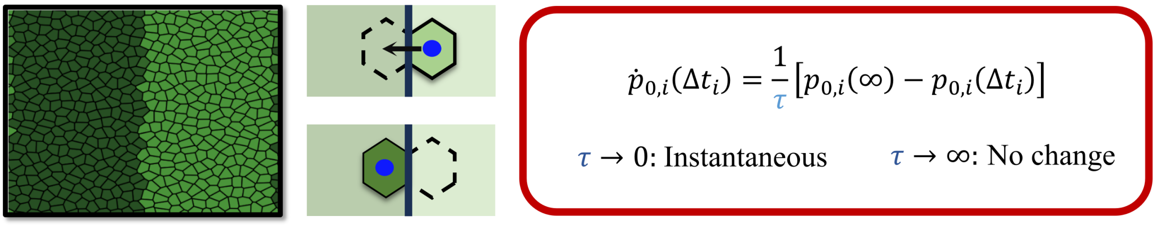

Figure 5.2: Schematic representation of the rules of the substrate. On the left is a snapshot of the tissue at the start of the simulation where the two sides are completely segregated. As cells go from one side of the substrate to the other they will start to adapt and change color. On the right are the equations associated with this adaption, which is modeled as an exponential decay with a characteristic time scale for adaptation τ.

Initially, all cells are fully adapted to the underlying substrate (see *Methods*). As time evolves, cells diffuse and cross from one side to the other. However, due to the finite adaptation time, their target shape index $p_{0,i}$ changes in time, as given by Eq. (5.4), and thus cells of different shape indices mix on both sides of the substrate. To characterize this mixing, we measure the demixing parameter, DMP, defined as,

$$DMP = \frac{1}{N}\sum_{i}^{N}\frac{1}{N_{i,neigh}}\sum_{j}^{N_{i,neigh}} H(\varepsilon - |p_{0,i} - p_{0,j}|), \tag{5.5}$$

where the out sum is over all cells and the inner sum is over the $N_{i,neigh}$ neighbors of cell i [186]. $H(\varepsilon - |p_{0,i} - p_{0,j}|)$ is the Heaviside step function and ε is a threshold that we set to $\varepsilon = 10^{-5}$ (see following sections for the dependence on ε). For $DMP = 1$ the cells in the confluent tissue are completely segregated by their shape index, whereas for $DMP = 0$ they are fully mixed, i.e., each cell is surrounded by cells with a different shape index.

Figure 5.3(a) shows the time dependence of the demixing parameter for different values of the adaptation time τ, where time is rescaled by τ. As cells mix, DMP decreases and saturates asymptotically. Different curves are for different values of τ/τ_D, where $\tau_D = L^2/D$ is the diffusion time which we define as the characteristic time it takes for a cell to diffuse a distance L. In Fig. 5.3(b) is the asymptotic value of DMP as a function of τ/τ_D for different numbers of cells (same density). A data collapse is observed, which shows that finite-size effects are negligible. The monotonic decrease of the asymptotic value of DMP with τ/τ_D hints at a competition between two time scales: the adaptation and the diffusion time. When the adaptation time is negligible ($\tau \ll \tau_D$), cells adapt rapidly to the underlying substrate, with $DMP \approx 1$. When the two time scales compete, the value of DMP should depend on the ratio between the two. In the limit where they are of the same order, DMP should vanish, for the cell changes sides before fully adapting to the new shape index. Thus, large values of the adaptation time compromise the control over the shape of the tissue boundaries via patterned substrates.

The demixing parameter is not uniformly distributed in space. In Fig. 5.3(c) are three snapshots of the tissue obtained at time 10τ, for different values of τ/τ_D. The color of cells depends on the value of the demixing parameter. Cells that are surrounded by cells of the same target shape index p_0 are in green ($DMP = 1$), the ones surrounded by cells of a different p_0 are in red ($DMP = 0$). The ones with intermediate values of DMP are in blue. One clearly sees that the green cells are in the center of each half-space, whereas red cells are concentrated around the boundaries: middle and borders, due to the periodic boundary conditions. However, the width of the regions of green and red cells depends on the value of τ/τ_D.

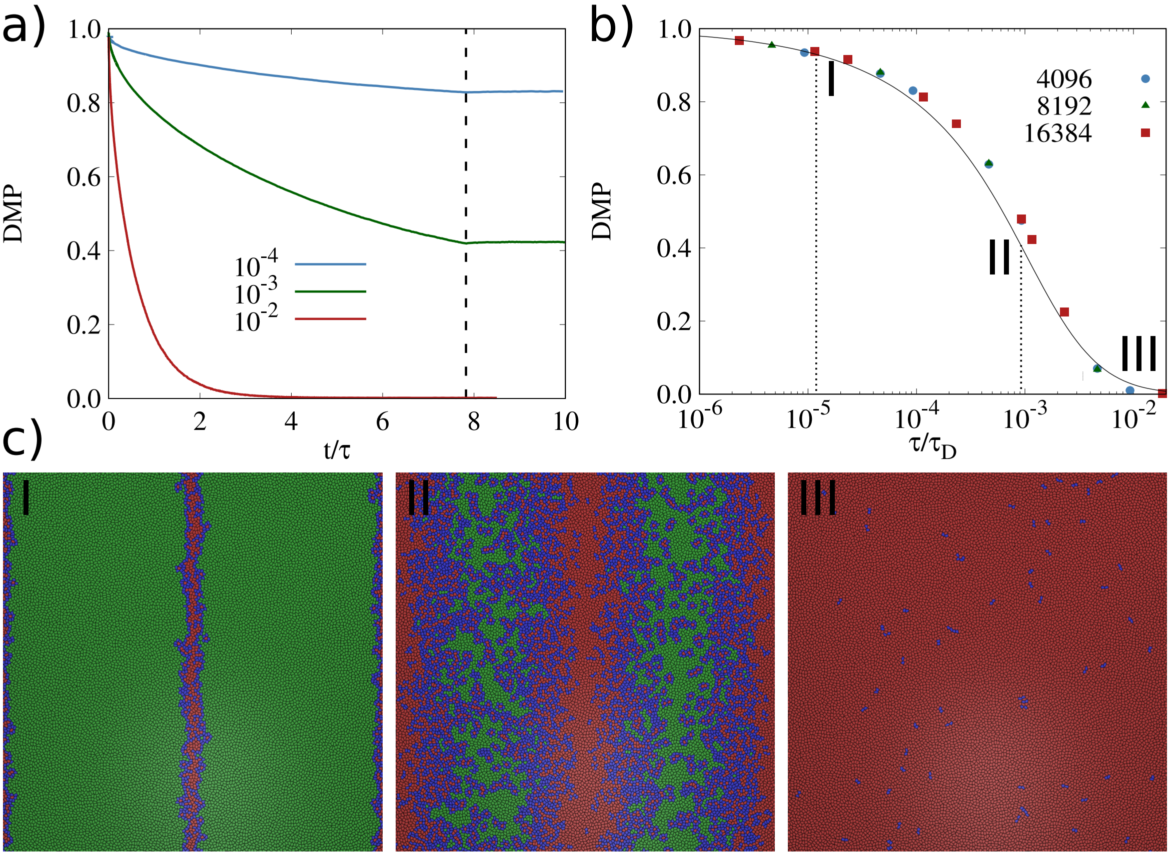

Figure 5.3: Dependence of the demixing parameter DMP on the two relevant time scales: adaptation τ and diffusion τ_D times. (a) Time dependence of the demixing parameter, where time is rescaled by the adaptation time τ. Different curves are for different values of τ/τ_D, namely, 10^{-4}, 10^{-3}, and 10^{-2}. The vertical dashed line corresponds to $\ln[(p_B - p_A)/\varepsilon]$, which is the time it takes for the target shape index of a cell i that crosses to the right-hand side, with $p_{0,i} = p_B$ to become $p_{0,i} = p_A + \varepsilon$, as given by Eq. (5.4).(b) Demixing parameter as a function of τ/τ_D for different system sizes, where the number density of cells is kept constant at 1, i.e., $L = \sqrt{N}$. The (black)-solid line is given by Eq. (5.8), derived from a continuum model, with $\alpha = 0.0866 \pm 0.0009$. (c) Snapshots of the confluent tissue obtained numerically at time 10τ, for three different values of τ/τ_D, namely, 10^{-5}, 10^{-3}, and 10^{-2} (respectively I, II and III). The color of each cell depends on the demixing parameter: green ($DMP = 1$), red ($DMP = 0$), and blue ($0 < DMP < 1$). It is clear that the cluster of red cells is formed around the line dividing the substrate into two parts (see Fig. 5.1) and it grows with τ/τ_D until it spans the entire tissue. Results in (a) and (b) are averages over ten independent samples.

We define $u(x,t)$ as the fraction of cells that are green ($DMP = 1$) at time t, where $x \in [0, L]$ is the spatial coordinate along the horizontal direction. To compute $u(x,t)$ numerically, we divide the system into vertical slices and measure the fraction of cells with $DMP = 1$ within each slice. The results for $u(x, 10\tau)$, for different values of τ/τ_D are shown in Fig. 5.4(a), for $x \in [0, L/2]$. As suggested by Fig. 5.3(c), there are more green cells at $x = L/4$ but, the fraction of cells and the width of the profile decreases with τ/τ_D. The latter scales with $\sqrt{\tau/\tau_D}$ as expected for a diffusive process. To highlight this, we plot the length of the interface, defined by the length l^* at which $u(x, 10\tau)$ is equal to 0.25, 0.5 and 0.75 respectively (see Fig. 5.4(b)).

To describe the competition between cell diffusion and adaptation time, we now propose a continuum model to describe the time evolution of $u(x,t)$. For simplicity, we take advantage of the symmetry of the problem and focus on $x \in [0, L/2]$. We consider a reaction-diffusion equation for $u(x,t)$,

$$u_t(x,t) = D^* u_{xx}(x,t) + T[1 - u(x,t)]. \tag{5.6}$$

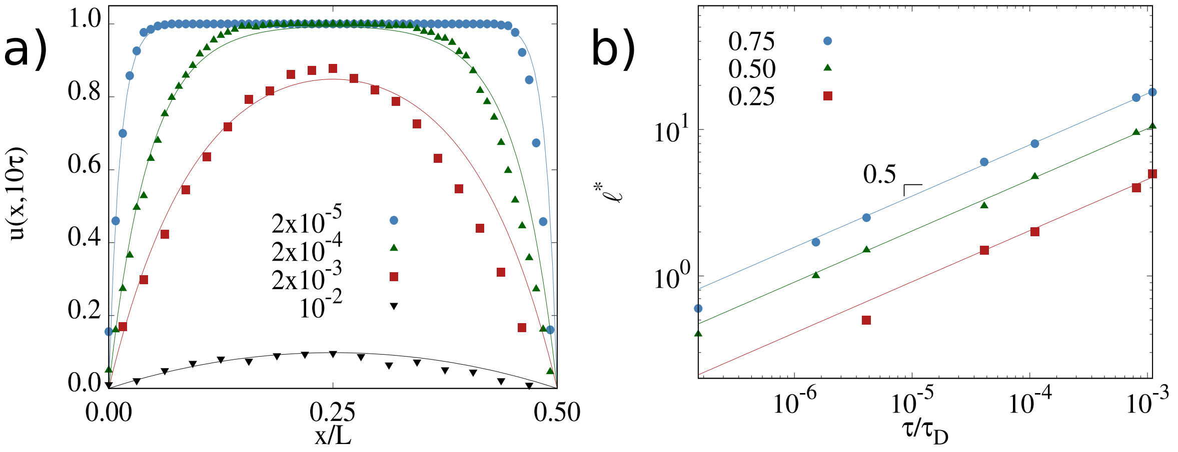

Figure 5.4: Spatial distribution of $N = 16384$ cells with $DMP = 1$. (a) Profile $u(x,t)$ of the fraction of cells with $DMP = 1$, for different values of τ/τ_D, where x is the spatial coordinate along the horizontal direction, $t = 10\tau$, τ is the adaptation time, and τ_D the diffusion time. The lines are given by Eq. (5.7), which is derived from a continuum model, using ϕ as a fitting parameter. (b) Value of $x = \ell^*$ at which $u(\ell^*, 10\tau)$ is 0.25 (squares), 0.50 (triangles) or 0.75 (circles), as a function of τ/τ_D. The slope of the curves is given in the plot as 0.5. Results are averages over ten independent samples.

where u_t is the time derivative and u_{xx} is the second space derivative. The first term on the right-hand side is a diffusive term that describes the collective diffusion of cells, with an effective diffusion coefficient D^*. The second term is a reaction term, which describes the adaptation of cells to the local environment. The adaptation is proportional to the fraction of cells that are not adapted, i.e. $1 - u(x,t)$, and occurs at a rate T that is proportional to the inverse of the adaptation time τ. Since we start from a demixed state, the initial conditions are $u(x,0) = 1$ and the boundary conditions are $u(0,t) = u(L/2,t) = 0$ at all times.

As derived in Appendix A, the control parameter for the dynamics of the continuum model is the ratio $\phi^2 = T(L/2)^2/D^*$. Since $T \sim \tau^{-1}$ and $D^* \sim D$, then $\phi^2 \sim L^2/\tau D = \tau_D/\tau$, which is the ratio between the diffusion and adaptation time scales. We define $\phi^2 = \alpha L^2/\tau D$, where α is a prefactor that depends on the 2D geometry of the substrate and the value of the shape index on both sides. Asymptotically, $u(x,t)$ converges to a stationary state $u_E(\hat{x})$,

$$u_E(\hat{x}) = \frac{1 + e^{\phi} - e^{-\phi(\hat{x}-1)} - e^{\phi\hat{x}}}{1 + e^{\phi}}, \tag{5.7}$$

where $\hat{x} = 2x/L$. As shown in Fig. 5.4(a), this analytical solution (solid lines) is in qualitative and quantitative agreement with the numerical results for the self-propelled Voronoi model, where we set $\alpha = 0.0866 \pm 0.0009$ for all curves, obtained by a fit using the least squares method.

To compute the demixing parameter from the profile in the stationary state, $u_E(x)$, we consider a mean-field approach, where the probability density that two neighboring cells are in the same state is $u_E^2(x)$ and so $DMP = \int_0^1 u_E^2(\hat{x})d\hat{x}$, which gives,

$$DMP = 1 + \frac{1}{1 + \cosh(\phi)} - \frac{3\tanh(\phi/2)}{\phi} \ . \tag{5.8}$$

This solution is the solid line in Fig. 5.3(b), which is in quantitative agreement with the numerical results.

The numerical and analytical results suggest that the fidelity of a patterned substrate in the control of the morphology of a tissue is significantly dependent on the ratio between the diffusion and the

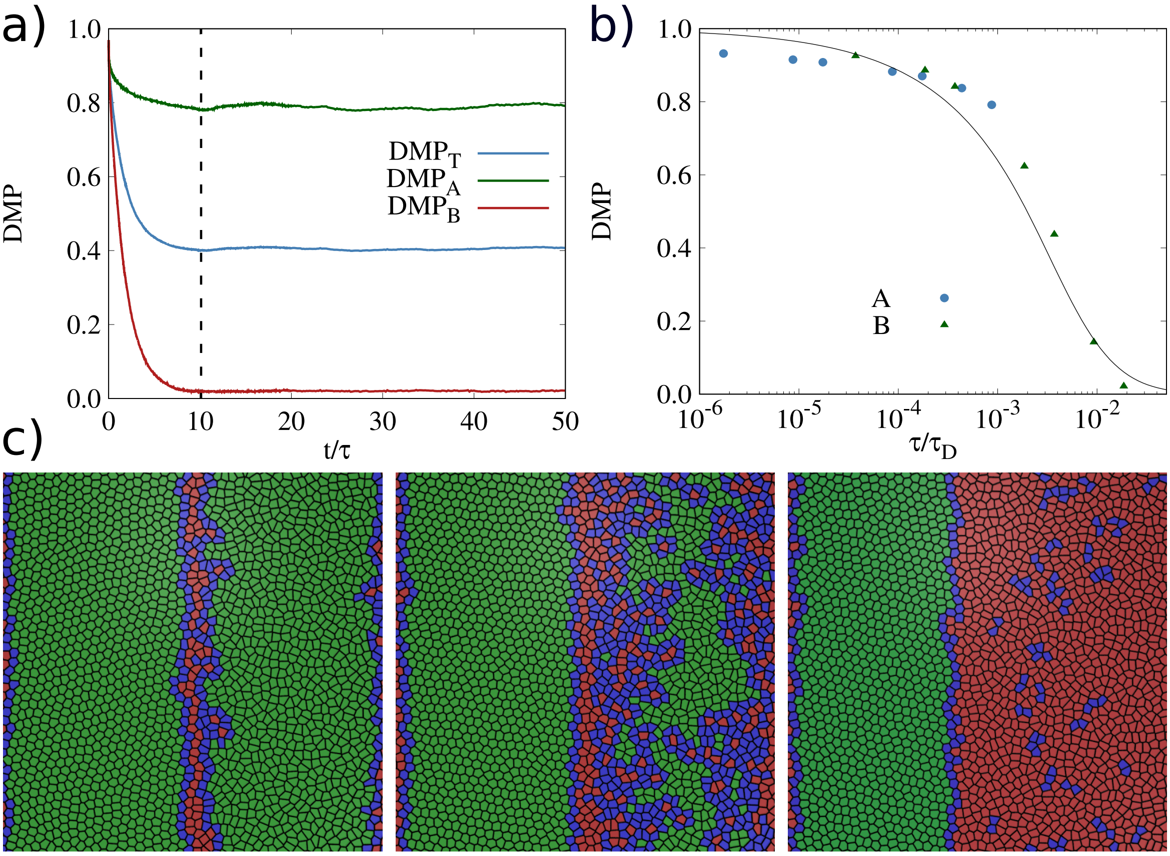

Figure 5.5: Dependence of the demixing parameter for the solid-fluid case. (a) Time dependence of the demixing parameter, where time is rescaled by the adaptation time ($\tau = 5000$), for $N = 2048$. Different curves are for the side A, B, and both sides. (b) Demixing parameter as a function of τ/τ_D for both sides, obtained at 50τ. The (black)-solid line is given by Eq. (5.8), derived from the continuum model, with $\alpha = 0.276 \pm 0.003$. (c) Snapshots of the confluent tissue, obtained numerically for different values of τ/τ_D, namely, 10^{-3}, 10^{-2}, and 10^{-1}. The color of each cell depends on the demixing parameter: green ($DMP = 1$), red ($DMP = 0$), and blue ($0 < DMP < 1$). Results in (a) and (b) are averages over ten independent samples and the value of τ_D is obtained for the liquid-like side.

adaptation time. Ideally, full control would imply $DMP = 1$. The lower the value of DMP, the less efficient is the use of a pattern. Let us define δ such that a tissue with $DMP < \delta$ is considered mixed. Since DMP increases monotonically with ϕ (see Fig. 5.3(b)), we take the limit of vanishing ϕ and DMP. From a Taylor expansion about $\phi = 0$, we obtain $DMP = \phi^4/120 + O(\phi^5)$. Thus, there is a minimum length,

$$L_{\text{min}} = \left[\frac{\tau D}{\alpha}\sqrt{120\delta}\right]^{\frac{1}{2}} \quad , \tag{5.9}$$

below which the cells in the tissue are mixed, which sets a lower bound for the size of the patterns.

So far, we considered a pair of target shape indices such that both sides are in a fluid-like state. We study now the solid-fluid case, by setting $p_A = 3.65$ and $p_B = 3.9$ (as before). Figure 5.5(a) shows the time dependence of the demixing parameter for the side A, B, and both sides. Different from the fluid-fluid case, where the time dependence of DMP was similar in both sides, here we observe that DMP vanishes for the liquid-like side, whereas in the solid-like side it saturates at ≈ 0.8. This break of symmetry is observed for a wide range of parameters, as seen in Fig. 5.5(b) from the dependence of the value of DMP on the left- and right-hand sides on τ/τ_D, where τ_D is that for the liquid-like state. For all values of τ/τ_D the demixing parameter is higher in the solid-like state than in the liquid one. This asymmetry stems from the difference in the effective value of the

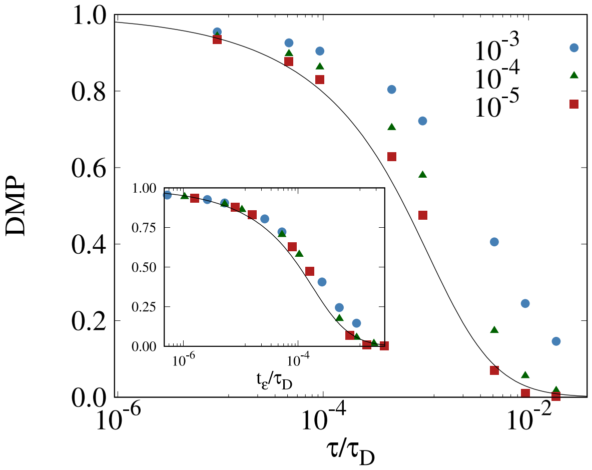

Figure 5.6: Asymptotic demixing parameter DMP as a function of τ/τ_D, for $N = 4096$. Different curves are for different values of ε, namely, 10^{-5}, 10^{-4}, and 10^{-3}. All the other parameters are the same as in the fluid-fluid case. In the inset, a data collapse is obtained when time is rescaled as proposed in Eq. 5.10. Results are averages over ten independent samples.

diffusion coefficient D in both sides. For the solid-like state, $D \approx 0$ and thus adaptation is much faster than diffusion. Cells have enough time to adapt to the new target shape index, which yields a high value of DMP that does not depend strongly on τ (see also snapshot for different values of τ in Fig. 5.3(c)). By contrast, for the liquid-like state, the value of DMP strongly depends on the value of τ as in the liquid-liquid case, see Fig. 5.3. In fact, the dependence of DMP on τ/τ_D in Fig. 5.5 for the liquid-like side is well described by Eq. (5.8), solid curve in Fig. 5.5(b) (further results for different substrates are discussed in the following subsections).

As in the fluid-fluid case it is important to highlight that the interface formed between adapted cells and the mixed ones for larger adaptation timescales is purely dynamical. Since the diffusion coefficient of the solid cells is almost negligible the time it takes for them to reach the boundary of the substrate increases with the distance to it. Thus, while the fluid side can mix with some of the solid cells that are closer to the boundaries, the rest of the solid cluster does not change significantly. Unfortunately, since the timescale for solid cells neighbor exchanges diverges when the tissues are in the solid state, we expect that the time for solid side mixing might be unreachable for any reasonable simulation efforts (or experimental)

5.3.1 Influence of ε on the results

In Eq. (5.5), the definition of alike cells depends on a threshold ε, which we fixed at $\varepsilon = 10^{-5}$. In practice, the value of these ε will depend on the experimental resolution to segregate cells by their type. Here, we study the dependence on ε.

Figure 5.6 shows the time dependence of the demixing parameter DMP for different values of ε for the fluid-fluid case. The larger the value of ε, the more cells are considered to be alike and therefore, the value of DMP is larger. To compare results for different values of ε, we compute the time t_ε that takes a cell to adapt to a new target shape index, within a threshold ε. The time evolution of the shape index is given by Eq. (5.4),

$$t_\varepsilon = \int_{\varepsilon}^{\Delta p_0} -\tau \ln\left(\frac{\varepsilon}{\delta_p}\right) d\delta_p \ , \tag{5.10}$$

where $\Delta p_0 = p_B - p_A$ is the change in shape index. In the inset of Fig. 5.6 we show that a data

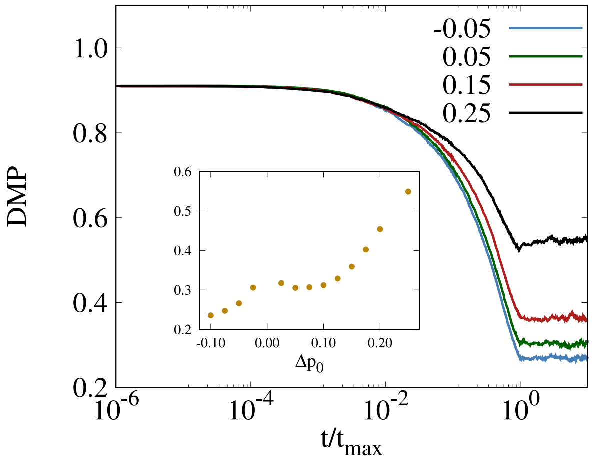

Figure 5.7: Time dependence of the demixing parameter DMP, where time is rescaled by $t_{\max} = -\ln(\varepsilon/\Delta p_0)$, with $N = 256$. Different curves are for different values of $\Delta p_0 = p_B - p_A$, where $p_B = 3.9$. In the inset is the asymptotic value of DMP as a function of Δp_0. Results are averages over 10^2 samples.

collapse is obtained for a wide range of values of ε (three orders of magnitude), if we plot DMP as a function of t_ε.

5.3.2 Dependence on Δp_0

As discussed previously, the properties of the tissue on each side of the substrate depend, not only on the target shape index of that side but also on the target value on the other side. Here, we explore the dependence on $\Delta p_0 = p_B - p_A$, defined as the difference in the target shape indices of both sides. For simplicity, we fix $p_B = 3.9$ and change p_A.

Figure 5.7 shows the time dependence of the demixing parameter for different values of Δp_0. For all values, DMP initially decreases and saturates asymptotically. In the inset, we plot the asymptotic value of DMP as a function of Δp_0, which reveals a non-monotonic behavior. From Eq. 5.10, we see that the time it takes for a cell to fully adapt to the new side depends on both τ and Δp_0. So, for vanishing Δp_0, cells crossing sides swiftly adapt to the local target shape index, leading to an increase in DMP.

5.4 Conclusion

We included the adaptation time of cells to external stimuli in a minimal model for confluent tissues. We found that the use of patterned substrates to regulate the tissue properties is compromised significantly when the adaptation time competes with the cell diffusion time. The latter depends on the characteristic length of the pattern L^*. From a continuum description based on a reaction-diffusion equation, we derived an analytic expression for the minimum length L_{min} for the pattern to be effective. For $L^* > L_{\text{min}}$, cells have enough time to adapt to the local cell-substrate interaction and the heterogeneous distribution of cell shapes reproduces the symmetries of the pattern, with a clear segregation by shape index. By contrast, for $L^* < L_{\text{min}}$, cells do not fully adapt to the local cell-substrate interaction and their shape index depends on their individual trajectories.

In the previous chapter we concluded that the cell size sets the relevant length scale for adaptation, thus the typical size of epithelial cells in confluent tissues ($L_{min} \approx 20\mu m$) sets the minimum length scale of the pattern for cells to be able to fully adapt. We can then calculate the expected adaptation time using the theory developed in this chapter. Using a typical diffusion coefficient for tissue cells of the order of $D \approx 0.1 \mu m^2 min^{-1}$, we estimate, using Eq. (5.9) with $\alpha = 0.276$ (large heterogeneity in substrate) and $\delta = 0.01$ (experimental resolution), that the typical time for a cell to adapt in a tissue interacting with a heterogeneous substrate is of the order of $\tau \approx 16$ hours. We have no knowledge of such measurements for cells in confluent tissues, but they fall within the relevant ranges for single cells adapting to heterogeneous substrates [130].

We considered a simple pattern but, it is straightforward to extend the conclusions to other patterns. In fact, the competition between diffusion and adaptation is so general that it should apply even to heterogeneous random substrates. These substrates are usually characterized by a correlation length ξ that plays the role of L^*, as seen in the previous chapter. So, only for $\xi > L_{\min}$, cells are expected to segregate based on their shape index, as defined by the local properties of the substrate. These results should be quite robust for different substrate patterns, even when the substrate is slightly curved, as long as one can assume that the curvature does not affect significantly cell-cell adhesion or the elasticity of the tissue [85]. However, for more extreme cases, it is known that curvature might lead to short and long-range collective motions [86].

The identification of the mechanisms responsible for the emergence of spatial cell patterns in a developing organism has been a subject of intensive research and discussion over the years [55, 132, 189, 194]. A recent study combines theory and experiments to show that cell sorting and compartmentalization in living organisms might be driven by surface tension due to differential adhesion [186]. However, the use of cell mixtures in vitro encompasses multiple challenges, which include the lack of control over the spatial distribution of cell types. We have shown that, above a certain length scale, the spatial distribution of cell properties can be controlled by the substrate pattern.

Although we only focused on changes to the shape of the cells, more specifically the cells perimeter, it is expected that the substrate can affect other properties. Previous works [186] have shown that the dynamics of mixtures is much less sensitive to differences in cell area than perimeter. Thus, we expect that, changes in area will lead to more subtle and potentially less consequential effects.

For simplicity, we assumed that the cell-cell and cell-substrate interactions depend on the substrate but not on the cell itself. A recent study shows that a broad distribution of the shape index of cells affects the tissue rigidity and, consequently, the cell diffusion coefficient [8]. Furthermore, we considered the adaptation time to be the same for all cells, but in a more realistic description this adaptation time might depend on other properties, like the cell geometry. Understanding the role of cell heterogeneities in the adaptation time is a question of interest for future studies.

In this study, for simplicity, we focused strictly on a 2D description, but a 3D generalization is possible. In the case of a simple generalization of the model to 3D [61], then we would expect similar results since a similar fluid to solid transition is present and cells are able to diffuse through the tissue. If we consider a more realistic description of a 3D epithelial monolayer, then we would need to go to a vertex model description that would follow something along the lines of [153] and characterize the apical and basal sides of the cells differently. Here, it could be expected that the competition between the basal and apical perimeter difference to play a role in the diffusion of the cells in the tissue. This would be something interesting to explore in future studies.

Here, we also neglected both cell death and division. Due to modelling constraints, it is required that the number of cells remains constant throughout the simulation. Other works explore the effect of cellular division [98], and in the context of patterned substrates it would be interesting for future studies to focus on how cell division or death could play a role in the mixing of the tissue.

Chapter 6

Non-confluent Self-Propelled Voronoi model

The dynamics of cell adhesion, motility, and proliferation on substrates poses technological and fundamental challenges in studies of morphogenesis, wound healing, and cancer. The dynamics evolves through (cell) shape changes and local rearrangements in response to stimuli from the surrounding medium as a result of the cell-cell correlations. Despite the inherent complexity, the relevant mechanisms can be isolated and used to develop realistic but tractable models. In this chapter we explore the Self-Propelled Non-Confluent Voronoi Model to shed light on some of the theoretical challenges in describing tissue development. We focus on the region of parameters which promotes cell adhesion and characterize some of the different properties of cell colonies, from colony growth to force distribution.

6.1 Motivation

In vitro experiments of cell-tissue morphogenesis, wound healing, and cancer rely on the capability of growing tissues on substrates [100, 196]. This poses practical and fundamental challenges that are motivating an enthusiastic and exciting body of research [1, 25, 32, 169]. For practitioners, it is key to control the morphology and mechanical robustness of the growing tissue, while guaranteeing a sustained delivery of nutrients to all cells. Theoretically, this problem resonates with traditional topics of soft-condensed matter: nonequilibrium dynamics, adhesion/wetting, transport in disordered media, and membrane mechanics [57, 60, 129].

For simplicity, most discrete models have considered either rigid or soft particles, mainly non-deformable, isotropic, and passive [59, 129, 197, 198]. Such extreme simplification provided us with a solid theoretical knowledge on how the equilibrium and some of the non-equilibrium properties depend on the type of interactions and competing timescales, and on the role of chemical/physical patterns imprinted on the substrate. However, for cells, this simplification is not satisfactory for two main reasons. 1) Cells are active particles, as they can collect energy from their surroundings and convert it into directed motion. 2) Cells shape changes in response to several stimuli. These two features are important in the dynamics and cannot be neglected [29].

Theoretical studies of cells have focused on two opposite limits: very detailed descriptions of a single cell [31,33,142,199] or coarse-grained descriptions of the entire tissue [2,22,45,46]. While the former describes the mechanical and biochemical behavior at very short length and time scales, the latter focus on the macroscopic mechanical properties of the tissue, but requires apriori knowledge of the spatial distribution of cells and cell features. The bridge between these very relevant limits is still elusive.

In this chapter we expand the previously introduced SPV model to allow for holes in the tissue. For this, a new length scale is introduced, the maximum radius of the cells, l. Thus, as cells grow apart, they will eventually separate and adopt a circular form. Recent studies on the Non-Confluent Voronoi model have established its different phases, from the individual cell system (Gas phase) to the fully confluent tissue [137]. Building on top of it, we explore the parameter region which promotes cell adhesion and focus on the growth of cell colonies. We try to elucidate some of the relevant mechanisms of tissue growth. We introduce activity to the equations of motion and focus on the study of the colonies surface tension. We observe that there is a linear dependence of the surface tension on activity strength and quantify the growth of the colony as a function of the geometrical parameters of the model.

6.2 Methods

We model the non-confluent tissue of N cells using the Self-Propelled Non-Confluent Voronoi model [137]. Each cell i is represented by its center $\mathbf{r}_i$ and its shape is given by the Voronoi tessellation of the space. To consider tissue boundaries, we introduce a new length scale l, which corresponds to the maximal radius of the cell. Thus, after performing the Voronoi tessellation, we check if all vertices are within a circle of radius l centered in i. The ones that are at a distance larger than l are excluded from the triangulation and a circumference arc of radius l between the unconnected vertices is drawn. This new curved interface corresponds to a boundary between the cell and the surrounding medium, while straight line interfaces connecting two cells perform the same role as in the previous model. The stochastic trajectories of cells are obtained from the equation of motion,

$$\frac{\mathrm{d}\mathbf{r}_i}{\mathrm{d}t} = \mu \mathbf{F}_i + v_0 \hat{\mathbf{n}}_i, \tag{6.1}$$

where $\mathbf{F}_i$ is the net force acting on cell i, μ is the mobility of the cell, v_0 the self-propulsion speed, and $\hat{\mathbf{n}}_i = (\cos\theta_i, \sin\theta_i)$ is a polarity vector which sets the direction of the self-propulsion force. For simplicity, we consider that θ_i is a Brownian process given by,

$$\dot{\theta}_i = \eta_i(t),\ \langle \eta_i(t)\eta_j(t')\rangle = 2D_r\delta(t-t')\delta_{ij}, \tag{6.2}$$

where $\eta_i(t)$ is an uncorrelated random process of zero mean and its variance sets the rotational diffusion D_r.

The net force $\mathbf{F}_i$ describes the many body cell-cell and cell-environment interaction and it is given by $\mathbf{F}_i = -\nabla_i E$, where $E = \sum E_i$ and E_i is the energy functional for cell i,

$$E_i = K_A[A_i - A_0]^2 + \Gamma P_i^2 + \Lambda_{<i,j>} P_i \ , \tag{6.3}$$

where A_i and P_i are the area and perimeter of cell i, respectively, and A_0 is the target area value. K_A is the area modulus, Λ is the line tension of the cell interfaces and Γ is related to the strength of the contractility. The main difference to the previous confluent model is the Λ term which not only accounts for the line tension between adhered cells but also between cells and their surrounding medium. For simplicity, we consider that the tension is equal in both cases and thus the energy functional reduces to the standard:

$$E_i = K_A[A_i - A_0]^2 + K_P[P_i - P_0]^2 \ , \tag{6.4}$$

where A_i and P_i are the area and perimeter of cell i, respectively, and A_0 and P_0 are their target values. K_A and K_P are the area and perimeter moduli. Physically, it is more appropriate to consider different tensions for cell-cell and cell-environment interfaces. However, this does not affect the phase diagram qualitatively, but merely moves the location of the phase boundaries, as shown in Ref. [137]. Without loss of generality, below, all lengths are in units of l and time is in units of $1/(\mu K_P l)$.

In Ref. [137], the different phases of the model are explored. In addition to the confluent phase for high adhesion, five other phases are reported, a schematic summary is shown in Fig. 6.1. These can be understood in the context of cell-cell interactions and geometrical constraints. In this model, vertices can be shared by either two or three cells. One can estimate analytically what is the typical force between an isolated pair (in a line configuration) and a triplet of cells (in a triangular configuration). These two and three-cell interactions can be calculated from Eq. (6.4), for a given P_0 and A_0. In the case where both interactions are negative, all cells repel each other and the system is in the gas phase. When the two-cell interaction is positive but the three-cell one is negative, one finds the hexagonal phase, where cells are able to overlap but do not form three cell connections, thus, large clusters cannot be formed. Due to this, each cell will have six neighbors leading to a configuration similar to the hexagonal packing. The inverse case, positive three-cell and negative two-cell interaction, leads to the cluster phase. Here, clusters of cells are formed due to the initialization protocol of the model. Since the position of cells is randomly generated, some are close to each other and the ones which form a three cell cluster will stay connected since three-cell interactions promote aggregation. On the other hand, since the two-cell interaction is repulsive, the clusters will not be able to merge leading to multiple segregated clusters. The last three phases are characterized by geometrical constraints since the two and three-cell interactions are positive. These interactions promote cell aggregation which leads to a large cell cluster that contains all cells. As mentioned, there is a phase corresponding to the confluent tissue where all cells are connected without any gaps. Then, there is also a minimal phase which can have small gaps and is observed when the constraints set by the energy functional are met, $\bar{P}_i = P_0$ and $\bar{A}_i = A_0$. This phase is like the fluid-like phase of the SPV model since there are no barriers for cell rearrangements, while the confluent phase is similar to the solid-like one [2]. Lastly, there is a non-confluent phase, where all cells still form a large connected cluster but there are gaps in the tissue, due to the maximal radial size of the cells. This happens for large P_0 and small A_0, where cells want to expand but still want to aggregate, since the two and three-cell interactions are positive. This leads to some cells distancing far apart, no longer satisfying their maximal radius constraint and a hole is formed.

For the simulations, we used a recently developed hybrid CPU/GPU software package, cellGPU [99], for the Self-Propelled Voronoi model and introduced the mechanism for non-confluent tissues described above. The equations of motion, Eq. (5.1), are integrated using the Euler method, with a time step of $\Delta t = 10^{-3}$. We impose periodic boundary conditions, $D_r = 1$, $v_0 = 0.1$, and $K_A = K_P = 1$. To generate the initial configuration, we generate N positions at random and let the system relax over 10^4 time steps.

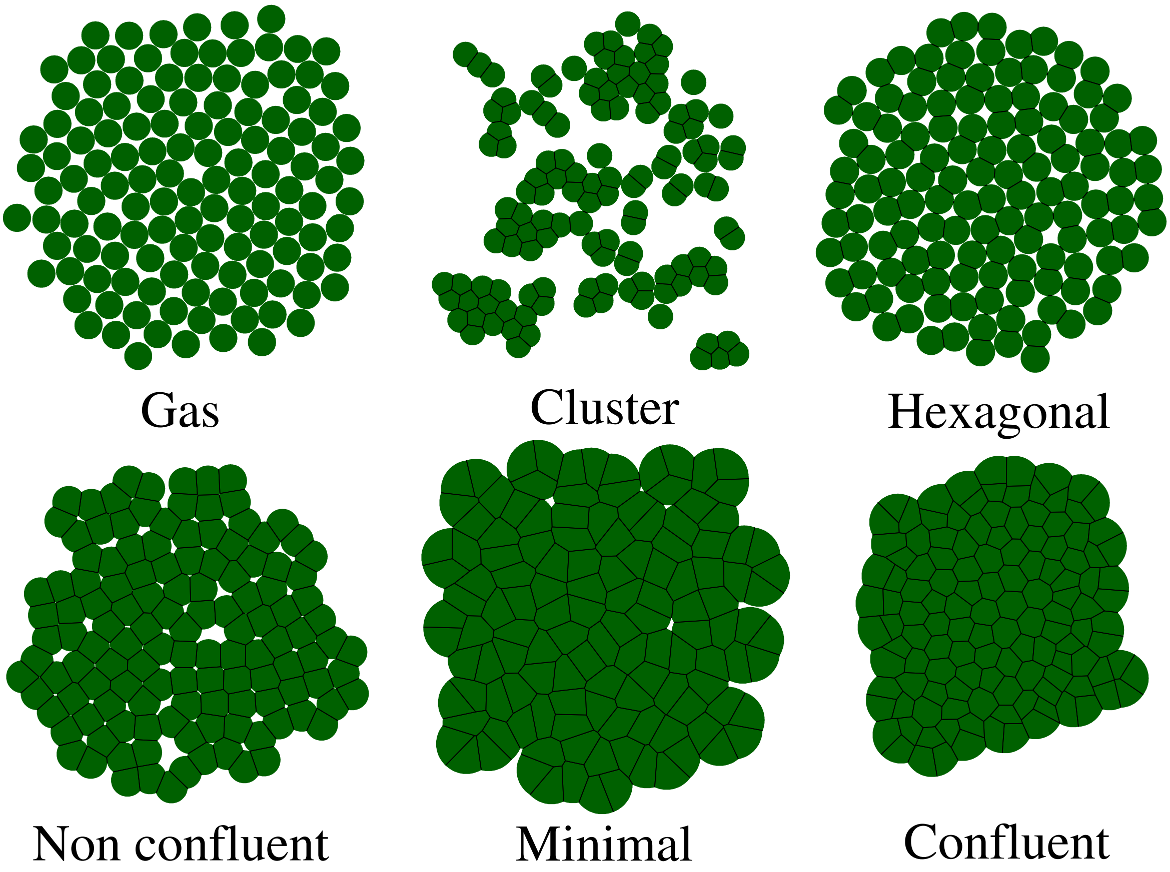

Figure 6.1: Schematic representation of the different phases of the model. In the Gas phase, the two and three-cell interactions are repulsive which makes cells move away from each other. In the Cluster phase, two-cell interactions are repulsive but three-cell ones are attractive leading to small clusters of cells that are formed at the start and never break, since two different clusters cannot merge given that they need two-cell contacts. Some two-cell cluster configurations are also stable, if during the initialization protocol they start sufficiently close together, since for small distances between two cell centers, the two-cell interaction can be attractive. The Hexagonal phase is characterized by attractive two-cell interactions but repulsive three-cell ones. This leads to a packing similar to hexagonal with multiple two-cell contacts. In the bottom row are the phases with both attractive two and three-cell interactions. In the Non confluent phase, cells are constrained by their maximal radius leading to holes in the tissue. In the Minimal phase the energy of the cells is close to their minimum ($P_i = P_0$ and $A_i = A_0$). In the Confluent phase the tissue is in a glassy state.

6.3 Results and discussion

We focus on the parameter space where the cells are in the confluent phase (see Fig. 6.1), which corresponds to $P_0 < q_5\sqrt{A_0}$, where $q_5 \approx 3.8$ is the shape parameter of a regular polygon with five sides. This is the same curve that separates the solid to fluid transition in the space-filling confluent tissues in the SPV model. As the tissue is able to form five sided polygons, the energy barriers for cell rearrangements decrease significantly leading to more frequent neighbor exchanges. This sector of the parameter space will allow us to probe several properties of cell colonies and how they develop until a fully confluent tissue is formed.

In Fig. 6.2 we show how the energy of the cells in the periphery of the colony changes with cell number. Since we focus on the confluent phase, the periphery of the colony is defined as the cells which share an interface with the surrounding medium, while cells in the bulk only share interfaces with other cells. As such, we sum the energy of each individual cell in the periphery of the colony (E_{per}) and normalize it by the total energy (E_{total}), as given by Eq. (6.4). Note that, from Eq. (6.4),

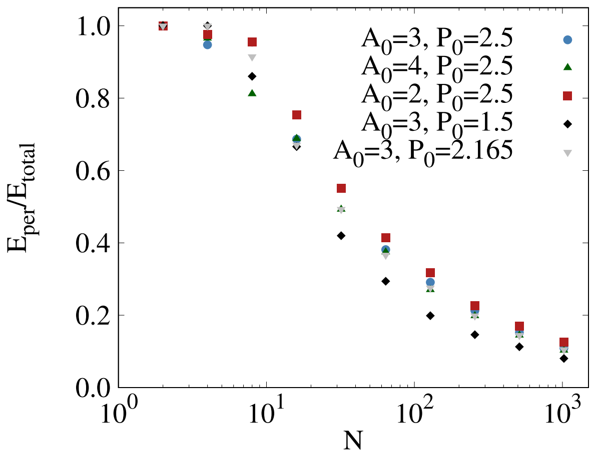

Figure 6.2: Normalized periphery energy of the colony as a function of the number of cells. These results were averaged over 10 samples. For small colonies, all cells are at the boundary, thus $E_{per} = E_{total}$. As N increases the main contribution to the cell colony shifts to the bulk.

since the cell-cell and cell-environment line tensions are considered equal, the difference between cells in the periphery and in the bulk is purely geometrical. Cells in the bulk will be surrounded by other cells and thus have a regular polygonal shape, while cells in the periphery are missing neighbors and thus have a curved arc which sets the border with the surrounding medium. We observe that for small N, all cells are in the periphery of the colony and as such $E_{per} = E_{total}$, but as N increases, the number of cells in the bulk increases and the largest fraction of the energy in the colony is that of bulk cells. While different P_0 and A_0 change the distribution of energy in the colony, these parameters do not change its behavior significantly. For higher N, the largest fraction of the energy comes from the bulk where cells share similar shape distributions, thus similar energy.

Although the energy of the periphery of the cluster is still non-negligible (around 10% of the total) for the largest colony sizes ($N = 1024$), in Fig. 6.3, we show that the way the colony grows is similar for smaller values of N. Here, we show how the radius of the colony grows with N. The radius is measured by approximating the colony to a circle of radius R. As such, we measure the total area of the colony and calculate its radius using, $R = \sqrt{A_{total}/\pi}$, where $A_{total} = \sum_i A_i$. We observe that the radius of the colony increases as $\sqrt{N}$ for $N \geq 10$. These results suggest that although the contribution of the bulk to the total energy of the tissue is still small (around 20%), it already has the required number of cells for the colony to form a more regular circular shape. Since the periphery grows with $\sqrt{N}$ and the bulk with N, eventually the contribution of the periphery to the total energy of the tissue is negligible.

We quantify how the different parameters play a role in shaping the periphery of the colony by analyzing its surface tension (γ). We measure γ by a least squares linear fit of the periphery energy (E_{per}) as a function of $\sqrt{N}$. Since this dependence is linear in the asymptotic limit, we can use its slope to quantify the surface tension of the colony. Figure 6.4 shows how the surface tension of the colony changes with the activity of the cells (left) and with P_0 and A_0 (right). The left plot shows that the surface tension of the colony grows approximately linearly with the activity of the cells. In the right plot, the blue circles correspond to simulations where we fix $A_0 = 3$ and change P_0, while the green triangles correspond to simulations where we fix $P_0 = 2.5$ and vary A_0. We have plotted this data as a function of the shape parameter $P_0/\sqrt{\bar{A}}$, where $\bar{A}$ corresponds to the average area of all the cells in the colony. This is one of the adimensional quantities commonly used in the literature as a control parameter [2, 61, 83, 137]. We observe data collapse, but more simulations would be

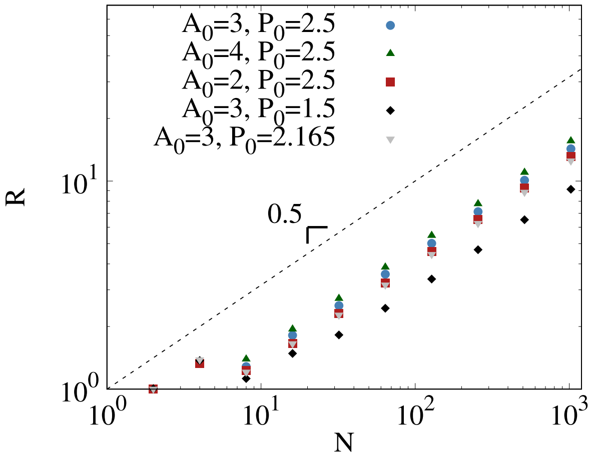

Figure 6.3: Radius of the cluster as a function of the number of cells in the colony. These results were averaged over 10 samples. A straight dashed line for $\sqrt{N}$ is shown in black. The radius of the colony is calculated by approximating it to a circle, thus $R = \sqrt{A_{total}/\pi}$, where $A_{total} = \sum_i A_i$. For larger cell colonies we can see that their radius follows the straight line. This happens at $N \gtrsim 10$.

needed to thoroughly verify its validity. We find that changes to A_0 play a much larger role to the periphery mechanics than changes to P_0. This is in contrast to space-filling tissue simulations where the relevant parameter is P_0 and $\bar{A}$ is usually fixed [2, 61, 83, 137]. Recent work has also shown how different A_0 do not seem to play a relevant role in the dynamics of the tissue [186]. These results highlight the difference between bulk and periphery mechanics. While bulk is mainly controlled by P_0, the periphery changes more with A_0. This is also supported by the phase diagram of the model [137], where by increasing P_0 the colony always stays connected but the dynamics changes significantly from the Confluent, to the Minimal and finally the Non Confluent phase. By contrast, when increasing A_0, the colony eventually breaks since there is not enough adhesion between cells. Thus, the colony will survive while the adhesion is kept between the peripheral cells, which is mostly affected by A_0.

6.4 Conclusion

In this chapter we analysed the surface properties of the Non-Confluent Voronoi model. We focused on the confluent phase of the model where cells attract each other to form a cohesive cell colony and studied how it grows and its surface properties. We found that, as the number of cells in the colony increases, the contribution of the cells in the bulk to the total energy of the colony dominates over the cells in the periphery. We show that for $N > 10$, the periphery will typically grow with the radius of the colony, while the bulk grows with the area. Thus, as N increases, there is a crossover between a colony where the periphery contributes significantly to its properties to a tissue where the bulk completely dominates and the periphery can be neglected. We also show that the surface tension of the colony scales linearly with the activity of the cells. We observed a data collapse of our results for the surface tension as a function of $P_0/\sqrt{\bar{A}}$.

More simulations are needed to assess the data collapse in Fig. 6.4, but the results already provide insight into the relevant parameters of the model. As in the confluent version, this geometrical parameter seems to play a relevant role in controlling the dynamics of the cells [2, 45, 46, 83]. In the confluent models, the parameter simplifies since $\bar{A} = 1$, but in the non-confluent one, the colony does not span the entire simulation box and, as such, different cells will have varying areas, espe-

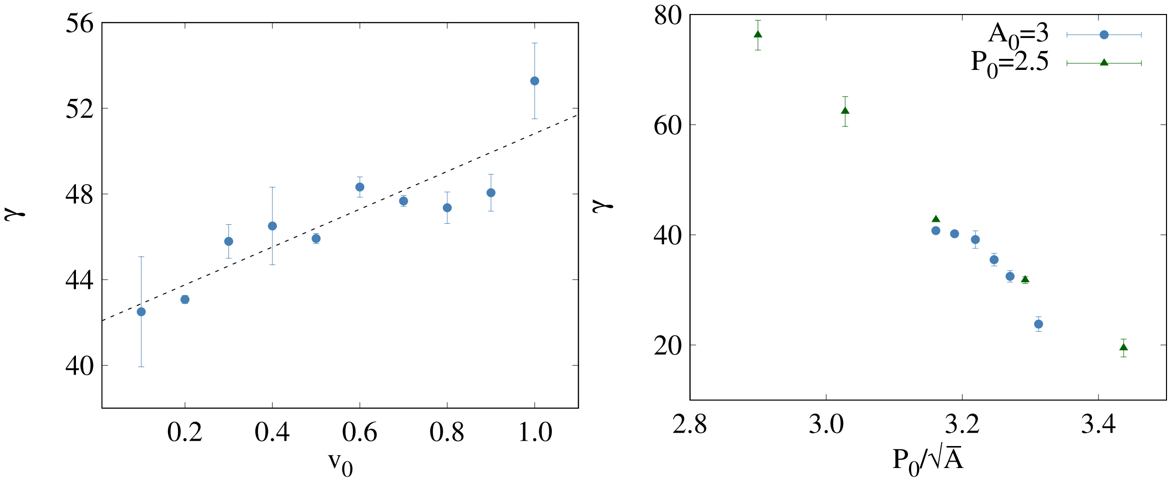

Figure 6.4: Surface tension in cell colonies. On the left is the surface tension (γ) as a function of activity (v_0). Note that the surface tension of the colony increases linearly with activity. The black line is given by $\gamma(v_0) = 8.8v_0 + 41.9$. These results were taken for $P_0 = 2.5$ and $A_0 = 3.0$. On the right is the surface tension (γ) as a function of $P_0/\sqrt{A}$. These results were taken for $v_0 = 0.1$. This scaling was used to collapse the data but more simulations are needed to assess its validity. The results in blue (circles) were taken by fixing $A_0 = 3$ and varying P_0 from 2.5 to 3.5 in steps of 0.2. The ones in green (triangles) were taken by fixing $P_0 = 2.5$ and varying A_0 from 2 to 4 in steps of 0.5. The surface tension was calculated through a linear fit of the energy of the peripheral cells as a function of $\sqrt{N}$ for large cell numbers ($N \geq 128$). All results were averaged over 10 samples.

cially when comparing cells in the bulk to cells in the periphery. Recent works have developed a minimal length approach to unify rigidity in underconstrained systems like the Vertex model and spring networks [61,62]. This approach may also be extended to non-confluent models, especially if the same parameter controls the properties of the cells.

Previous work has focused on a similar non-confluent system using the Vertex model [160], where the interactions between cells are changed to differentiate between cells and surrounding medium. The model remains similar to its confluent counterpart but since some cells now correspond to empty space, the tissue is allowed to reach a non-confluent state. The model also introduces tension fluctuations on the cell edges to mimic real cell colonies. Given the similarities between the dynamics of the confluent Voronoi and Vertex models [84], it would be interesting to extend this feature to the non-confluent regime. From a qualitative point of view, the phases observed in Ref. [160] are similar to the ones of Fig. 6.1, suggesting that both models remain similar in the non-confluent regime.

The mechanical properties of the tissues have been shown to be driven by universal properties related to topology and geometry of the individual cells [76, 94, 200]. These results have also been supported by simulations of the Vertex and Voronoi models [2, 83]. In the non-confluent model, our results suggest that this universality can be extended to colonies with as little as 20 cells. In the case of smaller colonies, especially when there are no cells in the bulk, the colonies can become unstable. This is due to the irregular shapes that result from the Voronoi tessellation when the number of cells is small. This may lead to instabilities when the cell centers are too close and are pushed out of the cluster. In the future, steps should be taken towards improving the model for small cell numbers. One possibility is adding *empty cells* as in Ref. [160] which are meant to model the holes in the tissue but allow for the addition of more stabilizing elements to the model. Being able to reach colonies with small number of cells is necessary to bridge the results known for tissues [76,94,200] to what is seen in small colonies [132].

The results reported here considered equal interactions between cells and cell-environment. Other works have shown that this simplification does not play a qualitative role in the phases of the model [137]. Furthermore, recent work has shown that the topology of tissues is universal even for different substrates [200]. Nonetheless, an interesting avenue for future studies is to introduce a different interaction between the cells and the environment. One possibility is to introduce heterogeneity via a substrate, as we explored in previous chapters, to understand if the cell-environment interaction can play a more relevant role.

Chapter 7

Conclusions

In this thesis, we explored the properties of epithelial confluent tissues using the Self-Propelled Voronoi model, which describes the cells using a Voronoi tilling of the space. The cell-cell interaction is given by an energy functional, quadratic in the perimeter and area of the cells. Using the shape index as a control parameter (ratio between the preferred perimeter and square root of the average area), previous works have shown that the model has a crossover between a solid-like and a fluid-like state, set by the increase of cell motility in the tissue. This is reminiscent of the glassy behavior in particulate systems, although recent work revealed an anomalous glassy dynamics. Its athermal limit also shows atypical behavior by being rigid throughout the whole range of parameters previously explored. In chapter two, we have discussed in detail these results and shed light on the state of the model, as well as on some open questions. This allowed us to highlight which relevant biological aspects the model captures, as well as its shortcomings.

In chapter three, we focused on the athermal limit. We explored the structure of the energy landscape with the objective of rationalizing conflicting results in the literature. We showed that to uncover the hierarchy of the energy landscape one needs to introduce a new metric. While using a standard contact metric, as is typical in particulate systems, we observed no structure. By changing to a metric that takes into account the energy of the cells, the hierarchical structure becomes apparent. While for particle systems the inter-particle distance enters in the pair-wise interactions, in the Voronoi model, the interactions are many body and depend on the perimeter and area of the cell. This means that, even if the contact network does not change substantially, the energy contact metric does. This result allowed us to uncover a new disordered state. While for low shape index the tissue is rigid and ultrametric, for high values of the shape index the rigidity remains, but there is a change in the energy landscape. In this second regime, the landscape is populated by flat minima (which always relax the tissue to the same state) and is no longer ultrametric. This has consequences to other systems where many body interactions are relevant given that such hierarchy can depend on the metric.

When introducing activity to the model, the cells are able to overcome some of these small energy barriers and eventually diffuse throughout the tissue. In chapter four, we introduced the substrate as a component of the model. We considered a heterogeneous substrate interaction that is spatially dependent and changes the shape index of the cell. By making a comparison between substrate and cell disorder, where the heterogeneity is in the shape index of the individual cells, we are able to understand how different types of disorder can change the mechanical properties of the tissue. Although both cases may be considered as *quenched*, the main difference comes from the source of the disorder and may lead to different outcomes. In the cell disorder, the tissue always becomes more rigid with increasing disorder. On the other hand, the substrate disorder can either increase or decrease the tissues rigidity. When using an averaging protocol to smooth the substrate disorder we are able to show that when the correlation length in the spatial distribution of the shape index is smaller than the typical cell size, the cells become more motile, while when it is greater, they become less motile. We found that this increase (or decrease) in rigidity is accompanied by percolation of rigid cells. For the most rigid tissues, the results resemble those of cell disorder. This highlights the differences between disorders. When cells explore different regions of the substrate with a small correlation length, the mechanical properties of the tissue are substantially different. By contrast, for larger correlation lengths, the averaging of the substrate disorder provides a larger area for the cells to relax, leading to similar behavior as cell disorder. Thus, although the quench is different in both types of disorder, the cell disorder provides a self-averaging mechanism that is similar to that of the substrate.

Given the complex internal biochemical structure of the cells, the response to the interaction with the substrate is not always instantaneous but might take a characteristic time set by the chemical and physical response of its internal structures. In chapter five, we introduced a characteristic time scale for cell adaptation into the substrate interaction to complement the previous work. To simplify the problem we considered a different geometry for the substrate pattern consisting of two half-planes. We focused on the segregation effect of the substrate as a function of the adaptation and motility of the cells. While for lower values of the characteristic time scale for adaptation (or lower motility of the cells), the substrate fully segregates the tissue based on the shape index, as this time increases, the tissue cells eventually mix. We introduced a continuum model which captures this behavior using a simple reaction-diffusion equation, which takes into account the diffusion of the cells and the rate at which they adapt to the substrate. We found very good agreement between this analytically solvable model and the simulation results. The results of the previous chapter allowed us to set a minimum length for substrate patterns, the typical cell size. By combining this result with the continuum model, we were able to estimate the adaptation time of the cells in tissues. Although we are not aware of such measurements, our results fall within relevant ranges of single cell values, highlighting the impact of the results for experiments.

Lastly, we focused on a non-confluent version of the model to shed light on the bridge between small colonies of cells and large confluent tissues. In chapter six, we explored the properties of cell colonies as the number of cells increases. We showed that even with a small number of cells in the bulk, cell colonies exhibit a similar growth for as low as 10 cells. We then calculated the surface tension and showed that it increases linearly with activity. We also found indications of data collapse of the surface tension as a function of the shape index in the non-confluent tissue. More simulations are needed to confirm this collapse. Recent studies have proposed a minimum length approach to understand the transition from the solid to fluid tissues, which could possibly be extended to non-confluent models. Other studies have also focused on non-confluent versions of the Vertex model. Given the similarities between the confluent limits, it would be interesting to explore the similarities in the non-confluent phases. The non-confluent models can also provide a link between standard particle models and confluent tissues. In the non-confluent cases, density plays a more explicit role which may allow a simpler relation between them, thus providing a complementary approach to investigate the differences of their glassy behavior and the understanding of the glass transition.

Is there universality in biology? The results presented in this thesis suggest that the answer is yes. The SPV model has been quite successful at predicting the mechanical properties of different epithelial tissues, in different organisms, from human bronchial cells [76] to Zebrafish [94]. The similarities between these network models and standard particulate systems, also highlights the universality of biological systems. Even though they are complex and intrinsically out of equilibrium, their properties have been, in many cases, explained using existing physical models. Continuum models or simple discrete ones, like the example studied in this thesis, have been remarkably successful at capturing the relevant physics of biological systems, but also at predicting their behavior. Even if a generalized theory of out of equilibrium statistical mechanics is out of reach, current results have pointed in the direction that there is universality in certain classes of these systems that can be captured by simple models. One *just* needs to formulate them in its proper language.

Bibliography

[1] R. Alert and X. Trepat, "Living cells on the move," *Phys. Today*, vol. 74, pp. 30–36, 2021.

[2] D. Bi, X. Yang, M. C. Marchetti, and M. L. Manning, "Motility-driven glass and jamming transitions in biological tissues," *Phys. Rev. X*, vol. 6, pp. 1–13, 2016.

[3] S. Hert and M. Seel, "dD Convex Hulls and Delaunay Triangulations," in *CGAL User Ref. Man.*, CGAL Editorial Board, 4.14 ed., 2019.

[4] M. Qi, T. T. Cao, and T. S. Tan, "Computing 2D constrained delaunay triangulation using the GPU," *IEEE Trans. Vis. Comput. Graph.*, vol. 19, pp. 736–748, 2013.

[5] T. T. Cao, A. Nanjappa, M. Gao, and T. S. Tan, "A GPU accelerated algorithm for 3D Delaunay triangulation," in *Proc. Symp. Interact. 3D Graph.*, pp. 47–54, Association for Computing Machinery, 2014.

[6] J. B. Kruskal, "On the shortest spanning subtree of a graph and the traveling salesman problem," *Proc. Am. Math. Soc.*, vol. 7, pp. 48–48, 1956.

[7] R. Rammal, J. Angles d'Auriac, and B. Doucot, "On the degree of ultrametricity," *J. Phys. Lettres*, vol. 46, pp. 945–952, 1985.

[8] X. Li, A. Das, and D. Bi, "Mechanical Heterogeneity in Tissues Promotes Rigidity and Controls Cellular Invasion," *Phys. Rev. Lett.*, vol. 123, pp. 1–16, 2019.

[9] K. Christensen and N. R. Moloney, *Complexity and Criticality*, vol. 1 of *Imperial College Press Advanced Physics Texts*. Imperial College Press, 2005.

[10] P. L. Krapivsky, S. Redner, and E. Ben-Naim, *A kinetic view of statistical physics*. Cambridge University Press, 2011.

[11] U. C. Täuber, *Critical dynamics: A field theory approach to equilibrium and non-equilibrium scaling behavior*. Cambridge University Press, 2012.

[12] C. Xue, Z. Liu, and N. Goldenfeld, "Scale-invariant topology and bursty branching of evolutionary trees emerge from niche construction," *Proc. Natl. Acad. Sci.*, vol. 117, pp. 7879–7887, 2020.

[13] H. Y. Shih and N. Goldenfeld, "Path-integral calculation for the emergence of rapid evolution from demographic stochasticity," *Phys. Rev. E*, vol. 90, p. 050702, 2014.

[14] E. A. Herrada, C. J. Tessone, K. Klemm, V. M. Eguíluz, E. Hernández-García, and C. M. Duarte, "Universal scaling in the branching of the tree of life," *PLoS One*, vol. 3, p. e2757, 2008.

[15] J. P. O'Dwyer, S. W. Kembel, T. J. Sharpton, and S. W. Pacala, "Backbones of evolutionary history test biodiversity theory for microbes," *Proc. Natl. Acad. Sci. U. S. A.*, vol. 112, pp. 8356–8361, 2015.

[16] B. Szabó, G. J. Szöllösi, B. Gönci, Z. Jurányi, D. Selmeczi, and T. Vicsek, "Phase transition in the collective migration of tissue cells: Experiment and model," *Phys. Rev. E*, vol. 74, p. 61908, 2006.

[17] A. Nicolas and I. Touloupas, "Origin of the correlations between exit times in pedestrian flows through a bottleneck," *J. Stat. Mech. Theory Exp.*, vol. 2018, p. 013402, 2018.

[18] A. Nicolas, M. Kuperman, S. Ibañez, S. Bouzat, and C. Appert-Rolland, "Mechanical response of dense pedestrian crowds to the crossing of intruders," *Sci. Rep.*, vol. 9, pp. 1–10, 2019.

[19] A. Nicolas, "Dense Pedestrian Crowds Versus Granular Packings: An Analogy of Sorts," in *Springer Proc. Phys.*, vol. 252, pp. 411–419, Springer, Cham, 2020.

[20] T. Vicsek, A. Czirk, E. Ben-Jacob, I. Cohen, and O. Shochet, "Novel type of phase transition in a system of self-driven particles," *Phys. Rev. Lett.*, vol. 75, pp. 1226–1229, 1995.

[21] J. Toner and Y. Tu, "Long-range order in a two-dimensional dynamical XY model: How birds fly together," *Phys. Rev. Lett.*, vol. 75, pp. 4326–4329, 1995.

[22] D. Bi, J. H. Lopez, J. M. Schwarz, M. L. Manning, and M. Lisa Manning, "Energy barriers and cell migration in densely packed tissues," *Soft Matter*, vol. 10, pp. 1885–1890, 2014.

[23] R. Alert and X. Trepat, "Physical Models of Collective Cell Migration," *Annu. Rev. Condens. Matter Phys.*, vol. 11, pp. 77–101, 2020.

[24] X. Trepat, M. R. Wasserman, T. E. Angelini, E. Millet, D. A. Weitz, J. P. Butler, and J. J. Fredberg, "Physical forces during collective cell migration," *Nat. Phys.*, vol. 5, pp. 426–430, 2009.

[25] X. Trepat and E. Sahai, "Mesoscale physical principles of collective cell organization," *Nat. Phys.*, vol. 14, pp. 671–682, 2018.

[26] G. T. Eisenhoffer, P. D. Loftus, M. Yoshigi, H. Otsuna, C. B. Chien, P. A. Morcos, and J. Rosenblatt, "Crowding induces live cell extrusion to maintain homeostatic cell numbers in epithelia," *Nature*, vol. 484, pp. 546–549, 2012.

[27] A. Szabó, R. Ünnep, E. Méhes, W. O. Twal, W. S. Argraves, Y. Cao, and A. Czirók, "Collective cell motion in endothelial monolayers," *Phys. Biol.*, vol. 7, p. 46007, 2010.

[28] E. M. Schötz, M. Lanio, J. A. Talbot, and M. L. Manning, "Glassy dynamics in three-dimensional embryonic tissues," *J. R. Soc. Interface*, vol. 10, p. 1098, 2013.

[29] A. S. Smith, "Physics challenged by cells," *Nat. Phys.*, vol. 6, pp. 726–729, 2010.

[30] C. Bechinger, R. Di Leonardo, H. Löwen, C. Reichhardt, G. Volpe, and G. Volpe, "Active particles in complex and crowded environments," *Rev. Mod. Phys.*, vol. 88, pp. 1–57, 2016.

[31] F. Höfling and T. Franosch, "Anomalous transport in the crowded world of biological cells," *Reports Prog. Phys.*, vol. 76, p. 046602, 2013.

[32] M. C. Marchetti, J. F. Joanny, S. Ramaswamy, T. B. Liverpool, J. Prost, M. Rao, and R. A. Simha, "Hydrodynamics of soft active matter," *Rev. Mod. Phys.*, vol. 85, pp. 1143–1189, 2013.

[33] N. Hodge and P. Papadopoulos, "Continuum modeling and numerical simulation of cell motility," *J. Math. Biol.*, vol. 64, pp. 1253–1279, 2012.

[34] M. E. Cates, "Diffusive transport without detailed balance in motile bacteria: does microbiology need statistical physics?," *Rep. Prog. Phys.*, vol. 75, p. 42601, 2012.

[35] A. Loisy, J. Eggers, and T. B. Liverpool, "How many ways a cell can move: The modes of self-propulsion of an active drop," *Soft Matter*, vol. 16, pp. 3106–3124, 2020.

[36] C. P. Broedersz and F. C. Mackintosh, "Modeling semiflexible polymer networks," *Rev. Mod. Phys.*, vol. 86, pp. 995–1036, 2014.

[37] J. Prost, F. Jülicher, and J. F. Joanny, "Active gel physics," *Nat. Phys.*, vol. 11, pp. 111–117, 2015.

[38] A. Munjal, J. M. Philippe, E. Munro, and T. Lecuit, "A self-organized biomechanical network drives shape changes during tissue morphogenesis," *Nature*, vol. 524, pp. 351–355, 2015.

[39] P. Kollmannsberger and B. Fabry, "Linear and nonlinear rheology of living cells," *Annu. Rev. Mater. Res.*, vol. 41, pp. 75–97, 2011.

[40] K. Kroy and J. Glaser, "The glassy wormlike chain," *New J. Phys.*, vol. 9, pp. 416–416, 2007.

[41] M. Weliky and G. Oster, "The mechanical basis of cell rearrangement. I. Epithelial morphogenesis during Fundulus epiboly," *Development*, vol. 109, pp. 373–386, 1990.

[42] H. Honda, Y. Ogita, S. Higuchi, and K. Kani, "Cell movements in a living mammalian tissue: Long-term observation of individual cells in wounded corneal endothelia of cats," *J. Morphol.*, vol. 174, pp. 25–39, 1982.

[43] G. W. Brodland, "Computational modeling of cell sorting, tissue engulfment, and related phenomena: A review," *Appl. Mech. Rev.*, vol. 57, pp. 47–76, 2004.

[44] H. Honda and G. Eguchi, "How much does the cell boundary contract in a monolayered cell sheet?," *J. Theor. Biol.*, vol. 84, pp. 575–588, 1980.

[45] R. Farhadifar, J. C. Röper, B. Aigouy, S. Eaton, F. Jü, and F. Jülicher, "The Influence of Cell Mechanics, Cell-Cell Interactions, and Proliferation on Epithelial Packing," *Curr. Biol.*, vol. 17, pp. 2095–2104, 2007.

[46] A. G. Fletcher, M. Osterfield, R. E. Baker, and S. Y. Shvartsman, "Vertex models of epithelial morphogenesis," *Biophys. J.*, vol. 106, pp. 2291–2304, 2014.

[47] C. M. Lo, H.-B. H. B. Wang, M. Dembo, and Y.-L. Y. L. Wang, "Cell Movement Is Guided by the Rigidity of the Substrate," *Byophys. J.*, vol. 79, p. 144, 2000.

[48] D. E. Discher, P. Janmey, and Y. Wang, "Tissue cells feel and respond to the stiffness of their substrate," *Science*, vol. 310, p. 1139, 2005.

[49] W. Guo, M. T. Frey, N. A. Burnham, and Y. Wang, "Substrate Rigidity Regulates the Formation and Maintenance of Tissues," *Biophys. J.*, vol. 90, p. 2213, 2006.

[50] S. Neuss, I. Blomenkamp, R. Stainforth, D. Boltersdorf, M. Jansen, N. Butz, A. Perez-Bouza, and R. Knüchel, "The use of a shape-memory poly(ϵ-caprolactone)dimethacrylate network as a tissue engineering scaffold," *Biomaterials*, vol. 30, p. 1697, 2009.

[51] M. Murrell, R. Kamm, and P. Matsudaira, "Substrate Viscosity Enhances Correlation in Epithelial Sheet Movement," *Biophys. J.*, vol. 101, p. 297, 2011.

[52] W. Song and J. F. Mano, "Interactions between cells or proteins and surfaces exhibiting extreme wettabilities," *Soft Matter*, vol. 9, p. 2985, 2013.

[53] R. Sunyer, V. Conte, J. Escribano, A. Elosegui-Artola, A. Labernadie, L. Valon, D. Navajas, J. M. García-Aznar, J. J. Muñoz, P. Roca-Cusachs, and X. Trepat, "Collective cell durotaxis emerges from long-range intercellular force transmission," *Science*, vol. 353, p. 1157, 2016.

[54] P. A. Janmey, D. A. Fletcher, and C. A. Reinhart-King, "Stiffness Sensing by Cells," *Physiol. Rev.*, vol. 100, p. 695, 2020.

[55] M. L. Manning, R. A. Foty, M. S. Steinberg, and E. M. E.-M. Schoetz, "Coaction of intercellular adhesion and cortical tension specifies tissue surface tension," *Proc. Natl. Acad. Sci. U. S. A.*, vol. 107, p. 12517, 2010.

[56] J. Russo, J. M. Tavares, P. I. Teixeira, M. M. Telo Da Gama, and F. Sciortino, "Reentrant phase diagram of network fluids," *Phys. Rev. Lett.*, vol. 106, pp. 1–4, 2011.

[57] C. S. Dias, C. Braga, N. A. Araújo, and M. M. Telo Da Gama, "Relaxation dynamics of functionalized colloids on attractive substrates," *Soft Matter*, vol. 12, pp. 1550–1557, 2016.

[58] C. S. Dias, J. M. Tavares, N. A. Araújo, and M. M. Telo Da Gama, "Dynamics of a network fluid within the liquid-gas coexistence region," *Soft Matter*, vol. 14, pp. 2744–2750, 2018.

[59] N. A. M. Araújo, C. S. Dias, and M. M. Telo da Gama, "Kinetic interfaces of patchy particles," *J. Phys. Condens. Matter*, vol. 27, p. 194123, 2015.

[60] N. A. M. Araújo, C. S. Dias, and M. M. Telo da Gama, "Nonequilibrium self-organization of colloidal particles on substrates: adsorption, relaxation, and annealing," *J. Phys. Condens. Matter*, vol. 29, p. 014001, 2017.

[61] M. Merkel and M. L. Manning, "A geometrically controlled rigidity transition in a model for confluent 3D tissues," *New J. Phys.*, vol. 20, p. 22002, 2018.

[62] M. Merkel, K. Baumgarten, B. P. Tighe, and M. L. Manning, "A minimal-length approach unifies rigidity in underconstrained materials," *Proc. Natl. Acad. Sci. U. S. A.*, vol. 116, p. 6560, 2019.

[63] T. E. Angelini, E. Hannezo, X. Trepatc, M. Marquez, J. J. Fredberg, and D. A. Weitz, "Glass-like dynamics of collective cell migration," *Proc. Natl. Acad. Sci. U. S. A.*, vol. 108, pp. 4714–4719, 2011.

[64] D. T. Tambe, C. Corey Hardin, T. E. Angelini, K. Rajendran, C. Y. Park, X. Serra-Picamal, E. H. Zhou, M. H. Zaman, J. P. Butler, D. A. Weitz, J. J. Fredberg, X. Trepat, C. C. Hardin, T. E. Angelini, K. Rajendran, C. Y. Park, X. Serra-Picamal, E. H. Zhou, M. H. Zaman, J. P. Butler, D. A. Weitz, J. J. Fredberg, and X. Trepat, "Collective cell guidance by cooperative intercellular forces," *Nat. Mater.*, vol. 10, p. 469, 2011.

[65] C. Pérez-Gonzáles, R. Alert, C. Blanch-Mercander, M. Gómez-González, T. Kolodziej, E. Bazellieres, J. Casademunt, and X. Trepat, "Active wetting of epithelial tissues," *Nat. Phys.*, vol. 15, p. 79, 2018.

[66] C. M. Nelson, R. P. Jean, J. L. Tan, W. F. Liu, N. J. Sniadecki, A. A. Spector, and C. S. Chen, "Emergent patterns of growth controlled by multicellular form and mechanics," *Proc. Natl. Acad. Sci. U. S. A.*, vol. 102, p. 11594, 2005.

[67] L. Richert, F. Vetrone, J. H. Yi, S. F. Zalzal, J. D. Wuest, F. Rosei, and A. Nanci, "Surface nanopatterning to control cell growth," *Adv. Mater.*, vol. 20, p. 1488, 2008.

[68] K. A. Davis, K. A. Burke, P. T. Mather, and J. H. Henderson, "Dynamic cell behavior on shape memory polymer substrates," *Biomaterials*, vol. 32, p. 2285, 2011.

[69] L. F. Tseng, P. T. Mather, and J. H. Henderson, "Shape-memory-actuated change in scaffold fiber alignment directs stem cell morphology," *Acta Biomater.*, vol. 9, p. 8790, 2013.

[70] H. Jeon, S. Koo, W. M. Reese, P. Loskill, C. P. Grigoropoulos, and K. E. Healy, "Directing cell migration and organization via nanocrater-patterned cell-repellent interfaces," *Nat. Mater.*, vol. 14, p. 918, 2015.

[71] P. Y. Mengsteab, K. Uto, A. S. T. Smith, S. Frankel, E. Fisher, Z. Nawas, J. Macadangdang, M. Ebara, and D. H. D.-H. Kim, "Spatiotemporal control of cardiac anisotropy using dynamic nanotopographic cues," *Biomaterials*, vol. 86, p. 1, 2016.

[72] C. Horejs, "A fluid state of mind," *Nat. Rev. Mater.*, vol. 3, p. 256, 2018.

[73] M. E. Brasch, G. Passucci, A. C. Gulvady, C. E. Turner, M. L. Manning, J. H. Henderson, M. Lisa Manning, and J. H. Henderson, "Nuclear position relative to the Golgi body and nuclear orientation are differentially responsive indicators of cell polarized motility," *PLoS One*, vol. 14, p. 1, 2019.

[74] K. Ghosh and D. E. Ingber, "Micromechanical control of cell and tissue development: Implications for tissue engineering," *Adv. Drug Deliv. Rev.*, vol. 59, p. 1306, 2007.

[75] N. S. Gov, "Traction forces during collective cell motion," *Adv. Drug Deliv. Rev.*, vol. 3, p. 223, 2009.

[76] J.-A. Park, J. H. Kim, D. Bi, J. A. Mitchel, N. T. Qazvini, K. Tantisira, C. Y. Park, M. McGill, S.-H. Kim, B. Gweon, J. Notbohm, R. Steward Jr, S. Burger, S. H. Randell, A. T. Kho, D. T. Tambe, C. Hardin, S. A. Shore, E. Israel, D. A. Weitz, D. J. Tschumperlin, E. Henske, S. T.

Weiss, M. L. Manning, J. P. Butler, J. M. Drazen, and J. J. Fredberg, "Unjamming and cell shape in the asthmatic airway epithelium," *Nat. Mater.*, vol. 14, p. 1040, 2015.

[77] S. Garcia, E. Hannezo, J. Elgeti, J. F. J.-F. Joanny, P. Silberzan, and N. S. Gov, "Physics of active jamming during collective cellular motion in a monolayer," *Proc. Natl. Acad. Sci. U. S. A.*, vol. 112, pp. 15314–15319, 2015.

[78] S. Grosser, J. J. Lippoldt, L. Oswald, M. Merkel, D. M. Sussman, F. F. Renner, P. Gottheil, E. W. Morawetz, T. Fuhs, X. Xie, S. Pawlizak, A. W. Fritsch, B. Wolf, L.-C. C. Horn, S. Briest, B. Aktas, M. L. Manning, J. A. Käs, and J. A. Kas, "Cell and Nucleus Shape as an Indicator of Tissue Fluidity in Carcinoma," *Phys. Rev. X*, vol. 11, p. 011033, 2021.

[79] K. Binder and A. P. Young, "Spin glasses: Experimental facts, theoretical concepts, and open questions," *Rev. Mod. Phys.*, vol. 58, pp. 801–976, 1986.

[80] L. Berthier and G. Biroli, "Theoretical perspective on the glass transition and amorphous materials," *Rev. Mod. Phys.*, vol. 83, pp. 587–645, 2011.

[81] L. M. Janssen, "Active glasses," *J. Phys. Condens. Matter*, vol. 31, pp. 1–21, 2019.

[82] J. A. Mitchel, A. Das, M. J. O'Sullivan, I. T. Stancil, S. J. DeCamp, S. Koehler, O. H. Ocaña, J. P. Butler, J. J. Fredberg, M. A. Nieto, D. Bi, and J. A. Park, "In primary airway epithelial cells, the unjamming transition is distinct from the epithelial-to-mesenchymal transition," *Nat. Commun.*, vol. 11, pp. 1–14, 2020.

[83] D. Bi, J. H. Lopez, J. M. Schwarz, and M. L. Manning, "A density-independent rigidity transition in biological tissues," *Nat. Phys.*, vol. 11, pp. 1074–1079, 2015.

[84] D. M. Sussman, M. Paoluzzi, M. C. Marchetti, M. L. Manning, M. Cristina Marchetti, and M. Lisa Manning, "Anomalous glassy dynamics in simple models of dense biological tissue," *Epl*, vol. 121, p. 36001, 2018.

[85] D. M. Sussman, "Interplay of curvature and rigidity in shape-based models of confluent tissue," *Phys. Rev. Res.*, vol. 2, pp. 1–7, 2020.

[86] S.-Z. Lin, Y. Li, J. Ji, B. Li, and X.-Q. Feng, "Collective dynamics of coherent motile cells on curved surfaces," *Soft Matter*, vol. 16, p. 2941, 2020.

[87] B. A. Camley and W.-J. J. Rappel, "Physical models of collective cell motility: From cell to tissue," *J. Phys. D. Appl. Phys.*, vol. 50, p. 113002, 2017.

[88] N. Sepúlveda, L. Petitjean, O. Cochet, E. Grasland-Mongrain, P. Silberzan, and V. Hakim, "Collective Cell Motion in an Epithelial Sheet Can Be Quantitatively Described by a Stochastic Interacting Particle Model," *PLoS Comput. Biol.*, vol. 9, p. e1002944, 2013.

[89] J. Bialké, J. T. Siebert, H. Löwen, and T. Speck, "Negative Interfacial Tension in Phase-Separated Active Brownian Particles," *Phys. Rev. Lett.*, vol. 115, p. 98301, 2015.

[90] J. M. Belmonte, G. L. Thomas, L. G. Brunnet, R. M. C. De Almeida, and H. Chaté, "Self-Propelled Particle Model for Cell-Sorting Phenomena," *Phy. Rev. Lett.*, vol. 100, p. 248702, 2008.

[91] S. Henkes, Y. Fily, and M. C. Marchetti, “Active jamming: Self-propelled soft particles at high density,” *Phys. Rev. E*, vol. 84, p. 40301, 2011.

[92] A. Nestor-Bergmann, G. Goddard, S. Woolner, and O. E. Jensen, “Relating cell shape and mechanical stress in a spatially disordered epithelium using a vertex-based model,” *Math. Med. Biol.*, vol. 35, pp. 1–27, 2018.

[93] J. M. López-Gay, H. Nunley, M. Spencer, F. di Pietro, B. Guirao, F. Bosveld, O. Markova, I. Gaugue, S. Pelletier, D. K. Lubensky, and Y. Bellaïche, “Apical stress fibers enable a scaling between cell mechanical response and area in epithelial tissue,” *Science*, vol. 370, p. eabb2169, 2020.

[94] A. Mongera, P. Rowghanian, H. J. Gustafson, E. Shelton, D. A. Kealhofer, E. K. Carn, F. Serwane, A. A. Lucio, J. Giammona, and O. Campàs, “A fluid-to-solid jamming transition underlies vertebrate body axis elongation,” *Nature*, vol. 561, pp. 401–405, 2018.

[95] K. P. Landsberg, R. Farhadifar, J. Ranft, D. Umetsu, T. J. Widmann, T. Bittig, A. Said, F. Jülicher, and C. Dahmann, “Increased Cell Bond Tension Governs Cell Sorting at the Drosophila Anteroposterior Compartment Boundary,” *Curr. Biol.*, vol. 19, p. 1950, 2009.

[96] H. Haga, C. Irahara, R. Kobayashi, T. Nakagaki, and K. Kawabata, “Collective movement of epithelial cells on a collagen gel substrate,” *Biophys. J.*, vol. 88, pp. 2250–2256, 2005.

[97] M. Czajkowski, D. Bi, M. L. Manning, and M. C. Marchetti, “Hydrodynamics of shape-driven rigidity transitions in motile tissues,” *Soft Matter*, vol. 14, pp. 5628–5642, 2018.

[98] M. Czajkowski, D. M. Sussman, M. C. Marchetti, and M. L. Manning, “Glassy dynamics in models of confluent tissue with mitosis and apoptosis,” *Soft Matter*, vol. 15, pp. 9133–9149, 2019.

[99] D. M. Sussman, “cellGPU: Massively parallel simulations of dynamic vertex models,” *Comput. Phys. Commun.*, vol. 219, pp. 400–406, 2017.

[100] S. Kaliman, C. Jayachandran, F. Rehfeldt, and A. S. Smith, “Limits of Applicability of the Voronoi Tessellation Determined by Centers of Cell Nuclei to Epithelium Morphology,” *Front. Psychol.*, vol. 7, p. 551, 2016.

[101] P. Charbonneau, Y. Jin, G. Parisi, C. Rainone, B. Seoane, and F. Zamponi, “Numerical detection of the Gardner transition in a mean-field glass former,” *Phys. Rev. E*, vol. 92, pp. 1–15, 2015.

[102] P. Charbonneau, J. Kurchan, G. Parisi, P. Urbani, and F. Zamponi, “Glass and Jamming Transitions: From Exact Results to Finite-Dimensional Descriptions,” *Annu. Rev. Condens. Matter Phys.*, vol. 8, pp. 265–288, 2017.

[103] C. Artiaco, P. Baldan, and G. Parisi, “Exploratory study of the glassy landscape near jamming,” *Phys. Rev. E*, vol. 101, pp. 1–15, 2020.

[104] A. Altieri, G. Biroli, and C. Cammarota, “Dynamical mean-field theory and aging dynamics,” *J. Phys. A Math. Theor.*, vol. 53, pp. 1–28, 2020.

[105] A. Baule, F. Morone, H. J. Herrmann, and H. A. Makse, "Edwards statistical mechanics for jammed granular matter," *Rev. Mod. Phys.*, vol. 90, pp. 1–64, 2018.

[106] L. Berthier, "Nonequilibrium glassy dynamics of self-propelled hard disks," *Phys. Rev. Lett.*, vol. 112, pp. 1–5, 2014.

[107] S. S. Ashwin, J. Blawzdziewicz, C. S. O'Hern, and M. D. Shattuck, "Calculations of the structure of basin volumes for mechanically stable packings," *Phys. Rev. E*, vol. 85, pp. 1–8, 2012.

[108] Y. W. Li, L. L. Y. Wei, M. Paoluzzi, and M. P. Ciamarra, "Softness, anomalous dynamics, and fractal-like energy landscape in model cell tissues," *Phys. Rev. E*, vol. 103, pp. 1–9, 2021.

[109] T. C. Lubensky, C. L. Kane, X. Mao, A. Souslov, and K. Sun, "Phonons and elasticity in critically coordinated lattices," *Reports Prog. Phys.*, vol. 78, p. 73901, 2015.

[110] O. K. Damavandi, V. F. Hagh, C. D. Santangelo, and M. L. Manning, "Energetic Rigidity: a Unifying Theory of Mechanical Stability," 2021.

[111] R. C. Dennis and E. I. Corwin, "Jamming Energy Landscape is Hierarchical and Ultrametric," *Phys. Rev. Lett.*, vol. 124, p. 78002, 2020.

[112] G. Parisi and F. Zamponi, "Mean-field theory of hard sphere glasses and jamming," *Rev. Mod. Phys.*, vol. 82, pp. 789–845, 2010.

[113] Q. Liao and L. Berthier, "Hierarchical Landscape of Hard Disk Glasses," *Phys. Rev. X*, vol. 9, p. 11049, 2019.

[114] T. Yeung, P. C. Georges, L. A. Flanagan, B. Marg, M. Ortiz, M. Funaki, N. Zahir, W. Ming, V. Weaver, and P. A. Janmey, "Effects of substrate stiffness on cell morphology, cytoskeletal structure, and adhesion," *Cytoskeleton*, vol. 60, p. 24, 2005.

[115] M. Guo, A. F. Pegoraro, A. Mao, E. H. Zhou, P. R. Arany, Y. Han, D. T. Burnette, M. H. Jensen, K. E. Kasza, J. R. Moore, F. C. Mackintosh, J. J. Fredberg, D. J. Mooney, J. Lippincott-Schwartz, and D. A. Weitz, "Cell volume change through water efflux impacts cell stiffness and stem cell fate," *Proc. Natl. Acad. Sci. U. S. A.*, vol. 114, pp. E8618–E8627, 2017.

[116] J. Devany, D. M. Sussman, T. Yamamoto, M. L. Manning, and M. L. Gardel, "Cell cycle–dependent active stress drives epithelia remodeling," *Proc. Natl. Acad. Sci.*, vol. 118, p. e1917853118, 2021.

[117] K. Wolf, M. te Lindert, M. Krause, S. Alexander, J. te Riet, A. L. Willis, R. M. Hoffman, C. G. Figdor, S. J. Weiss, and P. Friedl, "Physical limits of cell migration: Control by ECM space and nuclear deformation and tuning by proteolysis and traction force," *J. Cell Biol.*, vol. 201, pp. 1069–1084, 2013.

[118] S. Aznavoorian, M. L. Stracke, H. Krutzsch, E. Schiffmann, and L. A. Liotta, "Signal transduction for chemotaxis and haptotaxis by matrix molecules in tumor cells," *J. Cell Biol.*, vol. 110, pp. 1427–1438, 1990.

[119] J. T. Smith, J. T. Elkin, and W. M. Reichert, "Directed cell migration on fibronectin gradients: Effect of gradient slope," *Exp. Cell Res.*, vol. 312, pp. 2424–2432, 2006.

[120] P. P. Provenzano, D. R. Inman, K. W. Eliceiri, S. M. Trier, and P. J. Keely, “Contact guidance mediated three-dimensional cell migration is regulated by Rho/ROCK-dependent matrix reorganization,” *Biophys. J.*, vol. 95, pp. 5374–5384, 2008.

[121] D. T. Butcher, T. Alliston, and V. M. Weaver, “A tense situation: forcing tumour progression,” *Nat. Rev. Cancer*, vol. 9, pp. 108–122, 2009.

[122] R. Sinkus, J. Lorenzen, D. Schrader, M. Lorenzen, M. Dargatz, and D. Holz, “High-resolution tensor MR elastography for breast tumour detection,” *Phys. Med. Biol.*, vol. 45, p. 1649, 2000.

[123] G. Ciasca, T. E. Sassun, E. Minelli, M. Antonelli, M. Papi, A. Santoro, F. Giangaspero, R. Delfini, and M. De Spirito, “Nano-mechanical signature of brain tumours,” *Nanoscale*, vol. 8, pp. 19629–19643, 2016.

[124] C. Alibert, B. Goud, and J. B. Manneville, “Are cancer cells really softer than normal cells?,” *Biol. Cell*, vol. 109, pp. 167–189, 2017.

[125] E. W. Morawetz, R. Stange, T. R. Kießling, J. Schnauß, and J. A. Käs, “Optical stretching in continuous flows,” *Converg. Sci. Phys. Oncol.*, vol. 3, p. 024004, 2017.

[126] E. Kumacheva, R. K. Golding, M. Allard, and E. H. Sargent, “Colloid Crystal Growth on Mesoscopically Patterned Surfaces: Effect of Confinement,” *Adv. Matter*, vol. 14, p. 221, 2002.

[127] C.-A. Fustin, G. Glasser, H. W. Spiess, and U. Jonas, “Site-Selective Growth of Colloidal Crystals with Photonic Properties on Chemically Patterned Surfaces,” *Adv. Matter*, vol. 15, p. 1025, 2003.

[128] N. V. Dziomkina and G. J. Vancso, “Colloidal crystal assembly on topologically patterned templates,” *Soft Matter*, vol. 1, pp. 265–279, 2005.

[129] A. Cadilhe, N. A. M. Araújo, and V. Privman, “Random Sequential Adsorption: From Continuum to Lattice and Pre-Patterned Substrates,” *J. Phys. Condens. Matter*, vol. 19, p. 65124, 2007.

[130] M. Ebara, “Shape-memory surfaces for cell mechanobiology,” *Sci. Technol. Adv. Mater.*, vol. 16, p. 14804, 2015.

[131] B. L. Dossa, M. Pan, M. Gupta, G. Grenci, R.-M. Mège, C. T. Lim, M. P. Sheetz, R. Voituriez, and B. Ladoux, “Cell response to substrate rigidity is regulated by active and passive cytoskeletal stress,” *Proc. Natl. Acad. Sci. U. S. A.*, vol. 117, p. 12817, 2020.

[132] A. F. Mertz, S. Banerjee, Y. Che, G. K. German, Y. Xu, C. Hyland, M. C. Marchetti, V. Horsley, and E. R. Dufresne, “Scaling of traction forces with the size of cohesive cell colonies,” *Phys. Rev. Lett.*, vol. 108, pp. 1–5, 2012.

[133] C. A. Custódio and J. F. Mano, “Cell surface engineering to control cellular interactions,” *ChemNanoMat*, vol. 2, pp. 376–384, 2016.

[134] E. Marinari, A. Mehonic, S. Curran, J. Gale, T. Duke, and B. Baum, “Live-cell delamination counterbalances epithelial growth to limit tissue overcrowding,” *Nature*, vol. 484, pp. 542–545, 2012.

[135] V. Marx, “Tissue engineering: Organs from the lab,” *Nature*, vol. 522, pp. 373–377, 2015.

[136] E. Sackmann and A. S. Smith, “Physics of cell adhesion: Some lessons from cell-mimetic systems,” *Soft Matter*, vol. 10, pp. 1644–1659, 2014.

[137] E. Teomy, D. A. Kessler, and H. Levine, “Confluent and nonconfluent phases in a model of cell tissue,” *Phys. Rev. E*, vol. 98, p. 42418, 2018.

[138] P. Roca-Cusachs, V. Conte, and X. Trepat, “Quantifying forces in cell biology,” *Nat. Cell Biol.*, vol. 19, pp. 742–751, 2017.

[139] X. Serra-Picamal, V. Conte, R. Vincent, E. Anon, D. T. Tambe, E. Bazellieres, J. P. Butler, J. J. Fredberg, and X. Trepat, “Mechanical waves during tissue expansion,” *Nat. Phys.*, vol. 8, pp. 628–634, 2012.

[140] B. Ladoux and R. M. Mège, “Mechanobiology of collective cell behaviours,” *Nat. Rev. Mol. Cell Biol.*, vol. 18, pp. 743–757, 2017.

[141] S. A. Gudipaty, J. Lindblom, P. D. Loftus, M. J. Redd, K. Edes, C. F. Davey, V. Krishnegowda, and J. Rosenblatt, “Mechanical stretch triggers rapid epithelial cell division through Piezo1,” *Nature*, vol. 543, pp. 118–121, 2017.

[142] A. Mkrtchyan, J. Åström, and M. Karttunen, “A new model for cell division and migration with spontaneous topology changes,” *Soft Matter*, vol. 10, pp. 4332–4339, 2014.

[143] T. B. Saw, A. Doostmohammadi, V. Nier, L. Kocgozlu, S. Thampi, Y. Toyama, P. Marcq, C. T. Lim, J. M. Yeomans, and B. Ladoux, “Topological defects in epithelia govern cell death and extrusion,” *Nature*, vol. 544, pp. 212–216, 2017.

[144] G. Thrivikraman, A. Jagiełło, V. K. Lai, S. L. Johnson, M. Keating, A. Nelson, B. Schultz, C. M. Wang, A. J. Levine, E. L. Botvinick, and R. T. Tranquillo, “Cell contact guidance via sensing anisotropy of network mechanical resistance,” *Proc. Natl. Acad. Sci. U. S. A.*, vol. 118, p. e2024942118, 2021.

[145] L. Balasubramaniam, A. Doostmohammadi, T. B. Saw, G. H. N. S. Narayana, R. Mueller, T. Dang, M. Thomas, S. Gupta, S. Sonam, A. S. Yap, Y. Toyama, R. M. Mège, J. M. Yeomans, and B. Ladoux, “Investigating the nature of active forces in tissues reveals how contractile cells can form extensile monolayers,” *Nat. Mater.*, vol. 20, pp. 1156–1166, 2021.

[146] B. Aigouy, R. Farhadifar, D. B. Staple, A. Sagner, J. C. Röper, F. Jülicher, and S. Eaton, “Cell Flow Reorients the Axis of Planar Polarity in the Wing Epithelium of Drosophila,” *Cell*, vol. 142, pp. 773–786, 2010.

[147] T. Büscher, A. L. Diez, G. Gompper, and J. Elgeti, “Instability and fingering of interfaces in growing tissue,” *New J. Phys.*, vol. 22, p. 083005, 2020.

[148] A. J. Kabla, “Collective cell migration: Leadership, invasion and segregation,” *J. R. Soc. Interface*, vol. 9, pp. 3268–3278, 2012.

[149] A. Saraswathibhatla and J. Notbohm, “Tractions and Stress Fibers Control Cell Shape and Rearrangements in Collective Cell Migration,” *Phys. Rev. X*, vol. 10, p. 11016, 2020.

[150] D. Weaire and S. Hutzler, *The physics of foams.* Clarendon Press, 1999.

[151] S. Koride, A. J. Loza, and S. X. Sun, "Epithelial vertex models with active biochemical regulation of contractility can explain organized collective cell motility," *APL Bioeng.*, vol. 2, p. 031906, 2018.

[152] X. Yang, D. Bi, M. Czajkowski, M. Merkel, M. L. Manning, and M. C. Marchetti, "Correlating cell shape and cellular stress in motile confluent tissues," *Proc. Natl. Acad. Sci. U. S. A.*, vol. 114, pp. 12663–12668, 2017.

[153] S. Okuda and K. Fujimoto, "A Mechanical Instability in Planar Epithelial Monolayers Leads to Cell Extrusion," *Biophys. J.*, vol. 118, p. 2549, 2020.

[154] D. M. Sussman and M. Merkel, "No unjamming transition in a Voronoi model of biological tissue," *Soft Matter*, vol. 14, pp. 3397–3403, 2018.

[155] C. P. Goodrich, A. J. Liu, and S. R. Nagel, "Finite-size scaling at the jamming transition," *Phys. Rev. Lett.*, vol. 109, pp. 1–5, 2012.

[156] L. Coburn, H. Lopez, B. J. Caldwell, E. Moussa, C. Yap, R. Priya, A. Noppe, A. P. Roberts, V. Lobaskin, A. S. Yap, Z. Neufeld, and G. A. Gomez, "Contact inhibition of locomotion and mechanical cross-Talk between cell-cell and cell-substrate adhesion determine the pattern of junctional tension in epithelial cell aggregates," *Mol. Biol. Cell*, vol. 27, pp. 3436–3448, 2016.

[157] S. S. Soumya, A. Gupta, A. Cugno, L. Deseri, K. Dayal, D. Das, S. Sen, and M. M. Inamdar, "Coherent Motion of Monolayer Sheets under Confinement and Its Pathological Implications," *PLoS Comput. Biol.*, vol. 11, pp. 1–30, 2015.

[158] F. Pérez-Verdugo, J.-F. Joanny, and R. Soto, "Vertex model instabilities for tissues subject to cellular activity or applied stresses," *Phys. Rev. E*, vol. 102, p. 052604, 2020.

[159] L. Yan and D. Bi, "Multicellular Rosettes Drive Fluid-solid Transition in Epithelial Tissues," *Phys. Rev. X*, vol. 9, p. 11029, 2019.

[160] S. Kim, M. Pochitaloff, G. A. Stooke-Vaughan, and O. Campàs, "Embryonic tissues as active foams," *Nat. Phys. 2021 177*, vol. 17, pp. 859–866, 2021.

[161] R. Chen and C. Gotsman, "Localizing the Delaunay Triangulation and its Parallel Implementation," in *2012 Ninth Int. Symp. Vor. Diagrams Sci. Eng.*, pp. 24–31, 2012.

[162] D. M. Sussman, J. M. Schwarz, M. C. Marchetti, and M. L. Manning, "Soft yet Sharp Interfaces in a Vertex Model of Confluent Tissue," *Phys. Rev. Lett.*, vol. 120, p. 58001, 2018.

[163] S. Franz, A. Sclocchi, and P. Urbani, "Critical Jammed Phase of the Linear Perceptron," *Phys. Rev. Lett.*, vol. 123, p. 115702, 2019.

[164] A. Seguin and O. Dauchot, "Experimental Evidence of the Gardner Phase in a Granular Glass," *Phys. Rev. Lett.*, vol. 117, p. 228001, 2016.

[165] C. Scalliet, L. Berthier, and F. Zamponi, "Absence of Marginal Stability in a Structural Glass," *Phys. Rev. Lett.*, vol. 119, p. 205501, 2017.

[166] E. Bitzek, P. Koskinen, F. Gähler, M. Moseler, and P. Gumbsch, “Structural relaxation made simple,” *Phys. Rev. Lett.*, vol. 97, pp. 1–4, 2006.

[167] F. Murtagh, “A survey of recent advances in hierarchical clustering algorithms,” *Comput. J.*, vol. 26, pp. 354–359, 1983.

[168] R. Langer and J. P. Vacanti, “Tissue engineering,” *Science*, vol. 260, pp. 920–926, 1993.

[169] C. F. Guimarães, L. Gasperini, A. P. Marques, and R. L. Reis, “The stiffness of living tissues and its implications for tissue engineering,” *Nat. Rev. Mater.*, vol. 5, p. 351, 2020.

[170] T. Iskratsch, H. Wolfenson, and M. P. Sheetz, “Appreciating force and shape — the rise of mechanotransduction in cell biology,” *Nat. Rev. Mol. Cell Biol.*, vol. 15, p. 825, 2014.

[171] E. Garreta, P. Prado, C. Tarantino, R. Oria, L. Fanlo, E. Martí, D. Zalvidea, X. Trepat, P. Roca-Cusachs, A. Gavaldà-Navarro, L. Cozzuto, J. M. Campistol, J. C. Izpisúa Belmonte, C. del Pozo, and N. Montserrat, “Fine tuning the extracellular environment accelerates the derivation of kidney organoids from human pluripotent stem cells,” *Nat. Mater.*, vol. 18, p. 397, 2019.

[172] S. H. Kim, J. Turnbull, and S. Guimond, “Extracellular matrix and cell signalling: The dynamic cooperation of integrin, proteoglycan and growth factor receptor,” *J. Endocrinol.*, vol. 209, pp. 139–151, 2011.

[173] C. J. Miller and L. A. Davidson, “The interplay between cell signalling and mechanics in developmental processes,” *Nat. Rev. Genet.*, vol. 14, p. 733, 2013.

[174] W. J. Hadden, J. L. Young, A. W. Holle, M. L. McFetridge, D. Y. Kim, P. Wijesinghe, H. Taylor-Weiner, J. H. Wen, A. R. Lee, K. Bieback, B.-N. Vo, D. D. Sampson, B. F. Kennedy, J. P. Spatz, A. J. Engler, and Y. S. Choi, “Stem cell migration and mechanotransduction on linear stiffness gradient hydrogels,” *Proc. Natl. Acad. Sci. U. S. A.*, vol. 114, pp. 5647–5652, 2017.

[175] C. M. Kraning-Rush, J. P. Califano, and C. A. Reinhart-King, “Cellular traction stresses increase with increasing metastatic potential,” *PLoS One*, vol. 7, p. e32572, 2012.

[176] K. R. Levental, H. Yu, L. Kass, J. N. Lakins, M. Egeblad, J. T. Erler, S. F. Fong, K. Csiszar, A. Giaccia, W. Weninger, M. Yamauchi, D. L. Gasser, and V. M. Weaver, “Matrix Crosslinking Forces Tumor Progression by Enhancing Integrin Signaling,” *Cell*, vol. 139, pp. 891–906, 2009.

[177] P. Carmeliet and R. K. Jain, “Angiogenesis in cancer and other diseases,” *Nature*, vol. 407, pp. 249–257, 2000.

[178] M. Egeblad and Z. Werb, “New functions for the matrix metalloproteinases in cancer progression,” *Nat. Rev. Cancer*, vol. 2, pp. 161–174, 2002.

[179] K. Wolf and P. Friedl, “Mapping proteolytic cancer cell-extracellular matrix interfaces,” *Clin. Exp. Metastasis*, vol. 26, pp. 289–298, 2009.

[180] C. M. Kraning-Rush, S. P. Carey, M. C. Lampi, and C. A. Reinhart-King, “Microfabricated collagen tracks facilitate single cell metastatic invasion in 3D,” *Integr. Biol.*, vol. 5, pp. 606–616, 2013.

[181] A. Hernandez, M. F. Staddon, M. J. Bowick, M. C. Marchetti, and M. Moshe, “Geometric rigidity and anomalous elasticity of cellular tissue vertex model,” 2021.

[182] J. Huang, J. O. Cochran, S. M. Fielding, M. C. Marchetti, and D. Bi, “Shear-driven solidification and nonlinear elasticity in epithelial tissues,” 2021.

[183] D. E. P. Pinto, G. Erdemci-Tandogan, M. L. Manning, and N. A. M. Araújo, “The Cell Adaptation Time Sets a Minimum Length Scale for Patterned Substrates,” *Biophys. J.*, vol. 119, pp. 2299–2306, 2020.

[184] D. Stauffer and A. Aharony, *Introduction To Percolation Theory*. Taylor & Francis, 2018.

[185] M. Sahini and M. Sahimi, *Applications Of Percolation Theory*. CRC Press, 1994.

[186] P. Sahu, D. M. Sussman, M. Rübsam, A. F. Mertz, V. Horsley, E. R. Dufresne, C. M. Niessen, M. C. Marchetti, M. L. Manning, and J. M. Schwarz, “Small-scale demixing in confluent biological tissues,” *Soft Matter*, vol. 16, pp. 3325–3337, 2020.

[187] L. G. Griffith and G. Naughton, “Tissue Engineering—Current Challenges and Expanding Opportunities,” *Science*, vol. 295, p. 1009, 2002.

[188] A. Rabodzey, P. Alcaide, F. W. Luscinskas, and B. Ladoux, “Mechanical Forces Induced by the Transendothelial Migration of Human Neutrophils,” *Biophys. J.*, vol. 95, p. 1428, 2008.

[189] M. S. Steinberg, “Reconstruction of Tissues by Dissociated Cells,” *Science*, vol. 141, p. 401, 1963.

[190] A. K. Harris, “Is cell sorting caused by differences in the work of intercellular adhesion? A critique of the steinberg hypothesis,” *J. Theor. Biol*, vol. 61, p. 267, 1976.

[191] G. W. Brodland, “The Differential Interfacial Tension Hypothesis (DITH): A Comprehensive Theory for the Self-Rearrangement of Embryonic Cells and Tissues,” *J. Biomech. Eng.*, vol. 124, p. 188, 2002.

[192] R. A. Foty and M. S. Steinberg, “The differential adhesion hypothesis: a direct evaluation,” *Dev. Biol.*, vol. 278, p. 255, 2005.

[193] J. D. Amack and M. L. Manning, “Knowing the Boundaries: Extending the Differential Adhesion Hypothesis in Embryonic Cell Sorting,” *Science*, vol. 338, p. 212, 2012.

[194] J.-L. Maître, H. Berthoumieux, S. F. G. Krens, G. Salbreux, F. Jülicher, E. Paluch, and C.-P. C.-P. Heisenberg, “Adhesion Functions in Cell Sorting by Mechanically Coupling the Cortices of Adhering Cells,” *Science*, vol. 338, p. 253, 2012.

[195] M. Krieg, Y. Arboleda-Estudillo, P.-H. Puech, J. Käfer, F. Graner, D. J. Müller, and C.-P. Heisenberg, “Tensile forces govern germ-layer organization in zebrafish,” *Nat. Cell Biol.*, vol. 10, p. 429, 2008.

[196] M. R. Carvalho, F. R. Maia, J. Silva-Correia, B. M. Costa, R. L. Reis, and J. M. Oliveira, “A semiautomated microfluidic platform for real-time investigation of nanoparticles’ cellular uptake and cancer cells’ tracking,” *Nanomedicine*, vol. 12, p. 581, 2017.

[197] T. Ekblad and B. Liedberg, “Protein adsorption and surface patterning,” *Curr. Opin. Colloid Interface Sci.*, vol. 15, pp. 499–509, 2010.

[198] L. Cademartiri and K. J. Bishop, “Programmable self-assembly,” *Nat. Mater.*, vol. 14, pp. 2–9, 2015.

[199] P. A. DiMilla, K. Barbee, and D. A. Lauffenburger, “Mathematical model for the effects of adhesion and mechanics on cell migration speed,” *Biophys. J.*, vol. 60, pp. 15–37, 1991.

[200] S. Kaliman, M. Hubert, C. Wollnik, L. Nuić, D. Vurnek, S. Gehrer, J. Lovrić, D. Dudziak, F. Rehfeldt, and A. S. Smith, “Mechanical Regulation of Epithelial Tissue Homeostasis,” *Phys. Rev. X*, vol. 11, p. 031029, 2021.

Appendix A

Derivation of the continuum equations

A.1 Time dependent solution for the continuum model in chapter 5

To solve Eq. (5.6), we define a characteristic length $L^* = L/2$ and time $T^* = L^2/4D^*$, respectively, and introduce two adimensional variables,

$$\hat{x} = \frac{2x}{L} \qquad \hat{t} = \frac{4D^* t}{L^2}. \tag{A.1}$$

Using the chain rule, we get the following identities,

$$u_t = \frac{1}{T^*} u_{\hat{t}} \text{ and } u_{xx} = \frac{1}{(L^*)^2} u_{\hat{x}\hat{x}}. \tag{A.2}$$

By replacing them in Eq. (5.6), we obtain,

$$u_{\hat{t}}(\hat{x}, \hat{t}) = u_{\hat{x}\hat{x}}(\hat{x}, \hat{t}) + \phi^2[1 - u(\hat{x}, \hat{t})] \tag{A.3}$$

where $\phi^2 = TL^2/4D^*$. The initial and boundary conditions are then,

$$u(0, \hat{t}) = u(1, \hat{t}) = 0, \qquad \hat{t} > 0, \tag{A.4}$$

$$u(\hat{x}, 0) = 1, \qquad 0 < \hat{x} < 1. \tag{A.5}$$

In chapter 5, we present the stationary state solution $u_E(\hat{x})$ obtained by setting $u_{\hat{t}} = 0$. Here, to derive the time dependent solution, we define,

$$v(\hat{x}, \hat{t}) = u(\hat{x}, \hat{t}) - u_E(\hat{x}). \tag{A.6}$$

Substituting in Eq. A.3 gives,

$$v_t(\hat{x}, \hat{t}) = v_{xx}(\hat{x}, \hat{t}) - \phi^2 v(\hat{x}, \hat{t}) \ , \tag{A.7}$$

and the boundary conditions are now,

$$v(0, \hat{t}) = v(1, \hat{t}) = 0, \qquad \hat{t} > 0, \tag{A.8}$$

$$v(\hat{x}, 0) = 1 - u_E(\hat{x}), \qquad 0 < \hat{x} < 1. \tag{A.9}$$

This set of equations is solved by separation of variables, $v(\hat{x}, \hat{t}) = X(\hat{x})T(\hat{t})$, which gives,

$$\frac{T'(\hat{t})}{T(\hat{t})} + \phi^2 = \frac{X''(\hat{x})}{X(\hat{x})}. \tag{A.10}$$

Imposing the initial and boundary conditions, we obtain,

$$u(\hat{x},\hat{t}) = \frac{4}{\pi}\sum_{n=1}^{\infty}\left\{\left[1-\frac{\phi^2}{(2n-1)^2\pi^2+\phi^2}\right]\frac{\sin[(2n-1)\pi\hat{x}]}{(2n-1)}e^{-[(2n-1)^2\pi^2+\phi^2]\hat{t}}\right\}+\frac{1+e^{\phi}-e^{-\phi(-1+\hat{x})}-e^{\phi\hat{x}}}{1+e^{\phi}}\ , \tag{A.11}$$

which, in the limit $\hat{t}\to\infty$ gives the stationary solution.